Effect of an diffuser on the performance of an ocean current turbine

by
Josh Reinecke

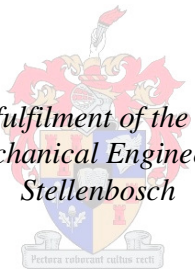

Thesis presented in partial fulfilment of the requirements for the degree Master of Science in Mechanical Engineering at the University of Stellenbosch

Supervisor: prof. T W von Backstöm
Co-supervisor: prof. G Venter
Engineering Faculty
Department of Mechanical and Mechatronic Engineering

March 2011

Effect of a diffuser on the power production of an ocean current turbine

by

Josh Reinecke

Thesis presented in partial fulfilment of the requirements for the degree of Master of Science in Engineering (Mechanical) at Stellenbosch University

Department of Mechanical and Mechatronic Engineering
University of Stellenbosch
Private Bag X1, 7602 Matieland, South Africa

Supervisor: T.W von Backström and G Venter

March 2011

Declaration

By submitting this thesis electronically, I declare that the entirety of the work contained therein is my own, original work, that I am the owner of the copyright thereof (unless to the extent explicitly otherwise stated) and that I have not previously in its entirety or in part submitted it for obtaining any qualification.

Date: .....

Abstract

Effect of a diffuser on the power production of an ocean current turbine

J Reinecke

Department of Mechanical and Mechatronic Engineering
University of Stellenbosch
Private Bag X1, 7602 Matieland, South Africa

Thesis: MSc.Eng (Mechanical)

March 2011

Ocean current turbines are hydropower turbines that extract kinetic energy from ocean currents. The marine current resource has a major advantage over other renewable energy resources in that it is essentially non-intermittent and predictable over long time periods. The purpose of the study is to investigate the increase in power density of an existing model ocean current turbine, due to a geometrically optimised curved plate diffuser. A single curved plate diffuser with an area ratio of 3.29 was designed. The diffuser shape was characterised as a B-spline defined by four variables. A two-dimensional computational fluid dynamics (CFD) analysis was used as function evaluation for a Latin hyper cube design of experiments (DOE). A support vector regression metamodel was constructed from the DOE and optimised. The metamodel predicted a maximum C_p of 1.672. The diffuser was manufactured and tests conducted in a towing tank facility at a flow speed of 1.5 m/s. Results showed an increase in turbine peak power from 383 W (Cp = 0.43) for the bare turbine to a measured 1512 W (C_p = 1.74) for the turbine with the optimised diffuser. This represented an increase in power production by a factor of 4.05.

Uittreksel

Die effek van 'n diffisor op die werkverigting van 'n seestroomturbine

J Reinecke

Departement Meganiese en Megatroniese Ingenieurswese
Universiteit van Stellenbosch
Privaatsak X1, 7602 Matieland, Suid Afrika

Tesis: MSc.Ing (Meganies)

Maart 2011

Seestroomturbines is hidro-turbines wat kinetiese energie uit seestrome onttrek. Die seestroom energie hulpbron het 'n groot voordeel bo ander hernubare energiebronne daarin dat dit inherent ononderbroke is oor lang tydperke. Die doel van die studie is om die toename in drywings digtheid van 'n bestaande SST te bestudeer deur die gebruik van 'n geometries geoptimeerde geboë plaat diffisor. Slegs een geboë plaat diffisor met 'n area verhouding van 3.29 is ontwerp. Die diffisorvorm is met behulp van vier verstelbare veranderlikes as 'n B-tipe latfunksie gedefinieer. 'n Twee-dimensionele numeriese vloei dinamika (NFD) model is geskep as funksie evaluasie vir 'n 'Latin hyper cube' ontwerp van eksperimente (OVE). Die 'Support vector regression' (SVR) metamodel was gebou van die OVE en geoptimeer. Die metamodel het 'n maksimum C_p van 1.672 voorspel. Die diffisor is toe vervaardig en toetse in 'n sleeptenkfasiliteit gedoen by 'n vloeispoed van 1.5 m/s. Resultate toon 'n toename in maksimum turbine werksverrigting van 383 W (C_p = 0.43) vir die normale turbine, na 'n gemete 1512 W (C_p = 1.74) vir die turbine met die geoptimeerde diffisor. Dit verteenwoordig 'n drywingsfaktor verbetering van 4.05 in turbine werksverrigting.

Acknowledgements

To Prof. von Backström and Venter for guidance and the incredible opportunity to work and learn under them.

My family for their support and encouragement in times of near death and abundant life.

Friends, all of them.

> "I have been with God and with the devil. I fought between the two... I seized the hand of God, it was the best hand... I always knew God would get us out of there." Second rescued Chilean miner Mario Sepulveda - *Cpiapo, Camp Hope, 2010*

Dedications

vir Pa

Contents

List of Figures

List of Tables

List of Abbreviations

AAE	Absolute Average Error
CAD	Computer-Aided Design
CFD	Computational Fluid Dynamics
CNC	Computer Numerical Control
DOE	Design of Experiments
FEM	Finite Element Analysis
LHC	Latin Hyper Cube
MCT	Marine Current Turbine
OCT	Ocean Current Turbine
RKT	River Kinetic Turbine
RMS	Root Mean Scquare
SD	Standard Deviation
SVR	Support Vector Regression
TSR	Tip Speed Ratio
US	University of Stellenbosch
VSD	Variable Speed Drive
1D	One-Dimensional
2D	Two-Dimensional
3D	Three-Dimensional

List of Symbols

Symbols

A = rotor area

a = induction factor

C = regularisation parameter

C_d = drag coefficient

C_p = power coefficient

C_{pe} = diffuser exit pressure

C_t = thrust coefficient

dA = discrete area

K = kernel function

$\dot{m}$ = mass flow

P = shaft power

P_{min} = minimum number of design points required

p_0 = static pressure at inlet plane

p = static pressure just in front rotor plane

r = efficiency factor

T = thrust

u = axial velocity at rotor plane

u_1 = axial velocity at exit plane

V = velocity

Vol = fluid volume

V_0 = axial velocity at inlet plane

$y^\star$ = dimensionless wall unit

$\hat{y}$ = approximation

η = diffuser efficiency

ρ = density

σ = radius parameter

Δ = change in variable

Subscripts

$avail$ = available

min = minimum

$side$ = from side of control volume

cv = control volume

d = diffuser

b = bare turbine

1 = at exit plane

0 = at inlet plane (free stream)

Chapter 1

Introduction

1.1 Background Information

The evidence of climate change and global warming has spurred human civilisation to ponder the possible consequences of the exploitation of Earth's resources. International consciousness has now moved towards conserving the environment. This is most evident by regulations within the power-generating industry, which is dominated by fossil-fuel electricity generation. The European Union recently committed itself to have 20 % of its energy needs met by renewable energy sources by the year 2020 [1]. In South Africa, the 2003 White Paper on Renewable Energy stipulated that 5 % of electricity generated should originate from renewable energy sources by the year 2013. In the recently released IRP 2010, this figure has shifted to 16 % of the installed capacity [2, 3].

Energy from the ocean is obtained in a number of ways, including off-shore wind; tidal stream, wave-energy, tidal barrages, ocean thermal energy conversion and osmotic pressure exploitation. The most advanced of these technologies are off-shore wind, wave, and tidal stream/ocean current technology. This research focuses on ocean current energy.

There are two methods of taking advantage of tidal power. Tidal stream systems make use of the kinetic energy of a moving tidal stream to power turbines. The theory applied is very similar to wind turbines, except that the fluid medium is water instead of air. The second type of system is the barrage system which converts potential energy from the difference in height between low tide and high tide. Barrage systems collect high-tide water in a "dam" and slowly release this water during low tide. The physical construction of the barrage system tends to make the concept more expensive than a tidal stream system and is also more damaging to the ecology of the seabed [4]. An image of a tidal stream turbine is shown in figure 1.1.

An ideal location for a tidal stream or ocean current turbine is where large ocean currents

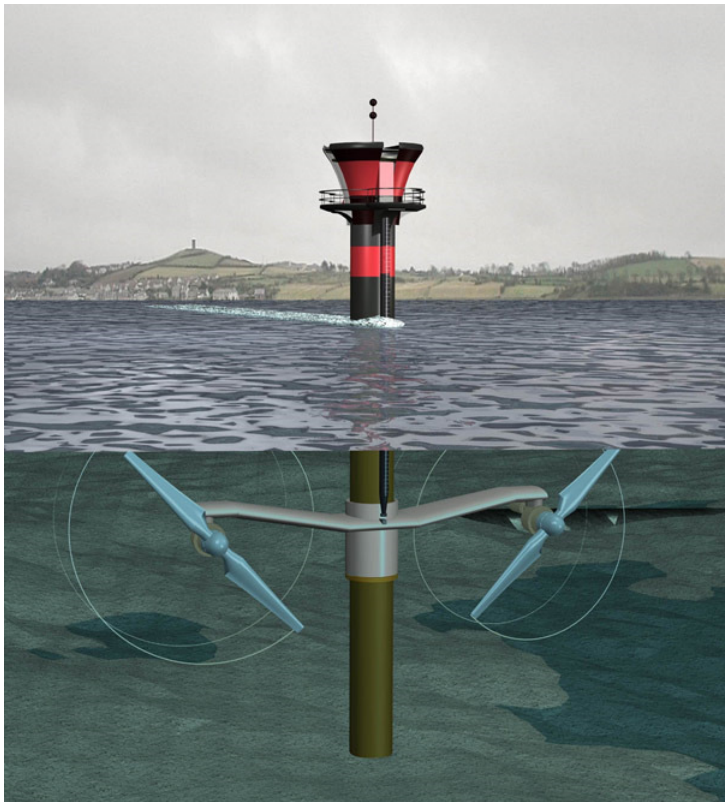

Figure 1.1: Seagen tidal stream turbine.

are channelled through constraining topography, thus producing high current velocities. This would naturally occur in an underwater gully, valley or channel. Feasibility studies have indicated that large marine current resources are to be found in regions such as South East Asia (Japan, Indonesia, Philippines), Australia, New Zealand, and the South-East coast of South Africa (the Mozambique and Agulhas current) [5]. The development of Ocean Current Turbines (OCTs) within South Africa has favourable prospects and Eskom has launched a resource assessment of the Agulhas current for this purpose [6].

The exploitation of ocean current energy in the form of a turbine is very similar to the application of wind turbines in air. Ocean current energy is however considered a "fledgling" form of renewable energy compared to wind energy [7]. Although the theory and basic system components are quite similar, wind energy technology is more developed. Design for the operating conditions that occur in a submerged system presents a number of practical challenges. Maintenance and accessibility are difficult, thus requiring that OCT systems be robust, reliable and designed for long life. The strength of the support structure and turbine is therefore an important design requirement. A further difficulty for OCT systems is the provision of a grid-connection point and the risk of cavitation damage to a turbine rotor.

The exploitation of ocean currents offers many benefits and good prospects for kinetic

energy extraction. Given a suitable site of concentrated flow and high velocities, OCTs can offer up to four times the energy intensity of a good wind site and 30 times the energy intensity of a solar plant in the Sahara Desert [8]. The diameter requirement for an ocean current rotor is half that of a wind turbine with the same power rating [7]. By adding a diffuser to a turbine, this power rating can be dramatically increased for the OCT [9]. Using smaller OCTs furthermore leads to decreased manufacturing costs, with less material being required. Smaller size also increases the turbine farm potential, since OCT turbines can be packed much closer together than in the case of a wind farm [8]. Another advantage of OCTs is that weight is not a critical factor, with a submerged system utilising buoyancy. Provided that some form of corrosion protection exists, support structures may therefore be manufactured out of steel which lowers the cost of manufacture [8]. Finally, and possibly the most favourable motivation for using OCTs, is the fact that an OCT system can produce energy consistently and predictably. Ocean currents are regular – their strength and directional frequency can be predicted. This allows for a degree of reliability that is not often encountered within renewable energy [10]. It is believed that with sufficient research and development, the technology will become more cost-effective and the practical challenges will be overcome.

Previous Studies

Recent studies have investigated the concept of shrouded or diffuser-augmented turbines [11, 12, 13] to increase the power production of an OCT or similar turbine. Diffuser augmentation refers to the utilisation of a diffuser around a turbine rotor to increase the turbine power production. By applying a diffuser to a bare rotor, it aims to increase the kinetic energy density at the rotor plane and thus increase the power extraction of the turbine over its bare rotor counter part. This has proven economically beneficial to producers. Consider the simple case of installing an OCT. In simplified terms, it involves the installation of a rotor, generator and gearbox. If, for instance, the addition of the diffuser would increase the power production of a single bare rotor turbine by a factor of two, one will be producing twice the power but at the cost of only a single generator, gearbox, rotor and diffuser.

Most topical research involves the use of straight wall diffusers with no curvature or variable gradients. A recent study conducted by Grobbelaar [11] involving a straight wall diffuser indicates a power increase over the bare turbine by a factor of 1.85. The diffuser used in his study had an outer diameter of 1.452 m and a rotor diameter of 0.8 m. Figure 1.2 illustrates this diffuser-augmented turbine system.

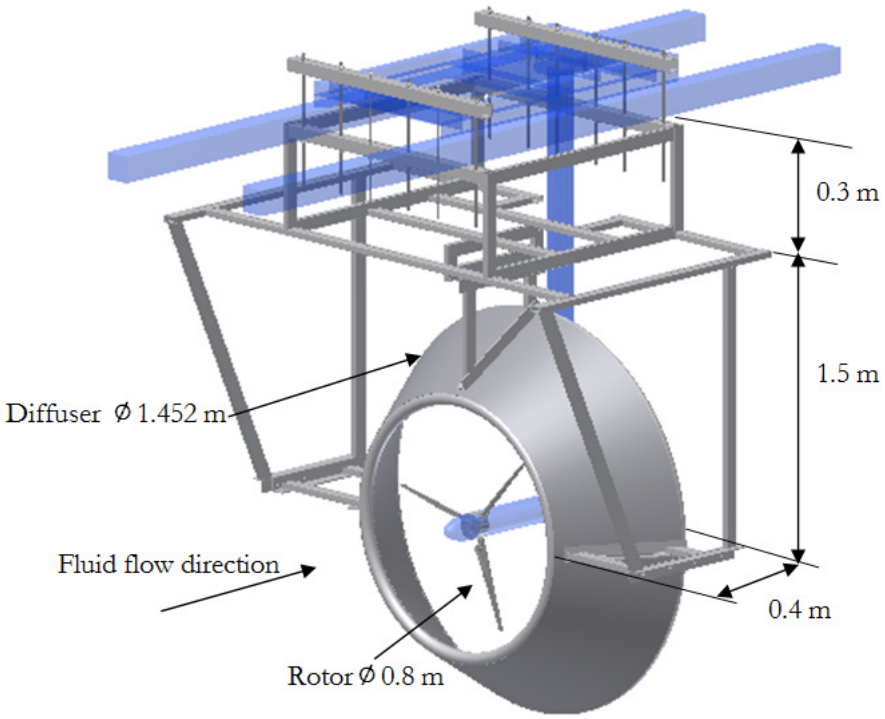

Figure 1.2: Diffuser turbine system of Grobbelaar [11].

1.2 Problem Statement

Very little experimental data currently exists with regard to diffuser augmentation studies, and the upper limit as to how much augmentation can be achieved is yet unknown [14]. In addition, only very simplistic diffuser designs have been investigated [12, 15]. A considerable improvement in diffuser-augmented power production is therefore considered to be possible through optimising the diffuser shape parameters. Although various numerical studies have been done into diffuser augmentation, very few experimental comparisons of such results exist.

The researcher aims to conduct a more in-depth optimisation of the diffuser shape, and provide numerical results based on CFD, and to conduct experimental investigations that are comparable to the CFD data.

1.3 Research Objectives

The broad objective of this project is to investigate the layout and design of a turbine concept utilising a diffuser for application within an OCT power generation system. To quantify the effect of the diffuser on the power production of the turbine, the following was decided:

- To use a similarly-sized diffuser as in Grobbelaar [11] with an existing rotor design, but to improve its augmentation factor of 1.85 to at least a factor of two.
- To utilise a more complex-shaped diffuser to gain insight into shape dynamics that affect diffuser performance.
- To compare the simulated performance results with practical results obtained from an experimental model.

All of the above will contribute to the knowledge base of diffuser augmentation, particularly with regards to the effect of complex diffuser shapes on turbine performance. Practical results to support CFD findings and thus validate a certain numerical simulation method, will furthermore also be generated. This will enable improved design considerations for full-scale prototypes in the future.

Thesis Statement

The thesis statement can be stated as follows:

> To increase the kinetic energy density of fluid passing through an existing rotor design by using an optimised diffuser design.

To explain this briefly, the research will apply an optimisation technique to design an optimal diffuser with a maximum outer diameter of 1.452 m. With this optimal diffuser, the researcher will aim to improve the power production of the current rotor design used by Reinecke [16]. By following this method, additional insight into the use of a single diffuser-augmented turbine over multiple turbine rotors will be gained by comparing the experimental results.

1.4 Limitations

The following limitations to the study have been identified:

- Using the same diffuser geometrical envelope and rotor designs as was used in Grobbelaar [11];
- Only design tools (CFD, CAD and optimisation techniques) are to be employed that are available for use at the University of Stellenbosch (US);

- Experimental testing will only be conducted at US towing tank facility and no other facilities will be considered;
- Only a single optimum diffuser shape will be manufactured and tested due to time constraints;
- Manufacturing is to be done within the constraints of the allowed budget only;
- Findings will only relate to the performance of the specific rotors tested and;
- Due to time constraints, no cost model to evaluate the economic feasibility of the diffuser will be presented.

1.5 Definition of Terms and Concepts

Key concepts related to the review include various terms used, and the most relevant of these will briefly be explained.

The term "OCT" or "ocean current turbine" is used as opposed to marine current turbine (MCT) or river kinetic turbine (RKT). Although a MCT and RKT share the same basic method of operation with an OCT, unless stated otherwise OCT will be used as a general term.

The use of the term "diffuser" refers to a device that is placed around a turbine rotor in order to increases the power production of a turbine by causing a greater pressure drop behind the rotor. Geometrically the diameter increases along the streamwise direction from the rotor plane to the diffuser exit plane.

"Shrouding" refers to a device placed around a turbine that has a constant diameter in the streamwise direction.

The "bare rotor" refers to a turbine not utilising a diffuser or shroud. "Power augmentation" refers to the factor increase in power production of a diffuser-augmented turbine over a bare turbine.

The term "diffuser area ratio" refers to the area ratio calculated using the largest outer diameter of a specific diffuser over the bare turbine rotor swept area.

1.6 Significance of the Study

The research findings and results are intended to contribute knowledge to the theoretical explanation of the diffuser effect and how it can be formulated for one-dimensional (1D)

turbine theory. It will furthermore shed light on how power augmentation prediction formulas are used and how they performed against the research findings.

The researcher intends to propose a more complex optimisation procedure that can be successfully used to design an optimal diffuser that leads to greater gains in power augmentation of OCTs. It has furthermore been ascertained from literature on the topic that diffusers have been designed for low to medium efficiency rotors [17, 9, 12], but none for high-efficiency rotors. The researcher aims to provide insight into the effect of a diffuser on high-efficiency rotors.

To the researcher's knowledge, no design involving a curved plate diffuser or annular airfoil diffuser has been designed for OCT diffuser augmentation. No experimental results exist in the available literature and thus the research will add valuable data to the research community.

An experimentally validated maximum power augmentation factor greater than two for OCTs is not found in literature. Consequently this investigation's purpose is to increase the maximum augmentation factor above 2 and present a new achievable maximum for a given rotor design.

1.7 Brief Chapter Overviews

The dissertation will start with a literature review that contains the theory base used to evaluate the effect of diffuser augmentation followed by the state of OCTs and a discussion on similar studies previously conducted. Deriving from an awareness of the shortcomings of previous studies, the design for the current research and methodology will be presented.

The main section of the dissertation conveys details of the chosen research design together with each section's results and short sub-conclusions. Parts of the main section include a numerical investigation that uses a chosen optimisation technique and provides the optimal diffuser shape, the design of the diffuser and test rig, the manufacturing of the necessary elements and the actual testing of the diffuser-augmented turbine. A discussion of the results then follows and the optimal diffuser is compared to results from previous studies. Lastly a conclusion is presented that summarises the main findings and their significance.

Chapter 2

Literature Review

2.1 Introduction

In the previous chapter a brief overview of what OCTs are and their reason for existence are presented. In this chapter a broader and more in-depth literature review is presented pertaining to various aspects of the technology and underlying theories. This review therefore has two main objectives. The first is to present the applicable theory base to understand power extraction of OCTs, and the second to review recent developments in OCT technology and trends, with a concluding part on similar diffuser studies.

The existence of OCTs and their development from wind turbine technology will then be investigated in more detail, specifically focusing on design and analysis tools used to evaluate wind turbines, such as CFD analysis, etc. Various pitfalls can be avoided in the design process if the correct design tools are identified to increase turbine performance. Finally, the studies most closely related to OCT shrouding will be discussed to indicate possible shortcomings in existing designs.

2.2 Theory Base: The Betz Limit

Betz's limit, or Betz's law, is the generally accepted theory that establishes the maximum possible amount of power that can be extracted by a wind turbine (or any unshrouded horizontal axis turbine in free fluid flow) to be 59.3 % of the available kinetic energy passing through a free stream area equal to the rotor swept area [18, 19]. Recent studies and proposed theories have been proposed to extend this law to shrouded turbines [14, 20, 21].

This limit in power extraction was derived in 1920 by Albert Betz [19], but according to Van Kuik [22]; Lanchester [23, 24], and Joukowsky [25] arrived at the same theoretical

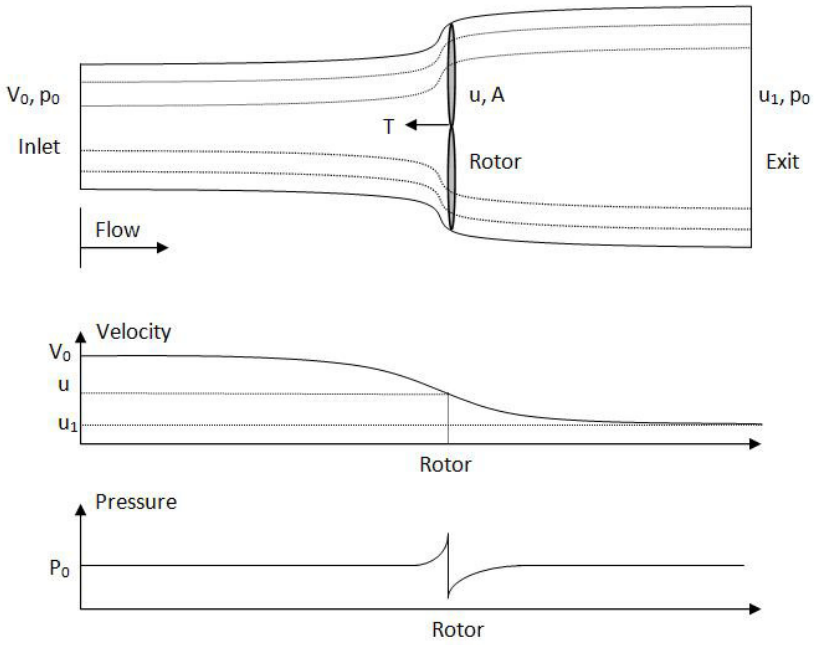

Figure 2.1: Turbine control volume showing streamlines.

maximum related to kinetic energy extraction from free fluid flow. Hence a more acceptable phrasing of the extraction limit is proposed to be the Lanchester-Betz-Joukowsky limit. In this study, however, Betz's law will be used as an abbreviation of the Lanchester-Betz-Joukowsky law.

Since the primary goal of this research is to maximise the kinetic energy extraction of a model OCT, Betz's law describing the kinetic energy extraction by a turbine rotor forms the core theory of the project. All of the performance design and optimisation in the rest of the project is to be based on this theory directly or indirectly. A derivation similar to that presented in Hansen [18] will be followed here.

The theory has some basic assumptions and is formulated based on a one-dimensional (1D) model using an actuator disc as formulated in [26]. The disc represents an ideal rotor, meaning it does not possess a hub, and is infinitely thin and frictionless. No angular momentum is transferred to or from the disk (zero rotational velocities). It assumes stationary incompressible flow with constant density throughout the volume, and no heat transfer occurs from or to the rotor. An illustration of the streamlines through the rotor is shown in figure 2.1 along with the change in velocity and pressure.

As kinetic energy is extracted at the disc, the flow speed slows from V_0 far upstream to u_1 far downstream at the exit area, leading to the expansion of the stream lines downstream of the rotor. This slowing of the flow is induced by a discontinuous pressure drop Δp over the rotor. The pressure recovers downstream to atmospheric level p_0. This drop in pressure causes a thrust force acting over the rotor area in the streamwise direction.

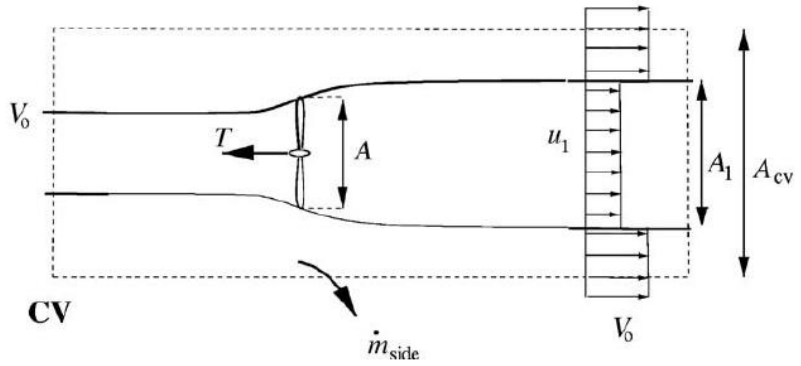

Figure 2.2: Circular control volume [18].

$$T = \Delta p A \tag{2.1}$$

Due to the assumptions of the flow and the absence of additional forces working on the flow, the Bernoulli equation is valid from far upstream to just in front of the rotor and again from just after the rotor to far downstream. The Bernoulli equation, with our assumptions, can be written as:

$$p + \frac{1}{2}\rho v^2 = const \tag{2.2}$$

Applied to our system, for far upstream to just in front of the rotor:

$$p_0 + \frac{1}{2}\rho V_0^2 = p + \frac{1}{2}\rho u^2 \tag{2.3}$$

and from just after the rotor to far downstream:

$$p - \Delta p + \frac{1}{2}\rho u^2 = p_0 + \frac{1}{2}\rho u_1 \tag{2.4}$$

Combining the equations leads to:

$$\Delta p = \frac{1}{2}\rho \left(V_0^2 - u_1^2\right) \tag{2.5}$$

The control volume to be used and to which we will apply the axial momentum equation can be modelled as a cylindrical control volume, as shown in figure 2.2.

Applying the conservation of mass to the control volume (CV), we have:

$$\dot{m} = \rho u A = \rho u_1 A_1 \tag{2.6}$$

$$\rho V_0 A_{cv} - \dot{m}_{side} = \rho u_1 A_1 + \rho V_0 (A_{cv} - A_1) \tag{2.7}$$

giving,

$$\dot{m}_{side} = \rho A_1 (V_0 - u_1) \tag{2.8}$$

Applying the axial momentum equation in integral form to the CV, we now have:

$$\frac{dP}{dt} = \frac{\partial}{\partial t} \int\int\int_{cv} \rho V d(Vol) + \int\int_{cs} V \rho V \cdot dA = F_{ext} + F_{press} \tag{2.9}$$

where P is momentum and V velocity, *d(Vol)* an infinitesimal small volume and dA infinitesimal small area. F_{ext} refers to the external force acting on the CV and F_{press} the axial component of the pressure force. The first term in equation 2.9 is equal to zero as flow is stationary and F_{press} acts on both sides with equal strength, but in the opposite directions, thus reducing it to:

$$\int\int_{cs} V \rho V \cdot dA = F_{ext} \tag{2.10}$$

Now applying equation 2.10:

$$\rho V_0^2 (A_{cv} - A_1) + \dot{m}_{side} V_0 - \rho V_0^2 A_{cv} + \rho u_1^2 A_1 = -T \tag{2.11}$$

Substituting equation 2.8 into equation 2.11 and solving yields:

$$T = \rho u_1 A_1 (V_0 - u_1) \tag{2.12}$$

Now applying equation 2.6,

$$T = \rho u A (V_0 - u_1) \tag{2.13}$$

Substituting equation 2.13 into equation 2.1, and the result for Δp into equation 2.5 produces the velocity relationship:

$$u = \frac{1}{2}(V_0 + u_1) \tag{2.14}$$

Equation 2.14 states that the axial velocity through the rotor is the mean of the upstream and downstream velocities.

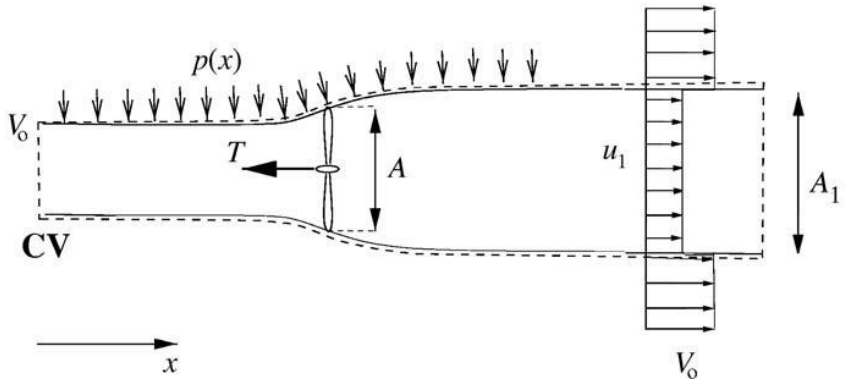

Figure 2.3: Alternative control volume [18].

An alternate control volume can now be devised that follows the streamlines over the rotor. This is illustrated in figure 2.3.

From this CV it can be seen that the F_{press} term in equation 2.9 is unknown and therefore cannot be neglected, hence:

$$T = \rho u A(V_0 - u_1) - F_{press} \tag{2.15}$$

The physical problem being the same as in the previous CV, and comparing equation 2.15 to equation 2.13 it is concluded that the net pressure force contribution along the streamlines are zero. For this CV, no mass flow occurs over the CV boundaries. According to the work-energy theorem, if a force acts on a body and causes its kinetic energy to change, the shaft power (mechanical energy) can be given by:

$$P = \frac{1}{2}\dot{m}\left(V_2^2 + \frac{p_2}{\rho} - V_1^2 - \frac{p_2}{\rho}\right) \tag{2.16}$$

Applying this to the current CV and substituting equation 2.6, it yields:

$$P = \frac{1}{2}\rho A u(V_0^2 - u_1^2) \tag{2.17}$$

The axial induction factor a is defined as the ratio in the reduction of velocity at the rotor plane over the upstream velocity:

$$a = \frac{V_0 - u}{V_0} \tag{2.18}$$

Theoretically a can vary from one to 0 as u varies from a minimum of 0 to a maximum of V_0. Rewriting equation 2.18 and using equation 2.14 leads to the following expressions:

$$u = V_0(1 - a) \tag{2.19}$$

$$u_1 = V_0(1 - 2a) \tag{2.20}$$

Adding these to the power and thrust equations, yields:

$$P = 2\rho A V_0^3 a(1 - a)^2 \tag{2.21}$$

$$T = 2\rho A V_0^2 a(1 - a) \tag{2.22}$$

The available power in the rotor area A is the kinetic energy of the flowing fluid.

$$P_{avail} = \frac{1}{2}\rho A V_0^3 \tag{2.23}$$

The power coefficient can now be formulated as being the ratio of measured power over theoretical power, hence:

$$C_p = \frac{P}{P_{avail}} = \frac{2\rho A V_0^3 a(1 - a)^2}{\frac{1}{2}\rho A V_0^3} \tag{2.24}$$

which leads to,

$$Cp = 4a(1 - a)^2 \tag{2.25}$$

Similarly, the thrust coefficient can be defined as:

$$C_t = \frac{T}{T_{avail}} = \frac{T}{\frac{1}{2}\rho V_0^2 A} = \frac{2\rho A V_0^2 a(1 - a)}{\frac{1}{2}\rho V_0^2 A} \tag{2.26}$$

and,

$$C_t = 4a(1 - a) \tag{2.27}$$

Now C_p can be rewritten in terms of C_t and a:

$$C_p = C_t(1 - a) \tag{2.28}$$

To find the maximum C_p we differentiate with respect to a and set the result equal to zero:

$$\frac{dC_p}{da} = 4(1-a)(1-3a) = 0 \tag{2.29}$$

It can be seen that when $a = \frac{1}{3}$, $C_\mathrm{p} = 0.593$. The relationship between a versus C_p and C_t is illustrated in figure 2.4.

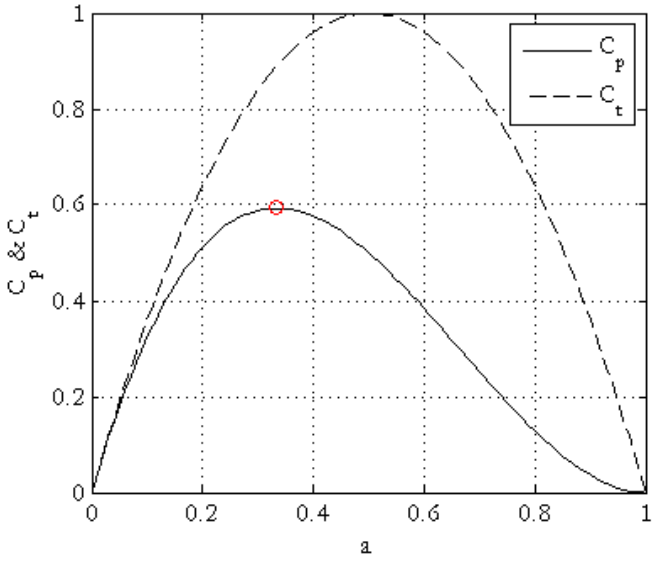

Figure 2.4: C_p and C_t versus a.

Expanding this to shrouded or diffuser-augmented turbines, Hansen [18] proposed that if a cross-section of the diffuser is shaped as an airfoil, a lift force will be generated and will accordingly increase the velocity of the fluid passing through the diffuser. This will increase the mass flow and consequently the energy density of the extractable kinetic energy per rotor area.

Fundamental to Hansen's argument is the use of an augmentation factor defined as $\varepsilon = u/V_0$, retaining the convention of the preceding derivation. Applying equation 2.24 and equation 2.26 to the diffuser-augmented turbine, we find:

$$C_{p,d} = \frac{P}{\frac{1}{2}\rho A V_0^3} = \frac{Tu}{\frac{1}{2}\rho V_0^2 \frac{V_0}{u} uA} = C_T \varepsilon \tag{2.30}$$

Combining equation 2.28 and equation 2.30 yields:

$$\frac{C_{p,d}}{C_{p,b}} = \frac{\varepsilon}{(1-a)} \tag{2.31}$$

Applying the following mass flow ratios we find:

$$\frac{\dot{m}_b}{\rho A V_0} = \frac{\rho A(1-a)V_0}{\rho A V_0} = 1 - a \tag{2.32}$$

$$\frac{\dot{m}_d}{\rho A V_0} = \frac{\rho A u}{\rho A V_0} = \varepsilon \tag{2.33}$$

When combining the above three equations, one concludes with:

$$\frac{C_{p,d}}{C_{p,b}} = \frac{\dot{m}_d}{\dot{m}_b} \tag{2.34}$$

Equation 2.34 states that the factor increase in C_p is directly proportional to the increase in mass flow through the diffuser-augmented rotor. This relationship was verified by CFD studies conducted and is presented in [21]. In order to design an optimised diffuser, the critical aspect that will determine what factor increase in kinetic energy extraction is achievable, is related to the ability of the diffuser to increase the fluid inflow velocity and consequently increase the mass flow through the rotor area.

Using Betz's law as validation, a CFD rotor model will be selected and a numerical investigation conducted in the design of the diffuser of this current study. The derivation has been presented, highlighting equations such as the power coefficient (C_p) to be used in design analysis as well as a proposed argument in obtaining increased power extraction from a turbine if using a diffuser. To design an optimised diffuser, literature that pertains to OCTs needs to be conducted. A review of literature will be presented in the next section.

2.3 Review

The structure followed in the review starts broad, considering OCTs objectively; providing an overview of the current state of the technology, and narrowing down to similar studies conducted in recent research. Continuing from the background information provided in Chapter 1, a more in-depth discussion will now be presented by using the same manner of discussion as followed by Rourke [4].

2.3.1 The State of Ocean Current Turbines

Various devices are being investigated to extract fluid motion caused by wave motion and steady flow ocean current, ranging from reciprocating to rotary devices. Although

differing in operational method, all of these utilise the hydrodynamic forces induced by the fluid environment to extract kinetic energy [27].

Rotary devices utilise the same underlying physics involved in wind turbines and are similar in design principle. They rely on inflow of fluid causing a hydrodynamic force over the turbine blades. This technology is associated with ocean and marine current flow and is thus the area of focus. Two sub-categories exist for rotary devices; namely horizontal axis turbines having the rotary axis parallel to the flow, and crossflow turbines, where the rotary axis is perpendicular to the flow; one configuration being vertical.

Horizontal axis OCT rotors consist of multiple blades and current prototypes range from two-bladed [28, 29] through to 16-bladed designs [30]. Blade configurations for horizontal axis OCTs range from having variable pitch design, which uses active pitch control to limit the maximum power output of a turbine by adjusting the pitch, or fixed pitch design, which uses the occurrence of stall of the rotor at a certain flow speed to limit the maximum power production. The number of blades used is evaluated similarly to wind turbines and is decided upon the basis of economic viability and force balances (Rourke *et al.* [31, 28]).

Vertical axis OCTs are generally of the Darrieus turbine type, having straight-bladed [32] rotors. A variation to the Darrieus turbine arises by arranging the blades as a triple helix as shown in Gorlov [33], known as a "Gorlov turbine". The Gorlov turbine, unlike the Darrieus turbine, has self-starting capabilities. An advantage of this turbine is that the drive shaft protrudes above the water surface due to the vertical alignment of axis, thus needing less submerged parts and increasing the ease of access to the complete drive train (Rourke *et al.* [4]).

Depending on application area and design speed, installation location can differ considerably. Due to depth of water and the type of turbine used, various mooring systems exist. In general four systems are utilised: a gravity mooring system; tripod and bipod mooring (Clarke *et al.* [34]); monopile and bipile structure [8, 35], and a floating structure.

Having installed a turbine system, the power take-off system differs between concepts. OCTs generally have slow rotational speeds requiring the use of a gearbox. Some rim generators, as used in Open Hydro's Open Center Turbine, utilises no gearbox since a direct drive is implemented [36]. Conversion of mechanical energy (shaft) to electrical energy is accomplished by using a synchronous or asynchronous motor for a three-phase power transmission. With the introduction of high voltage direct current transmission lines, some concepts can however utilise DC generators (Bresesti *et al.* [37]) and further.

Selecting a site that suffices as a viable resource and not just as a theoretical resource depends on contributing factors. This includes gross energy content of the flow, as locations

having a flow speed between 1.5 - 2.5 m/s are considered exploitable [38, 39]. Proximity to shore grid connectivity and electrical demand; seabed conditions and interference with shipping routes are all factors to consider in site location. In addition, typical application of current prototypes are designed for minimum depth levels of 30 m, hence limiting the size of turbines and reducing possible usable locations [40, 35, 31].

Estimates based on satellite altimetry establish the amount of power dissipation in kinetic energy on the North-West continental shelf of Europe to be 219 GW [41]. Some estimates place Canada's potential at 50 TWh/year and (Bedard *et al.* [42]) have recently suggested that the initial resource estimation of 12 TWh/year (1.4 GW) for the United Kingdom (UK) is incorrectly computed due to an inaccurate numerical model and a figure of 20 GW is suggested to be more representative of the extractable power around the British Isle's [43].

Resource assessments are currently being conducted by Eskom on the Agulhas current. Findings point to average velocities of 1.63 m/s up to a peak velocity of 2.5 m/s and a potential kinetic energy resource of 600 GW for the current [6]. Having an installed electrical capacity in South Africa of 42.7 GW [44], further investigation into the resource exploitation is warranted by the large electrical potential in the Agulhas current. Being 10 to 50 km from the coast of South Africa, however, it poses problems on installation; operations; maintenance, and grid connection.

With regard to environmental impacts on the current resource environment; due to slow rotations, some as low as six to eight rpm [45], the impact on the surrounding environment and aquatic life is minimal according to Rourke *et al.* [4]. Some concerns include interruption to hydrological and sediment regimes, and restriction of animal movements Cada *et al.* [46].

OCT technology has only recently been investigated and developments in the past decade have seen several start-up companies attaining prototype testing level. Greater commercial deployment will inevitably reduce the cost of OCTs and will allow it to compete with conventional power generation methods [28, 4]. Table 2.1 gives a short overview of current leading technologies.

There are currently 75 listed developers of OCT technology on the European Marine Energy Centre's recent developers list, with future ventures being envisioned as the commercial level of deployment is being reached [47]. The seven devices listed in table 2.1 are those found to be in an advanced developmental stage and closest to commercial level deployment. In particular the SeaGen and AK-1000 devices are leading the product readiness phase in the market.

Table 2.1: Some OCT developers and current status.

Device(s)	Illustration	Features	Status
SeaGen [29]		Twin two-bladed Ø 16m rotors. Rated 1.2 MW at 2.4 m/s	1.2 MW full-scale prototype installed April 2008
AK-1000 [45]		Twin three-bladed Ø 18 m rotors. Rated 1 MW at 2.64 m/s	1 MW full-scale prototype installed August 2010.
Evopod Tidal Turbine [48]	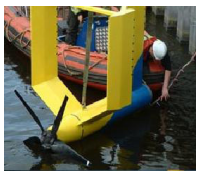	Three-bladed Ø 1.5 m rotor.	35 kW 1/10th model tested.
Lànstrøm AS300 [49]		Three-bladed Ø 6 m rotor.	Rated 300 kW at 2.5 m/s. Installed 2003. Needed no maintenance after four years of operation.
Open Center Turbine [50]		Multi-bladed Ø 6 m rotor.	1/4 scale prototype installed. Rated 250 kW. 2006
Free Flow System Turbine [51]		Three-bladed Ø 5 m rotor.	Full-scale prototype.Rated 35 kW/ turbine. 2008
Gorlov Helical Turbine [52]		Three-bladed helical turbine. Ø 1 m X 2.5 m	Prototype tested. Rated 10 kW at 2 m/s. 2002

2.3.2 Studies on Diffuser-Augmented Wind Turbines and Ocean Current Turbines

The focus of the review will now turn towards research conducted a the development of diffuser-augmented OCTs, wind turbines and RKTs. The current research is a design

project and it is thus necessary to investigate some methods used in evaluating OCTs or similar technologies such as wind turbines. Limited information exists on the large-scale implementation of diffusers on OCTs in the open literature. Diffuser augmentation of wind turbines has however been investigated to a larger extent, and findings and modelling techniques can be used from previous diffuser-augmented wind turbine projects in order to aid the design and development of OCTs.

One of the most well-known research results on diffuser-augmented wind turbines was conducted by Igra and presented in [53, 15]. Having a relatively low power density, air requires a relatively large rotor in a bare turbine setup to extract meaningful amounts of energy [53]. Due to cost in manufacturing, however, the rotor size is limited leading to the idea that if power density can be increased for a given power rating, a smaller rotor can be used.

A theory regarding diffuser-augmented turbines was also developed in Igra [53], and is similar to Jamieson [14] in concluding that there exists an optimum turbine load factor for a given diffuser augmented system. Design points followed in his early studies noted that for an optimum diffuser and shroud shape, two factors are critical. The diffuser exit pressure at the diffuser exit plane should be as low as possible; and for a given diffuser area ratio shroud efficiency should be as high as possible.

In the experimental work conducted by Igra, various concepts were investigated. The first was a conical straight wall diffuser having an expanding inclination angle of 12.6^{o} with three small chord annular airfoils (flaps) at diameters larger than the diffuser exit area, see figure 2.5. To simulate the rotor, a gauze screen is used. This configuration caused a small gap between the diffuser and flaps that accelerates part of the outer flow and directs it into the diffuser wake; effectively bleeding the outer airflow into the wake and re-energising the boundary layer attached to the inside of the flaps. This resulted in a reduction of the diffuser exit pressure and a consequent increase in airspeed and mass flow through the rotor. A measured increase in power production by a factor of 2.9 was recorded for a diffuser area ratio of two.

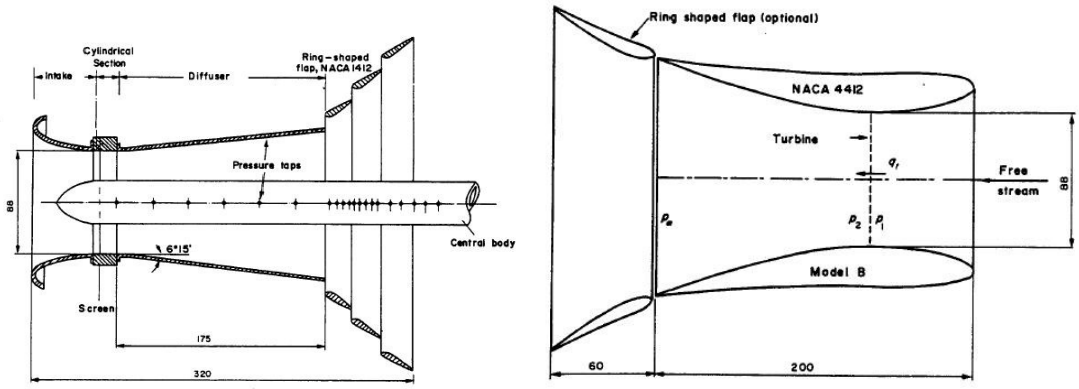

Figure 2.5: Experimental layout of turbine shroud concepts [53].

Other experiments included in the same study considered the use of two annular airfoils without the straight wall diffuser but with larger chord lengths than the flaps in the previous experiment. Arranging them in two different diffuser area ratio configurations of 3.22 and 4.7, an augmentation factor of two and 2.5 were recorded respectively, thus being more compact and illustrating the effective boundary layer control achieved by use of bleed slots. Various other experiments were conducted and augmentation factors of two to four were reported for diffuser area ratios ranging from one to 10. Igara notes in his results that there exists a diminishing trend in augmentation factor versus diffuser area ratio, but not as abruptly as reported in Gaden & Bibeau [9]. From the experiments conducted by Igra [53, 15] he concludes that a significant augmentation is achievable and that the use of bleed slots improves the augmentation over concepts without bleed slots. The peak power now occurred at higher tip speed ratios and thus also reduced tip speed losses. Igra [53] suggests that there is a need for research on the optimisation of the geometric shape of the diffuser.

Using a turbine rotor in the experiments instead of a screen, the diffuser-augmented turbine produced more power than the screen simulation predicted. In Fletcher [54] it is argued that this phenomenon can be attributed to the use of a screen to simulate energy extraction (pressure drop at rotor plane), but is incapable of simulating the favourable effects of wake rotation on boundary layer control [54]. Fletcher also found the effect of increasing diffuser area ratio improves power output, but at a diminishing rate. A power improvement of 30% was recorded in numerical studies.

The diffuser concept on wind turbines was further pursued by a New Zealand company Vortec [55, 56]. A full-scale model, Vortec 7, was built and monitored, recording a power increase of two corresponding to a measured C_p value of 0.62 and a diffuser area ratio of 2.78.

In Schaffarczyk [57] a CFD study was conducted to determine blade rotor performance.

A 3D domain was created using the commercial software CFX and Fluent to simulate the diffuser-augmented turbine. For the rotor an actuator disk model (momentum source) was used and validated against the modified BEM theory and found to be in good agreement. In addition a 2D-axisymmetric CFD model was also implemented and validated against wind tunnel gauze screen tests, and good agreement existed between the two data sets. A slight overestimation of velocity at the rotor plane was predicted by the CFD model and is attributed to the presence of turbulence in the wake. A C_{p} value of 0.8 for a diffuser area ratio of three was recorded in tests [57].

So far, diffuser concepts having little to no space between the rotor blade tips and diffuser have been reviewed. In Bet & Grassman [17] another concept, termed "a partially static turbine", is introduced. This is a diffuser system with greater tip clearance, allowing flow around the rotor to influence the low pressure region behind the rotor. By allowing flow into the low pressure region at higher velocity, the pressure needs to decrease, thus increasing the pressure drop over the rotor and consequently spurring an increase in velocity through the rotor [17].

A CFD investigation conducted in [17] used a wedge-shaped domain modelling a single blade. Additionally, the grid density was increased by a factor of 10 around the rotor area and diffuser, and consisted of 40 000 cells. The design was aimed at minimising the axial length of the diffuser, and used small chord length annular airfoils. It allowed a tip clearance of 37 % of the rotor radius. A power increase of two was achieved with a corresponding diffuser area ratio of 1.69.

Follow-up studies in [13] showed that Kaplan turbines using a partially static diffuser yielded a factor power increase of 2.94. Grassman measured a massflow considerably less than 2.94, thus contradicting equation 2.34 as the amount of power increase is not directly proportional to the increase in massflow.

CFD and experimental investigations in [58, 59] indicated a large discrepancy between CFD results and experimental data. An over-estimation of 30 % was predicted by most CFD results. This was however attributed to a lack of reliable experimental data that suffered from repeatability inherent to the test setup. For the CFD, an unstructured mesh consisting of 500 000 tetrahedral cells was used. Periodic side conditions were imposed along with using an upwind-differencing scheme and k-ε turbulence model.

A strong turbulence presence was observed in the wake of the diffuser. The rotor was modelled using an existing bare wind turbine and it was found to increase power by 20 %. After redesigning the blades, however, an increase of 55 % - 100 % was noted. From this it can be concluded that the use of optimised turbine rotor blades, specific to a given diffuser, is necessary. This also supports the claim made in [14, 53].

A study conducted in Japan by Matsushima [12] utilised a straight wall diffuser with an added vertical flange outer ring at the end. This can be seen in figure 2.6.

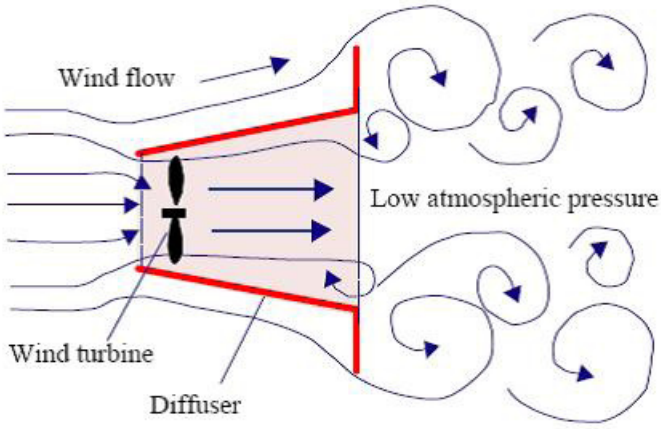

Figure 2.6: Schematic cross-sectional view of a diffuser and wind speed increase mechanism [12].

The method utilised to investigate the characteristics of the diffuser turbine interaction used a CFD study. The commercial software used was I-DEAS in conjunction with Fluent, and the domain chosen; a 2D-rectangular space with dimensions 10 m by 20 m. A constant velocity inlet condition was used. The idea was to optimise for three parameters namely the diffuser inclination angle (0^o - 12^o); flange height (0.1 m - 0.5 m), and diffuser length (2 m - 4 m). The results concluded that for diffuser angles of 0^o - 4^o a sharp rise in augmentation is observed, after which it diminishes and drops off with the onset of boundary layer separation.

Results indicated an increase in rotor axial velocity of 1.4 without the flange, and with the flange a factor of 1.7 [12]. An increase in diffuser length furthermore increased the axial velocity at the rotor, thus predicting a total increase in power by a factor of five. After a model was constructed, a factor increase of only 2.4 in power production was recorded [12]. This disagreed strongly with the predicted CFD results.

From the literature consulted thus far, it is concluded that some discrepancy between CFD models and experimental results exists. This discrepancy is attributed to CFD models where turbulence has a strong presence, as the CFD formulation of turbulence models cannot explicitly predict the point of flow transition and separation (Benjanirat *et al.* [60]).

Various turbulence models exist in commercial software and a study evaluating these models applicable to wind turbines was investigated. The Baldwin-Lomax, Spalart-Almaras and k-ε model were investigated in [60], considering the flow over rotor blades for fully

attached flow and severely separated flow. It was found that the k-ε model predicted the experimental rotor results the most accurately.

In the preceding literature, optimisation was used to determine the optimal diffuser geometry. This was however limited to very crude parametric studies where a given set of variables (for instance diffuser inclination angle and diffuser area ratio) were optimised by fixing all variables except one and optimising the excluded variable. This process was repeated until all variables were optimised [12, 59, 9]. This methodology neglects the interaction (interdependence) between variables.

A design of diffuser shapes in Madsen *et al.* [61] for incompressible flow was conducted, utilising a design space developed by the D-optimality criterion and analysed using CFD [61]. A metamodel was then fitted through the design space using a response surface (RS) approximation, after which the optimum was determined using numerical optimisation. A two- and then a five-variable design was conducted; all variables being defined as geometric variables characterising a B-spline and hence determining diffuser shape. It was concluded in Madsen *et al.* [61] that the RS technique smoothed out the numerical noise associated in different CFD analyses. RS approximations allowed interaction between variables to be studied and to consequently arrive at a more global optimum.

A parametric study on a horizontal axis RKT utilising a diffuser was conducted in Gaden & Bibeau [62, 9]. The authors argue that contrary to wind turbines, a size limit is imposed on OCTs due to bathimetry and seabed depth. The use of aerodynamic devices such as diffusers to increase the power density can therefore have positive power production consequences where installation size is limited. OCT technology is not just used in ocean currents but also in rivers, tidal currents and man-made channels; a versatility that allows its application area at sites not possible with other technologies.

Gaden & Bibeau [9] further propose a straight wall diffuser design (see figure 2.7) where the objective is to maximise the mass flow through the rotor to consequently increase the power density and the consequent power extraction. The design and optimisation of their diffuser was approached using CFD analysis. A momentum source was used for the rotor and validated against the Betz theory. A close correlation was observed but with a 5 % over-prediction of the overall turbine performance in Gaden [62], but agreement was enough to validate the use of the model.

For the CFD 3D model an upwind-differencing scheme was used along with the k-ε turbulence model, employing near-wall effects. The mesh consisted of tetrahedral and hexahedral elements and total cell count was approximately 713 000. The momentum source model that was used only extracted the amount of energy specified by an existing model's maximum output; thus effectively maximising a turbine for one flow situation (in this case, $C_{\mathrm{p}} = 0.35$). The optimisation method used two variables, namely diffuser area ratio

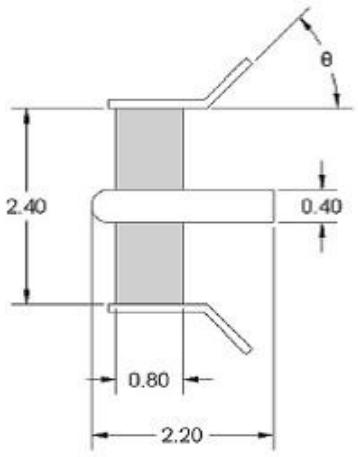

Figure 2.7: Illustration of Gaden turbine from [9].

and diffuser angle. The angle was first fixed and then the diffuser area ratio optimised. After achieving the best diffuser area ratio the angle was then optimised. In total, 25 different analyses were executed, each having an unique diffuser shape.

Results for the increase in power with increase in diffuser area ratio showed that a factor increase in power of 2.5 is achievable for a corresponding diffuser area ratio increase of 1.4; after which the improvement levels level out sharply. This level out effect was attributed to the onset of flow separation at diffuser area ratios greater than 2.5. The effect of drag versus diffuser area ratio was also investigated and showed an almost linear increase from approximately 6 kN to 150 kN corresponding to diffuser area ratios of one and 6.2 respectively.

In Gaden's chosen design an increase in power by a factor of 3.1 was achieved at a diffuser area ratio cost of 1.56 and a drag increase of 3.9 [9]. Gaden showed that for the same diffuser, if a rotating reference frame is used to model a geometrically accurate rotor, a power increase of only 1.5 is achieved. From [62] experiments were conducted on a diffuser with a shroud without the presence of a rotor. Validation of the CFD models was attempted but not achieved. However with a 45^{o} diffuser angle, diffuser area ratio of 6.25 and no rotor the velocity where the rotor would have been placed, was found to increase by approximately a factor of 1.2 to 1.4 over the free stream velocity.

This concludes the review. A summary of the most important findings and how they relate to the current study will be presented in the next section.

2.4 Conclusion

As can be deduced from the aforementioned literature, OCT technology is still in its infancy stage. No commercial expansion of such concepts currently exists, although a number of companies have completed or are busy with full-scale prototype testing.

Rouke *et al.* [4, 47] point out that 75 developers of OCT technology exist. The most pursued OCT configuration is the horizontal axis turbine, followed by vertical axis turbine. As far as could be ascertained from available literature, in terms of rated power of full-scale prototypes, horizontal axis turbine surpasses vertical axis turbine's popularity. Some OCT prototypes already incorporate a diffuser utilised not only for its improvement in power generation but also for its structural benefits as attachment device, or forming an active part of the generator (direct-drive stator). The geometry of the diffuser however being basic in design and possible to optimise further into a more complex shape.

Limited knowledge regarding the use of diffusers on horizontal axis OCTs exist in the available literature, but due to the similarity to wind turbines, diffuser augmentation of wind turbines were explored. This was conducted to gain insight into possible pitfalls, shortcomings and acceptable design methods and tools used with regard to diffuser-augmented turbines in OCTs.

From the studies of Igra [53], Grassmann [59, 58, 13] and Matshushima [12], two distinct designs emerged in diffuser shape. One is the utilisation of annular airfoils with or without bleed slots and, secondly, inclined straight wall diffusers with or without a flange. Gaden [62] suggested the use of a curved plate diffuser. Interestingly, Grassmann [13] found that the factor increase in turbine power production was not similar to the factor increase of mass flow through the rotor.

Most studies of diffuser-augmented wind turbines implement CFD and/or a 1D-analysis of the diffuser-augmented turbine. For the CFD varying between 3D-, 2D- and 2D-axisymmetrical grids but most employing unstructured grids and the k-ε turbulence model. From CFD results, improvements of a factor 1.2 to 4 were noted. Compared to the related experimental tests, the CFD results differed in accuracy but provided valuable insight into the underlying physics involved. An improvement in power of 2.4 has been recorded experimentally for rotors with a power coefficient $C_{pmax} < 0.35$. For rotors with high-efficiency ($C_{pmax} > 0.4$), improvements were less prominent. Most studies suggested optimisation of diffusers and/or rotor blades to achieve higher power increases.

Studies using optimisation to design a wind turbine diffuser or OCT diffuser have been limited to low variable count, simple geometry (straight wall) and a crude technique (parametric study). Using this type of optimisation technique reduces the interdependence of the variables, and constrains the design problem too excessively and a solution is

found based on only a few function evaluations (30 or less). None employed the use of a metamodel as used in Madsen *et al.* [61].

To summarise, OCT technology is being pursued not simply on a research level, but also on a commercial level. The usefulness of employing a diffuser also lies in its ability to increase the power density if the installation environment is limited. The use of a diffuser however has to be weighed against the economic effects it will have on prototype cost as opposed to simply employing a larger rotor of similar outer diameter to the diffuser-augmented turbine's diffuser outlet diameter; or using multiple small rotors similar in size to the diffuser-augmented turbine's rotor.

In reference to the above, this research undertakes to design an optimised diffuser employing a more rigorous optimisation approach than parametric studies, thereby contributing to current investigations into this area of research.

The researcher will attempt to exceed previous augmentation factors for a high-efficiency rotor and to explore the limits of possible maximum augmentation for a given diffuser area ratio. This will attempt to address the question of how much augmentation is possible for a given diffuser area ratio, thus providing an improved design methodology for future research and development, and providing data that has been compared to experimental findings for future analysis.

Chapter 3

Research Design and Methodology

3.1 Introduction

From the previous chapter it can be seen that the various research methods used in diffuser-augmented turbine studies differ in approach. In this chapter the researcher hopes to highlight some research methods encountered in literature to also supply the motivation behind and details regarding the approach selected for this research.

To reiterate, the purpose of the thesis is to increase the power density of fluid passing through an existing OCT rotor design by using an optimised diffuser design to effectively increase the power output from the model turbine rotor used in [16, 11] by a factor of two or more.

This chapter starts with an overview of previous research designs in the field of diffuser-augmented turbines and then moves on to the chosen design for this research. This project was subject to various limitations that will be briefly discussed, followed by some concluding remarks.

3.2 Research Design

To examine the effects of diffusers on the power augmentation of turbines, various design techniques have been applied. Generally, however, the approaches consist of three distinct parts; the numerical prediction and evaluation phase; then the developmental phase, and finally the experimental testing phase.

The numerical prediction and evaluation phase consists mainly of identifying a suitable numerical model from which a DOE can be created in some manner. In the developmental

phase, some form of evaluation and development occurs, resulting in an optimal design. The final stage consists of constructing a physical test model.

In the first phase some form of numerical tool is used to evaluate the diffuser performance and to estimate the expected experimental data. This ranges from implementing 1D-theory [53] to using more modern techniques, like CFD [59, 9, 57, 12], that are specific to the geometry. In the 1D-theory approach the diffuser shape is ignored and the ability of the diffuser to increase the power output of a turbine is determined by using only two parameters, namely the diffuser exit pressure (C_{pe}) and the diffuser efficiency parameter (η). Igra [53] then formulates the factor increase in power as:

$$r_{max} = 0.649 \left[\frac{(1 - C_{pe})^3}{1 - \eta \left[1 - \left(\frac{A_t}{A_e} \right)^2 \right]} \right]^{1/2} \tag{3.1}$$

A_{t} is the turbine swept area and A_{e} is the diffuser exit area. The maximum power increase factor is r_{max}, achievable for a given set of C_{pe} and η.

In order to calculate the values of C_{pe} and η correctly, an experimental test needs to be conducted from which C_{pe} and η can be measured and then applied to equation 3.1 to estimate the power increase factor. This formulation is useful as small-scale diffusers can be built and tested, and if an appropriate shape has been found with the best parameters, only then is it necessary to build a bigger model diffuser. This is however a time-consuming process that fails to allow for minor adjustments to be made quickly and also requires an extensive experimental setup to acquire the C_{pe} and η parameters.

With improvements to the Navier-Stokes CFD solver codes and computing power, CFD provides increasingly accurate insight into fluid flow problems. Not only being utilised for the insight it provides into fluid flow problems, it is progressively being applied to redesign concepts and to enhance performance [61]. The use of CFD as a numerical design tool has recently been used extensively for conducting a design of experiments (DOE) for diffuser shapes [12, 9].

Instead of having to build small model diffusers and following a trial and error DOE as used in Igra [53], numerical experiments can be conducted using CFD. This process offers the advantage of being able to execute various designs in a much shorter time frame than physical experiments would allow. Being a numerical model utilising finite volume methods to describe the flow, however, it still lacks accuracy in the prediction of turbine performance - especially in highly turbulent flow - and can only provide approximate solutions. However, comparitive analysis between designs is possible thus still leading to the best design although having an analytical solution only.

Various applications of CFD with different mesh, grid and flow parameters have been conducted. In typical cases a simplified 2D-mesh was used to minimise the computing time. Simplified rotor representation also varied between porous disk (discontinuous pressure jump) or momentum source representation. Momentum source models are more accurate in representation as it takes the rotor characteristics into account; however for our study investigating a more simple formulation so as to arrive at a more generalised conclusion was beneficial as it can be applied to geometrically different rotors with the same performance.

For the turbulence models used in the literature a number of different models were used to address the representation of turbulence in the CFD model. Notably the k-ε, k-ω and Spalart-Almaras model were used extensively and with good results [9, 13, 21, 12, 11]. It was however suggested that a study into turbulence model evaluation, as is applicable to the current study, should be conducted, and thus formed part of the research.

Optimisation in the literature ranged from using sparsely populated DOEs of less than 30 design points to describe a design space of four to three design variables. From available literature, various improved techniques were encountered ranging from particle swarm optimisation or approximation optimisation techniques (metamodelling) such as Kriging or Response Surface modelling (RS). RS modelling seem to be effective in smoothing out noisy response functions [61], but for non-linear functions support vector regression (SVR) modelling has been proposed [63]. From optimisation a diffuser shape should emerge that will have to be experimentally tested according to the research objectives.

To test the proposed diffuser design, the towing tank test facility used at the Department of Mechanical and Megatronic Engineering at Stelenbosch University is to be used. The main reasoning behind this choice is that the facility has been proven to be adequate in retrieving reliable test data in previous experiments [11, 16].

This section highlighted the main techniques used in diffuser design projects. The discussion will now move to elaborate on the chosen method to test the current thesis.

3.3 Methodology

CFD analysis forms the core of the numerical simulation to be used in the optimisation and ultimately determines how effective and reliably the objective of the research can be achieved.

Seen in the context of the optimisation to be carried out, it should be noted that a large number of analyses are required. Having a mesh that accurately captures the flow

effects determining diffuser performance is therefore essential. The mesh should also be as computationally inexpensive as possible to minimise computational time.

3.3.1 Two-Dimensional Axisymmetric Mesh

It was decided to use a 2D-axisymmetric mesh. Since the diffuser shape will be characterised using geometric points, the amount of points needed to be limited, as the design variables that will change for the optimisation will be geometric parameters of the diffuser. Thus if the geometry can be described with as few as possible parameters, the number of variables will be limited and, ultimately, so will the size of the DOE. It was decided to use a curved plate diffuser instead of an annular airfoil diffuser. Another advantage to this approach is that the complexities in manufacturing the diffuser is greatly reduced using the curved plate diffuser rather than the annular airfoil diffuser.

By using the curved plate diffuser configuration the curved line can also be described by as few as three variables through which a spline can be fitted to change the curvature of the plate (two at the ends and one in the middle). In this research a four variable B-spline was selected to describe the diffuser shape. Using four variables allows the curve to have, if required, at least two inflection points and so provide the curve with sufficient geometric flexibility. In addition, the elements used will be of an unstructured grid type so as to ensure consistent grid quality throughout various different diffuser shape simulations.

3.3.2 Rotor Modelling

Having the characteristics of the model OCT turbine rotor available from previous studies [11], the pressure drop according to turbine theory can be calculated across various tip speed ratio (TSR) values. For the optimisation, the chosen design point where the optimum diffuser needs to be calculated, is at the rotor maximum efficiency (highest C_{p}value). A single value for the pressure jump constant is therefore required [62].

As shown in [14] for each discrete rotor loading state exists a unique optimised diffuser shape. Following the proposed optimisation methodology also allowed only one optimised diffuser shape to be generated for a specific rotor loading state. Therefore since the current study aimed to maximise the turbine power production only one rotor loading state needed to be optimised.

To check if this proposed rotor modelling method is acceptable for the CFD analysis, a validation against the 1D-turbine theory is presented in Chapter 2. During this investigation various turbulence models will be used and thus if the rotor model follows the theory correctly, the rotor model is validated. Additionally, the turbulence model used

with the rotor that allows CFD simulation to follow the theory the best, validates the specific choice of turbulence model. Please refer to Appendix A for a discussion on related CFD theory and turbulence models.

3.3.3 Optimisation

Depending on the optimising procedure used, the optimisation process can prove time-consuming [61]. The advantage of using a metamodelling technique such as SVR or RS is that it allows for the evaluation of the entire design space, and for a low design variable count, it is considered computationally less expensive compared to gradient-based search algorithms [64, 61].

This aspect is of particular interest to this study, as having a metamodel means that various aspects of the design space can be investigated, including checking for local optimum designs (if there are any). Due to the uncertainty involved in diffuser design the design problem can be of a highly non-linear nature, thus validating the use of metamodelling techniques.

The predictive capability of any metamodelling technique relies on the distribution of the sampling or training points within the design space [61]. A DOE needs to be constructed that will spread the function evaluations (training points) effectively throughout the design space in an attempt to capture as much of the characteristic design space responses. A space-filling DOE design was therefore chosen; specifically the Latin hyper cube (LHC) design was used in generating training points and the 2D-axisymmetric CFD model was used as the function evaluation. Figure 3.1 provides a simplified overview of the optimisation procedure.

In step 3 depicted in figure 3.1, the simulation of the various CFD analyses can be conducted on a parallel computing environment such as a computing cluster. This entails the automation of mesh adaptation and simulation. To accomplish this, the mesh generated and the simulation needs to be created by using text command scripts or journal files. Journal files contain the commands that are generated when a simulation model is created and executed as text; thus reading a journal file in Gambit or Fluent will produce a mesh or simulate a mesh respectively. Inside the Gambit journal file the key variables describing the diffuser shape can then be altered and changed according to a specific set of variable combinations, as determined by the DOE. A program capable of simplifying this procedure is VisualDOC, which effectively is a process management tool. Using this method, a DOE consisting of a mixture of variable values can be fed into the management program.

The process management tool oversees the creation of various meshes and conducts the

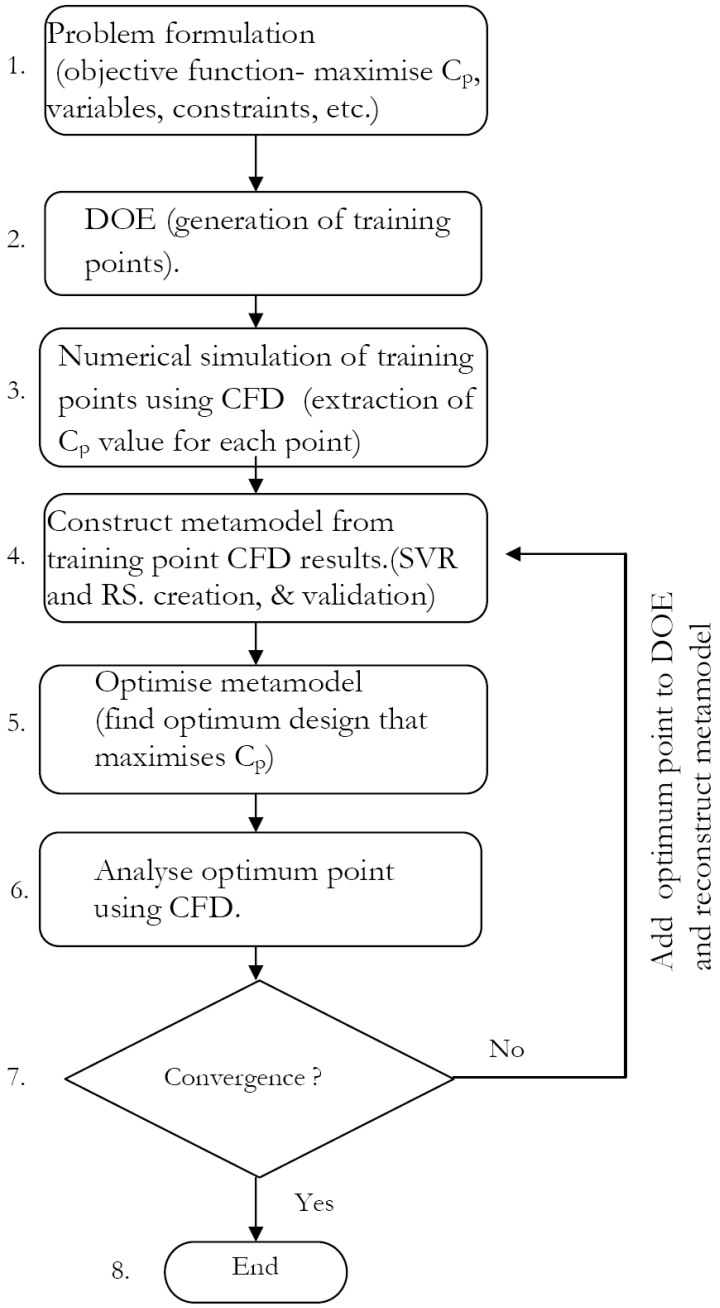

Figure 3.1: Simplified optimisation flow chart.

simulation thereof. It finally extracts the results from the completed CFD analyses and produces the responses (C_{pmax} values) to the DOE. This is in turn used to construct the metamodel and the optimum is then searched for. The construction of the metamodel can be numerically achieved using the numerical toolbox for Matlab as prepared by Viana [65]. An optimum design should emerge from this part of the research.

3.3.4 Finite Element Methods

After an optimum design has been achieved, a detail design can be conducted. To aid in the process of designing the support structure and the test rig, finite element methods (FEM) and topology optimisation can be used. Topology optimisation is a mathematical method that analyses a FEM sub-problem to optimise material layout according to constraints (mass, deflection, stiffness etc.) within a certain design space. The use of topology optimisation will help to identify suitable placements of struts to ensure minimal structural deflection and reliable test results.

By using the results of the CFD, the drag force acting on the diffuser can be calculated. Using this force as input, the diffuser and rig deflection can be approximated. As the diffuser will be made using composites, the thickness required to minimise excessive diffuser shape warping can be calculated using an iterative procedure in thickness application and checking the amount of deflection from various FEM analyses. This should provide a design that can withstand the forces that will be encountered in the towing tank test facility.

3.3.5 Manufacturing

The manufacturing of the diffuser will make use of composites as opposed to steel plates, which will allow the manufacture of more complex shapes. This process will consist of first manufacturing a pattern using CNC machining from which the diffuser lay-up can be made. To save material costs the diffuser will be made in two halves that are later joined together. In addition, the support rig that accommodates the current test turbine will be modified using readily available tubing of an appropriate profile.

3.3.6 Testing

The equipment used in the experimental setup consist of a towing tank trolley, torque transducer, bridge amplifier, tachometer, data-capturing device, and an electric motor that can be used as an electric brake when used in generator mode.

For the transducer and tachometer, calibration tests need to be conducted to ensure the reliability of the test data. In addition, the towing tank trolley's speed needs to be calibrated to accurately simulate the flow speed of the water. Using this equipment the power production of the diffuser-augmented turbine can be accurately captured and will present reliable data for post-processing.

3.4 Limitations

As stated in Chapter 1 the current research is concerned with exceeding the power production as attempted in a previous design project [11]. The diffuser is to have the same geometrical envelope as the previous diffuser, thus fixing the diffuser area ratio of the current diffuser and axial length but not the shape.

CFD analyses using a 3D-accurate model of the rotor and diffuser will be computationally expensive and the time needed to integrate into the optimisation procedure will require more time than the scope of the research allows. The curved plate geometry for the diffuser is consequently investigated and no other diffuser configuration such as an annular airfoil will be investigated.

With regard to simulation software, only a single CFD package was used in the analyses namely the Navier-Stokes solver Fluent with its pre-processor (mesh generator) Gambit. In addition, FEM software included Patran and Nastran as well as the structural optimisation software, Genesis, numerical optimiser and management software, VisualDOC, and numerical software, Matlab and Python were used.

Limitations to the experimental testing include the towing tank length, width and breadth being fixed that will have blockage effects on the turbine; available measurement equipment and water temperature variation.

Due to the large amount of design tools used and individual studies conducted, elaborate discussions into the underlying theory for SVR, CFD turbulence modelling and additional 1D-theories will be restricted to only sufficient explanation so as to understand the results obtained.

3.5 Conclusion

Available research in diffuser design in horizontal axis wind and RKTs have been presented in this chapter. The research design chosen for the current investigation has been discussed and evaluated together with the inherent advantages and shortcomings thereof. More specific methods for each design tool has also been shown, and therefore the methodology governing the study should be evident and endorse the usage and choice of the methods in achieving the research objectives.

Some limitations implied by usage of the methods and other project specifics have also been presented and should illuminate the boundaries within which the current study was conducted. The dissertation now turns to the application of the methodologies discussed in this chapter along with each method's related results.

Chapter 4

Rotor and Turbulence Modelling: Details and Validation

4.1 Rotor Modelling

The modelling of the rotor was done by implementing an infinitely thin disk that causes a discontinuous pressure drop when fluid flows through the disk. To understand how this was accomplished, a short derivation is given below for the pressure jump formulation. In Fluent the pressure jump for a fan [66] is formulated as:

$$\Delta p = \sum_{n=1}^{N} f_n v^{n-1} \tag{4.1}$$

Or, where N = 3, the equation becomes a quadratic polynomial:

$$\Delta p = f_1 + f_2 v + f_3 v^2 \tag{4.2}$$

The pressure jump is Δp, f_n is the polynomial coefficient and v^{n-1} is the axial velocity at the rotor. If we recall equation 2.5, a definition for the pressure jump is given in terms of the axial thrust. We now need to rewrite equation 2.5 so that the only variable is the rotor axial velocity. This can be accomplished by substituting the velocity relations defined in equation 2.19 and 2.20 so that only the velocity at the rotor and the induction factor determines the pressure difference:

$$\Delta p = \frac{1}{2}\rho \left[\frac{1 - (1 - 2a)^2)}{(1 - a)^2} \right] \times u^2 \tag{4.3}$$

The fluid density is ρ, the axial induction factor is a and u is the axial velocity at the rotor. Observe that the coefficient to u^2 in equation 4.3 varies only with induction factor. Thus to simulate the rotor numerically at a specific C_p value, only the corresponding induction factor needed to be computed from 1D-theory and applied to equation 4.3.

To validate this pressure jump rotor modelling technique, CFD simulations needed to be conducted in order to retrieve data and compare to theory.

4.2 Two-Dimensional Grid and Parameters

In general an ideal rotor validation study considers an infinitely small hub at the centre of the rotor, which was vital for this study. For the optimisation simulations, an ideal turbine is not desirable, but one that recreates the model turbine that is to be tested. Determining the performance of the CFD rotor model with hub inclusion versus turbine theory was therefore to be of interest as the ideal assumption of no hub was now violated.

The 2D-axisymmetric grid is displayed in figure 4.1 along with its dimensions and certain boundary conditions. The fluid space was selected in order to minimise the influence of boundaries on the simulation results. Note that the "R" in the figure refers to the radius of the model turbine rotor ($R = 0.4$ m). The Fluent code is based on the full Reynolds-averaged Navies-Stokes equations and various turbulence models will be applied as a closure form. Refer to Appendix B for more simulation details.

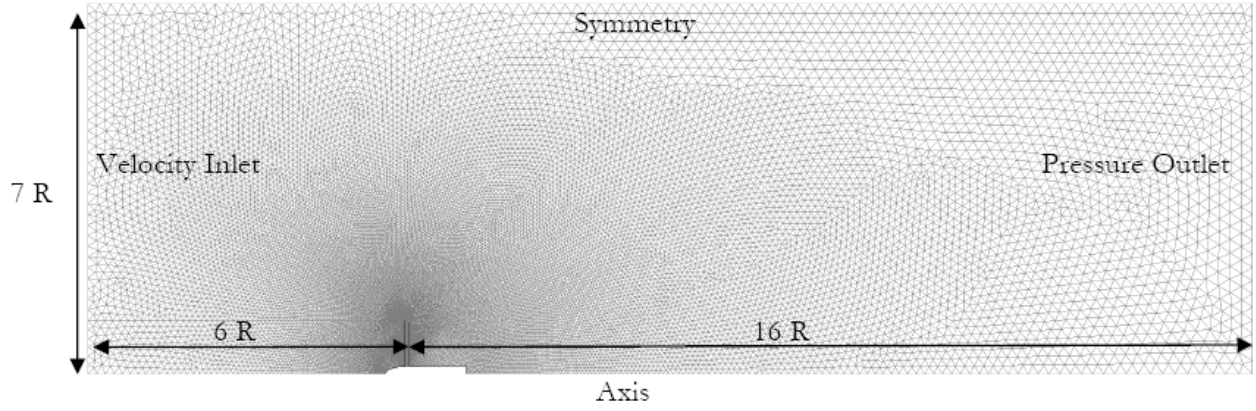

Figure 4.1: 2D-axisymmetric mesh used for rotor model validation.

In order to produce a high quality grid the mesh density distribution was smoothed to minimise the truncation error that occurs between the partial derivatives in the Navier-Stokes governing equations and their discrete approximations. This happens when cell

volume between adjacent cells increases too rapidly which translates to excessive truncation errors. Another quality measure is skewness that is defined as the difference between the shape of the generated cell (actual cell) and the shape of an equilateral (in our case equiangle triangles) cell (ideal cell) of equivalent volume. Values below a skewness index of 0.5 are considered acceptable. Highly skewed cells decrease accuracy and destabilise the solution, slowing convergence and increasing computational time. Aspect ratio is a measure of the stretching of the cell and in [66] it is recommended to avoid ratios exceeding 5:1. Squish is calculated from the vector pointing from the centroid of a cell toward the centre of each of its faces [66]. Values below an index of 0.5 are considered acceptable [66].

Grid dependence tests were also conducted on the mesh to see the influence of mesh density on results. Similarly dimensioned grids as shown in figure 4.1 were constructed that varied in mesh densities from a cell count of 1038 to 58 442. The value used to compare the results is the C_p value as calculated by:

$$C_p = \frac{P}{P_{avail}} = \frac{Tu}{\frac{1}{2}\rho A V_0^3} = \frac{\Delta p A u}{\frac{1}{2}\rho A V_0^3} \tag{4.4}$$

The axial velocity at the rotor is u; Δp is the pressure drop across the rotor; A the rotor swept area, and V_0 is the free stream velocity. The results are presented below in figure 4.2.

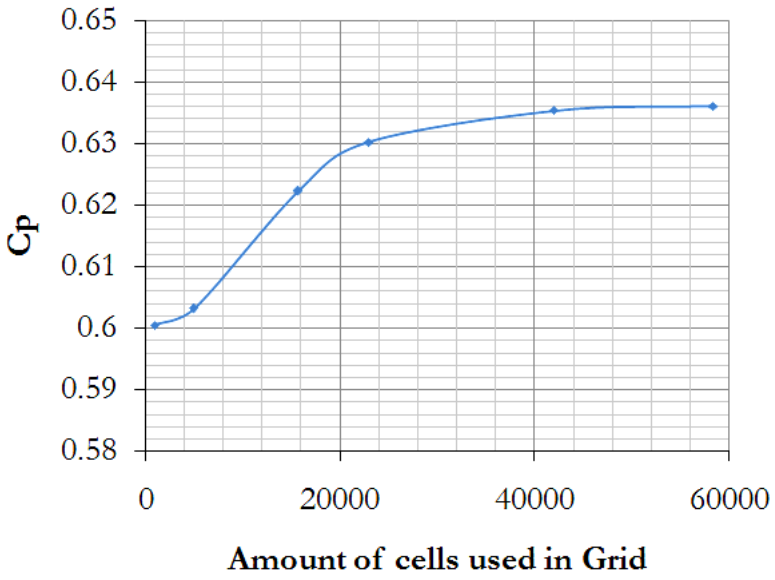

Figure 4.2: Grid dependence for 2D-axisymmetric mesh.

The chosen mesh consisted of 42 464 cells and 63 917 faces. The mesh scheme used is unstructured tri-pave elements. All cells were within excellent to acceptable ranges for maximum skewness (0.48), squish (0.28) and aspect ratio (4.2).

After applying various monitors and setting the convergence criteria that all residuals should be less than 10^{-5}, the simulations were initiated. It was found that for the various turbulence models investigated, convergence was achieved at 3800 iterations. Figure 4.3 shows the axial velocity distribution; where the colour map scale units are m/s.

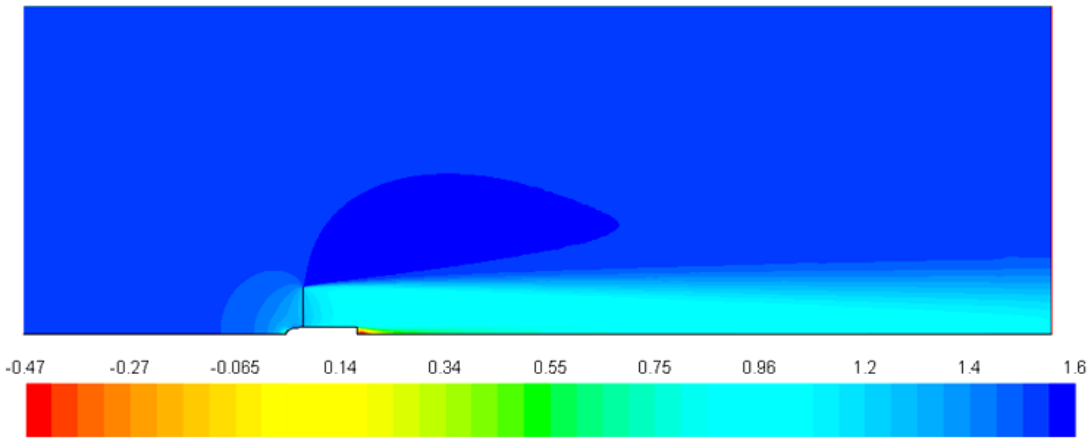

Figure 4.3: Axial velocity distribution (m/s).

Turbulence models investigated include the k-ε realizable turbulence model and the k-ω standard model. The choice of these were motivated from previous studies applying them and indicating good agreement with experimental test data. A laminar solution was also investigated that neglected viscosity effects for a more correct representation of the 1D-theory assumptions.

4.3 Validation Methodology

In order to validate the CFD rotor model, it had to be compared to the 1D-theory derived in Chapter 2.

Glauert [67] found that the normal 1D-theory tends to fall away at induction factors (a) greater than 0.4 or in the turbulent windmill state. To overcome the shortcoming of the 1D-theory he presented an empirical relation for the thrust coefficient C_t versus a for values of $a > 0.4$.

A recent study conducted in Buhl [68] developed a modified empirical relation for the induction factor range of 0.4 to one, and is given as:

$$C_t = \frac{8}{9} + \left(4F - \frac{40}{9}\right) a + \left(\frac{50}{9} - 4F\right) a^2 \tag{4.5}$$

F is a loss factor related to the tip and hub losses. For the present study's purposes, it was selected as 1. Validation was therefore done using 1D-turbine theory for $a < 0.4$ and against the modified Glauert empirical relation for $a > 0.4$.

This theory will also be used to evaluate the turbulence models investigated.

4.4 Results

After simulating, the results obtained from the CFD were then compared to the 1D-theory and the modified Glauert empirical relation for induction values greater than 0.4. These results are presented below in figures 4.4 and 4.5.

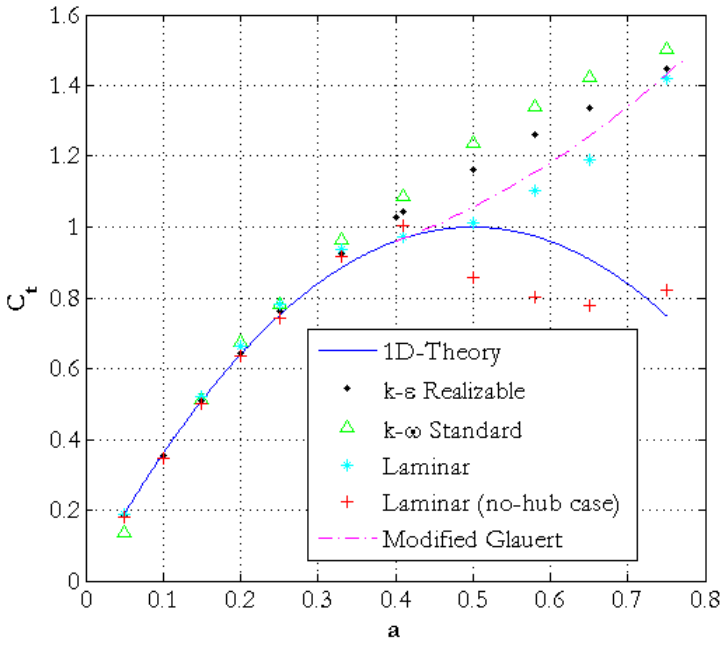

Figure 4.4: C_t versus a graphs showing comparison between rotor theory and various turbulence models.

From the figures it can be deduced that the k-ε turbulence model outperforms the k-ω model. The laminar (with hub) solution however, accurately predicts the turbine performance over that of the k-ε turbulence model. This is ascribed to the low level of turbulence in the simulation space. Should a diffuser be present in the flow area, adverse turbulence effects are expected and hence the k-ε turbulence model is chosen.

One should also note that all turbulence models follow the 1D-theory trend accurately up to $a = 0.4$ and then continue to approximate the modified empirical relation. The error

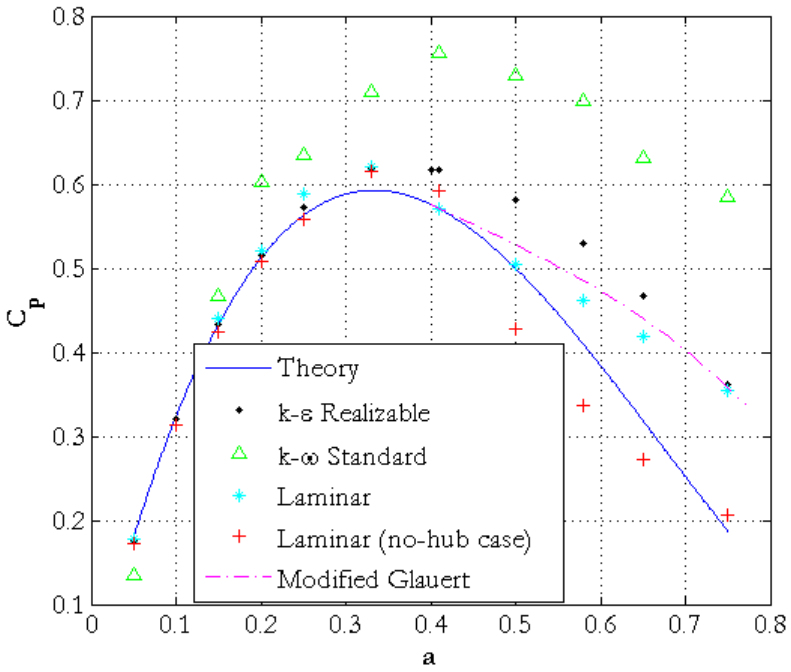

Figure 4.5: C_p versus a graphs showing comparison between rotor theory and various turbulence models.

however increases after $a = 0.4$. As noted in [68], variances in the data are considerable. Thus for $a > 0.4$ turbulence model prediction behaviour is deemed acceptable.

The model turbine rotor to be used in towing tank experiments has a $C_p = 0.43$ at the design point that corresponds to an induction factor of 0.15 according to the ideal turbine theory or 1D-theory (see figure 4.5). The turbulence model at this point has a prediction error of 0.24 % and it may be concluded that the CFD rotor model will accurately simulate the physical rotor at the design point. At the Betz limit of $C_p = 0.593$ corresponding to a induction factor of 0.333, the model predicted $C_p = 0.619$ - over-prediction of 4.4 %.

4.5 Conclusion

It can be seen from the results that the use of a 2D-axisymmetric CFD simulation accurately predicts the performance of a turbine rotor. In addition a grid with a cell size of 42 464 cells seem to be the best compromise between accuracy and computational time. The use of a simple pressure jump formulation to represent the rotor has been presented and validated. The use of the k-ε realizable turbulence model as a closure form to the governing equations underlying CFD has also been validated for use in further CFD studies in this research.

Chapter 5

Optimisation

5.1 Background Theory

5.1.1 What is Optimisation?

Optimisation can be defined as choosing the best solution to a problem from a set of possible solutions. In order to find the optimum, a range of decisions needs to be made to weigh different variables against each other and to eventually decide upon the optimal solution.

Optimisation using gradient methods is best described at the hand of an example used in Vanderplaats [69]. Imagine a person is blindfolded and standing at the foot of a hill. He does not know what this hill looks like or where the highest point is and thus he has to use an alternate method in finding the summit. The hill represents the optimisation problem and the person the optimiser. Whilst being blindfolded the person now needs to find the top of the hill by some means.

He initially takes a step in say the northern direction and returns to his centre position and the same for the west, south and east directions. Now he has gathered some information regarding the gradient of the hill at his position. In order to find the top of the hill he now moves in the direction that allows the steepest ascent until the slope starts to descend (inflection point) or until he is forced to stop due to some constraint (fence etc.). At the new location he recalculates the gradient at his position and then walks in a new direction that is towards the summit until he meets another fence or inflection point. This process continues until he reaches the summit.

This is essentially gradient-based optimisation that the person uses to locate the summit (optimum). To explain this at the hand of mathematics, an example of the "hill" can be represented as:

$$F(X) = e^{-x_1^2 - x_2^2} + \frac{1}{2} e^{-(x_1-2)^2 - x_2^2} \tag{5.1}$$

$$X = \left\{ \begin{array}{c} x_1 \\ x_2 \end{array} \right\} \tag{5.2}$$

Where x_1 and x_2 are two variables an X is the vector containing the variables. Using the hill example, the variables can be defined as the longitude and latitude. $F(X)$ is the objective function (altitude) which we want to maximise and therefore need to find a mix of our variables that will give us the highest point. To see the design space, refer to figure 5.1.

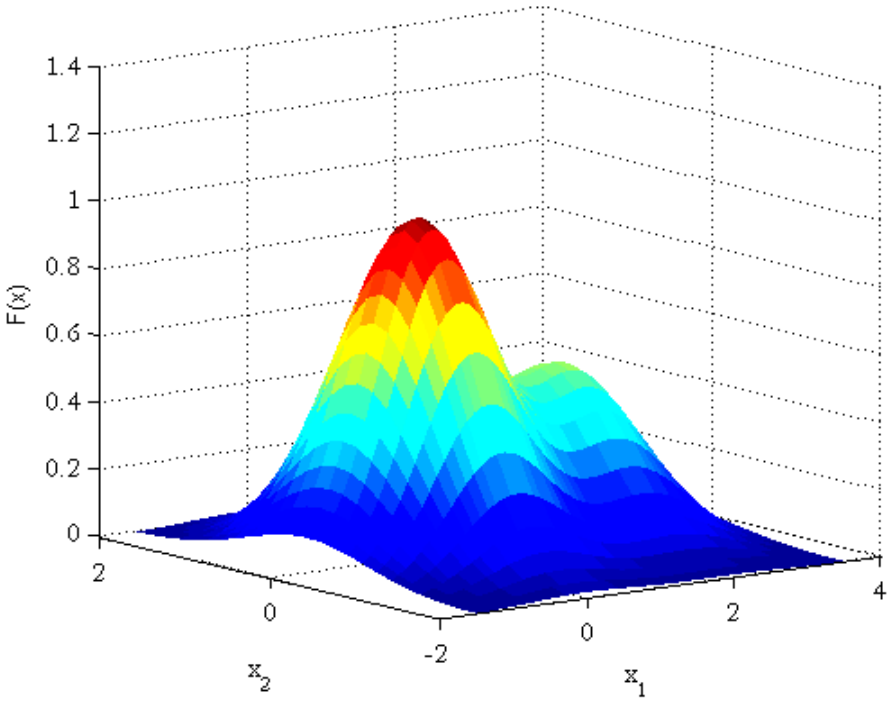

Figure 5.1: Mathematical hill.

From the above figure it may be deduced that the highest point occurs where $x_1 = 0$ and $x_2 = 0$, yielding a height of $F(X) = 1$. If the design space was not visible, using a gradient-based solution will bring you to the summit. In this example there are two peaks; one being lower than the other. The lower peak, or local optimum, can be mistaken for the global optimum if you are blindfolded. More so in a highly non-linear problem with 20 variables (as is typical in engineering), finding the global optimum is not easily achievable from a single starting point.

5.1.2 Optimisation Using Gradient Methods

Gradient methods use the gradient and previous step information to update the search vector and step size. They are based on the direct estimation of the optimum from changes in the gradient. Various methods exist and will briefly be discussed below.

Sequential Quadratic Programming (SQP)

This method is generally regarded as being robust and one of the most popular methods used in solving constrained non-linear continuous problems. Since most engineering optimisation problems are inherently non-linear, it is possible to find the optimum by quadratic approximation of a sub-problem around the current design point. At the current design point, the gradient information is obtained typically using finite differencing. The objective function is approximated by a quadratic Taylor series around the current design point [70]. The constraints are approximated using a linear Taylor series. This updated optimisation problem is then solved by minimising the objective function.

A new design point is then defined and evaluated where this minimum is found and the procedure above is repeated iteratively until no further improvement to the objective function can be made - hence the term sequential programming. The standard formulation of an optimisation problem is:

$$
\begin{aligned}
\text{Minimise:} \quad & F(x) && \\
\text{Subject to:} \quad & g_j(x) \leq 0 && j = 1, m \\
& h_k(x) = 0 && k = 1, l \\
& x_i^l \leq x_i \leq x_i^u && i = 1, n \\
\text{where} \quad & x = x_1,\, x_2 \ldots,\, x_n &&
\end{aligned}
$$

$F(x)$ is the objective function subjected to some inequality and equality constraints. Upper and lower limits are imposed on design variables. The design variables are represented by x.

Seeing that the design problems associated in engineering often involve computationally expensive optimisation problems as they rely on computationally expensive numerical simulation (CFD, FEM etc.), gradient-based optimisation is considered an expensive method [64]. This statement is dependent on the amount of variables being optimised in the problem. In general an optimisation problem involving 20 or more variables makes using gradient-based direct methods more computationally economical than when using metamodelling techniques.

The number of points required to solve a response surface second-order metamodel can be calculated as follow:

$$P_{min} = \frac{(n+1)(n+2)}{2} \tag{5.3}$$

The number of variables is represented by n. For this research a minimum number of 15 points would be required based on equation 5.3. In Wise [70] the amount of points eventually used was a multiple of four times the P_{min} value that reduced the effect of numerical noise and provided a good approximation.

In the current study a variable count of four was used. Thus if a gradient-based method was followed involving four variables, between 90 and 150 function evaluations would have been conducted to find a optimum. For this research's metamodelling technique, using a multiple of ± 7 times P_{min} or 110 points were more to the higher end of the amount of points needed but would ensure adequate design space resolution. This method was also implemented in [70].

One of the main advantages than metamodelling has over gradient or derivative based optimisation is the smoothing out of the noisy responses that tend to show up as local minima or maxima and incorrectly predicts the optimal design [61]. Metamodelling furthermore allows the re-use and easy updating of the design problem without demanding any recalculation and provides greater insight into the global understanding of the design space [61, 64]. The choice was therefore made to use a metamodelling technique.

5.1.3 Metamodelling Techniques

The basic operation of a metamodel or approximation technique is that it effectively reduces a complex CFD or FEM optimisation problem to a set of algebraic equations that can be easily analysed and updated. The name metamodel is therefore used as it effectively makes a algebraic model (mathematical formulation) of the analysed model (CFD, FEM etc.). If the design space is approximated by the metamodel, amendments thereto and related analyses thereof can be conducted quickly and efficiently.

To explain metamodelling mathematically, if the design variables to the actual engineering analyses are supplied in vector x, and the outputs or responses from the analyses is supplied by vector y, the engineering code evaluates:

$$y = f(x) \tag{5.4}$$

The actual engineering analyses (CFD, FEM, etc.) is $f(x)$. The metamodel is then

defined as:

$$\hat{y} = g(x) \tag{5.5}$$

so that,

$$y = \hat{y} + \varepsilon \tag{5.6}$$

The approximated engineering analyses is $g(x)$, and ε includes both the approximation and random errors.

Response Surface Methodology

Response Surface Approximation (RS) is a method that approximates the optimisation problem by fitting low-order polynomials over the design space. This assumes an underlying trend in the form of a polynomial and also assumes a single optimum (global) for the second-order case.

As with the other metamodelling techniques, if the metamodel is fitted accurately, a response from the design space can be obtained via the metamodel without incurring any further function evaluations. One disadvantage of RSs is the drop in accuracy experienced when approximating highly non-linear functions. Increasing the polynomial order is possible but might be too difficult in acquiring sufficient sample data from function evaluations to estimate all of the coefficients in the response surface equation. A second-order polynomial model can be expressed as:

$$\hat{y} = \beta_0 + \sum_{i=1}^{m} \beta_i x_i + \sum_{i=1}^{m} \sum_{j=1}^{m} \beta_{ij} x_i x_j \tag{5.7}$$

Here the set of coefficients $(\beta_0, \beta_i ...)$ can be determined by least squares. This is a well established approximation method and implementation thereof is easy. With the increase in non-linearity of functions common in complex engineering problems, SVR metamodelling has grown in popularity due to its ability to handle highly non-linear functions [70, 65].

Support Vector Regression

SVR is a modelling technique that, unlike RS, does not assume an underlying model and does not follow the "black box" approach as used for radial basis functions (RBF) and Kriging approximations. As described in RS methods, the aim of the approximation is to model the design space accurately by fitting it over some function evaluation responses (training data) acquired from, for instance, CFD or FEM analyses conducted using some DOE implementation.

For SVR, the aim is to fit this training data with at most a deviation of magnitude ε. Errors are therefore considered to be zero if they are less than ε. The SVR model can be expressed as:

$$\hat{y} = \sum_{i=1}^{p} (a_i - a_i^\star) K(x_i, x) + b \tag{5.8}$$

The values of $(a_i - a_i^\star)$ and b are obtained during the fitment process; $K(x_i, x)$ is the kernel function where x_i are various training points from the DOE and x is the point in the design space where the SVR model is to be evaluated.

The loss function ε can be of a linear (as used in the current study) or quadratic form. From [70] the linear case was used in a non-linear design space and acceptable results were generated. The formulation for the linear case is expressed as:

$$L(x) = \left\{ \begin{array}{c} 0, \, if \;\; \mid y(x) - \hat{y}(x) \mid \leq \varepsilon \\ \mid y(x) - \hat{y}(x) \mid, \, else \end{array} \right\} \tag{5.9}$$

In addition to ε, a regularisation parameter C needs to be selected. The parameter C determines the trade-off between the complexity and degree to which deviations greater than ε are tolerated in the optimisation formulation. When C is excessively large, the tolerance is small and the SVR formulation highly complex, and vice versa [64].

In the kernel function another parameter needs to be chosen correctly, namely σ the radius parameter in the Gaussian RBF kernel function. Although various other types of kernel functions exist, this formulation was chosen as it delivers higher accuracy over the linear-type kernel [70]. Some types are presented in table 5.1.

Table 5.1: Kernel Types

Linear	$K(x_i, x) = \langle x_i \cdot x \rangle$
Polynomial	$K(x_i, x) = \langle x_i \cdot x \rangle^d$
Gaussian	$K(x_i, x) = \frac{\sqrt{\sigma^2 + \|x - x_{oi}\|^2}}{\sigma}$

From the discussion presented above it can be seen that when using SVR three parameters, ε, C and σ need to be appropriately selected so that the model fits the training data and delivers accurate responses.

5.1.4 Design of Experiments

The DOE consists of various points that are analysed explicitly by using some model that incorporates the design variables such as CFD or FEM. The DOE therefore effectively

provides various training points (responses) acquired from, for instance, the CFD model that evaluated the design variables at various points in accordance with the optimisation problem formulation.

The metamodel's approximation accuracy is influenced by the distribution of training points and the distribution scheme used; as the metamodel is fitted to these training points [61]. If the amount of points are too few, it leads to low resolution and the design space responses in certain areas can be incorrectly modelled or omitted leading to a metamodel that produces incorrect responses and that brings the approximation's fidelity into question.

Various DOE designs exist from D-optimal to Latin hyper cube (LHC) designs. For metamodels assuming an underlying form such as in the case of RS optimisation, a D-optimal design is preferred. Such a design distributes the bulk of the training points to be analysed around the perimeter of the design space and at the centre of the design space. This method is used as the parts in-between points of the design space is assumed from the RS polynomial form and thus yield a RS model that is insensitive to noise [61]. For metamodelling techniques that do not assume an underlying form such as SVR, a space-filling DOE such as LHC is preferred as more information across the entire design space is required for accurate fitment of the metamodel. This method aims to distribute the training points across the field evenly and efficiently. The aim here is to gather as much information of the design space with as few as possible training points.

To ensure that a true optimum is reached, the following method is applied. After fitting the metamodel to the training points, the objective function is minimised and an optimum point is reached. This optimum is then analysed using CFD, and the CFD results are compared to the SVR response. If a difference exists that violates some threshold in error between the approximation and CFD, the optimum point of the CFD together with its design variable values are added to the DOE and the SVR model is again fitted to the new DOE and minimised. This process continues until convergence is achieved.

5.2 The Optimisation Problem

The optimisation problem as it pertains to the research is to maximise the C_p value of the turbine by finding the optimal geometric diffuser shape that will maximise the rotor axial velocity u, and pressure drop Δp over the rotor.

For the present purposes, the diffuser is to be represented by a single curved plate that can be described by a B-spline. Using the spline will allow changes of the shape of the diffuser with a minimum number of variables. After various trials a compromise

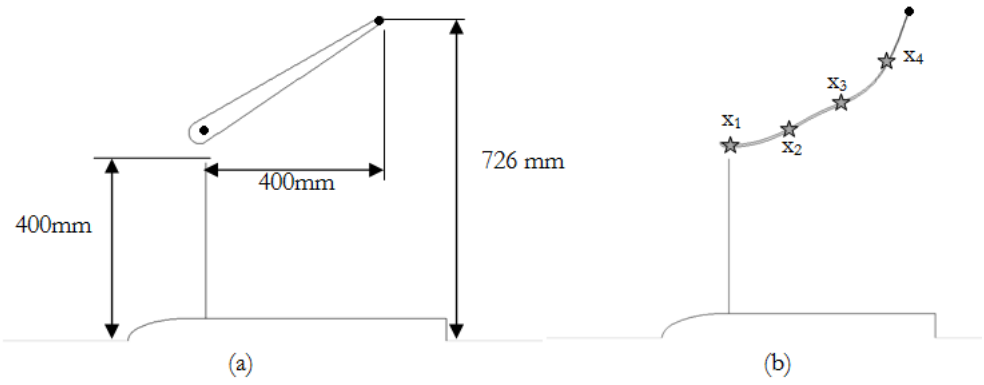

Figure 5.2: (a)Diffuser dimensions as defined in Grobbelaar, (b) curved plate diffuser with variable points.

between complexity and DOE size was reached by choosing four variables to describe the diffuser geometric shape. A constraint to the problem as described earlier is that the optimised diffuser should be of the same geometric envelope than the diffuser used by Grobbelaar [11].

When parameterising the diffuser, it should be done to allow automation of the mesh generation. Being able to do this, a parallelisation implementation of the DOE is possible.

5.2.1 Diffuser Representation and Parametrisation for Variables

The dimensional constraint can be seen in figure 5.2. In addition the geometric variables describing the B-Spline can be seen in figure 5.2(b).

Figure 5.2(b) indicates that the black spot to the right of the variable x_4 is fixed at a vertical length of 0.726 m from the centre of the turbine and 0.4 m in the horizontal axis behind the rotor plane. The variables in (b) are equally spaced at intervals of 100 mm in the horizontal direction, starting at the rotor plane. For the optimisation they are only allowed to vary in the vertical direction; their horizontal position is fixed. This is done to minimise the amount of variables needed. Madsen [61] uses two variables that yielded acceptable results with regard to B-spline curves. Additionally a monotonicity constraint (limit constraints) is implemented, meaning that the height of x_1 should be less than x_2, $x_2 < x_3$ and $x_3 < x_4$ to ensure a negative gradient along the B-spline curvature. To include some buffer dimension to the limit constraints, variables are not allowed to be within 0.02 m from each (to ensure the monotonicity of the B-spline) other and the lowest minimum rotor tip clearance that should exist is 0.015 m between the rotor tip and diffuser throat (hence 0.415 m limit for x_1). From pre-studies conducted it was found that if one or more variables are located on the same horizontal plane the B-spline formulation allows for negative as well as positive gradients in the curve, hence the 0.02 m value. All

variables now represent a vertical height.

5.2.2 Problem Definition and Constraints

The optimisation problem can therefore be defined as:

$$\text{Maximise:} \qquad Cp\,(x_1,\, x_2,\, x_3,\, x_4)$$

$$\begin{aligned} \text{Subject to:} \qquad 0.415 \leq x_1 &\leq x_2 - 0.02 \\ x_2 &\leq x_3 - 0.02 \\ x_3 &\leq x_4 - 0.02 \\ x_4 &\leq 0.726 - 0.02 \end{aligned}$$

5.3 The Function Evaluation

A grid has already been created in Chapter 4 that validates the rotor model. One therefore needs to add the diffuser geometry to the grid in such a way so as to allow parallelisation of the function evaluation; by manipulating the grid generation via some pre-processor (in our case Gambit) journal files.

It was important to use a boundary layer around the generated diffuser geometry. The boundary layer grid was therefore generated to include near wall effects with the use of wall functions. To allow for the law of mean velocity to be applied, a value range for $20 < y^* < 300$ is necessary and at least a minimum $y^* > 11.25$ is needed to employ the log-law [66]. These rules applied to the CFD solver used in this research.

Knowing the range of y^* a boundary layer needed to be constructed so that the first cell height from the wall would equal a certain distance. The mean velocity, however, differed along the diffuser, from the inside of the diffuser to the outside of the diffuser. Thus to solve this, the wall shear stress first needed to be calculated from a CFD analyses involving a diffuser-augmented turbine from which general but similar values to that encountered in the function evaluation could be deduced.

After analysing the diffuser-augmented turbine, the wall shear stresses were obtained and the boundary layer first cell height found to be in a range of 0.31 mm$< y_h <$ 1.54 mm with a minimum boundary layer height of 11.5 mm. A first cell height of 0.9 mm was chosen as the best compromise between grid size and boundary resolution.

The next step now is to construct the boundary layer in such away to minimise the cell count around the diffuser, but to still allow good grid quality in terms of aspect ratio,

skewness and squish. Thus a mesh seed of 200 nodes was chosen on the inside and outside of the diffuser walls; a first row height of 0.9 mm, and nine rows thick layer. From the first row a growth factor of 1.09 in row thickness was selected with a transition of 4:2 to the interior mesh. To illustrate this, figure 5.3 shows the boundary layer of the diffuser.

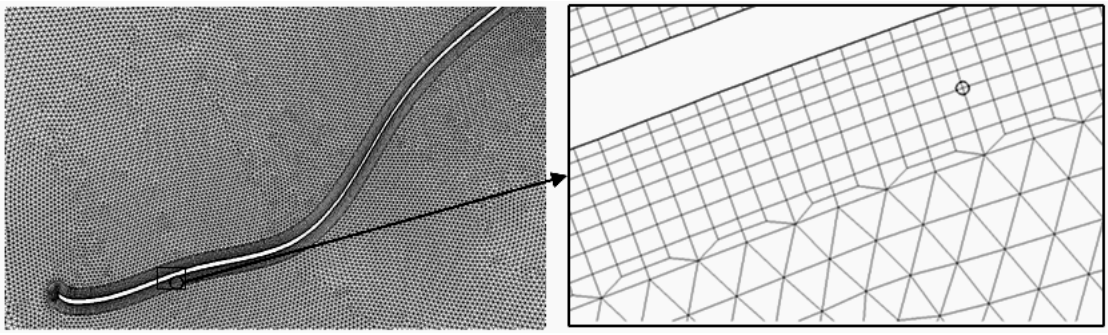

Figure 5.3: Boundary layer mesh for diffuser.

The transition was chosen so as to minimise the number of cells being generated. The parametrised grid is now increased in number of cells from 42 464 without the diffuser to 168 682 cells with the diffuser. This increase is expensive, but following the procedure to limit the cell cost, it was found as the best compromise between accuracy and computational cost.

The final mesh possesses exactly the same boundary settings as the one used in Chapter 4, except for the inclusion of the diffuser as a "wall type" boundary. With the addition of the diffuser, much greater turbulence were encountered and it was found that the convergence differed greatly for different meshes, as the diffuser was allowed to change in the optimisation. After various trails, an iteration count of 10 000 was found to provide sufficient convergence of all residuals. Figure 5.4 shows the mesh in greater detail arround the diffuser.

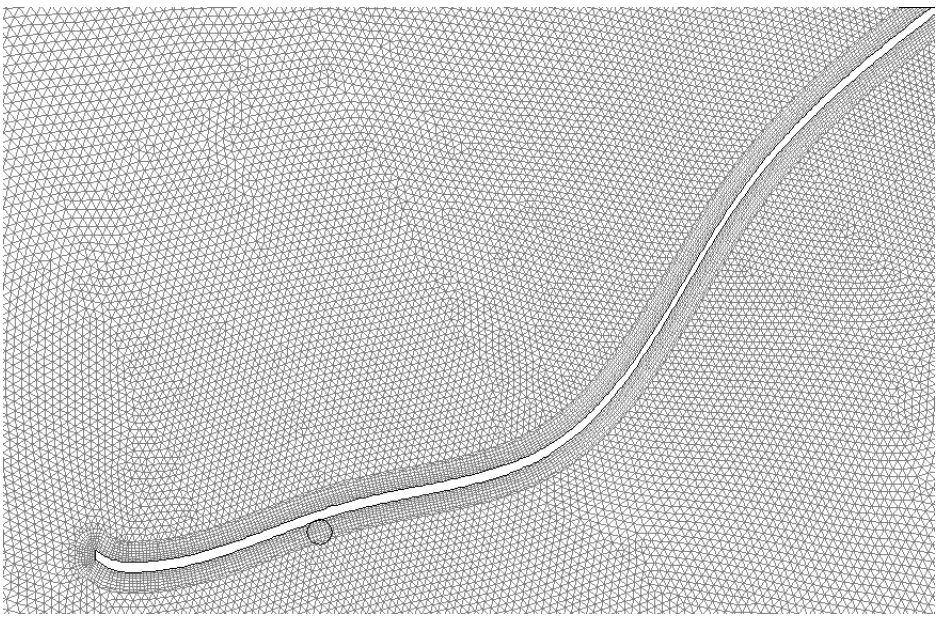

Figure 5.4: 2D-axisymmetric mesh of diffuser-augmented turbine.

The function evaluation is however only partially completed as the mesh has been generated but the solver settings not yet defined. For our optimisation an automated approach to solve the mesh for certain flow conditions needed to be conducted. The use of Fluent's journal text command script allows for this automation. The researcher therefor arranged the function evaluation to be generated and analysed by only changing four inputs representing the design variables in the Gambit journal file and then simulating via the Fluent journal file. For simulation details and convergence plots, please refer to Appendix B.

5.4 Methodology and Implementation

5.4.1 Design of Experiments Implementation

The DOE is used to gather responses from the optimisation problem and to provide the training points over which the metamodel can be fitted. In addition to generating the training points, some test points that are unique to the training points are produced against which the metamodels fit and prediction accuracy can be checked.

The DOE consists of analysing various design variable configurations by generating individual meshes; simulating them in the CFD solver and extracting the relevant data to compute each unique configuration's turbine performance in terms of the turbine power coefficient C_p and drag coefficient of the diffuser C_d. For the purposes of this study, in order to have enough responses for the design space to be modelled by the metamodel,

110 training points needed to be generated. Some test points needed to be generated and 25 points were considered appropriate.

Each CFD simulation took approximately 13.5 hours to complete on a single dual core 2.1 GHz Intel processor work station. Thus for the current study involving 135 analyses (110 + 25 function analyses), a time of 75.9 days would be necessary to complete all the analyses once. The need to expand the DOE implementation in a parallel environment is therefore obvious

A high speed computing cluster (HPC) exists at US and it was decided to implement a parallelisation regime on this device. It consists of 168 cores with each core having 16 GB memory and a process capacity of 2.83 Ghz. It therefore has a total system capability of 336 GB memory; data storage of 12.1 TB, and theoretical performance of two Tflop.

To accomplish the parallelisation of the DOE an implementation methodology needed to be established to analyse the DOE from point one through to point 110. This is best illustrated at the hand of the flow diagram presented in figure 5.5. Keep in mind that this is an elaboration on step number three in figure 3.1.

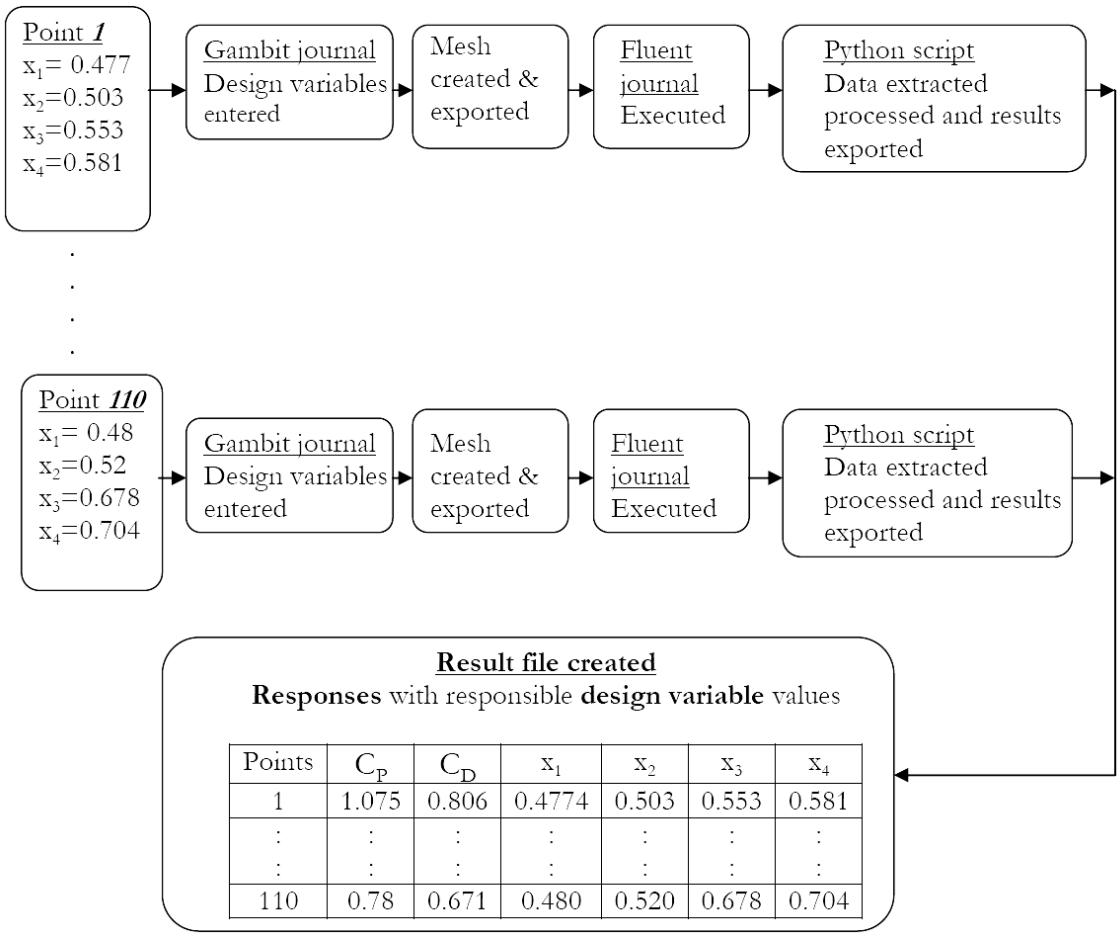

Figure 5.5: DOE implementation strategy.

To implement the parallelisation a message-passing interface was used and an automation script that oversaw, initiated, terminated and generated all the steps described in figure 5.5. The automation script (management program) was generated using VisualScript in conjunction with VisualDOC. By adding all the elements to VisualScript (Gambit, Fluent and Python post-processing), a Python script was generated that controlled the flow of data from starting Gambit; generating the mesh via the journal; exporting the mesh; starting Fluent; simulating via the journal, and finally extracting the data with the use of Python and exporting the results.

After finalising the automation of a single function analyses, a master/worker implementation was used to implement the parallelisation. OpenMPI was used as the message-passing interface and after experimenting with various simulation setups, a simulation setup for the parallel job was found to execute the DOE fastest when running four jobs in parallel with each using eight cores to process a single job. This reduced the simulation time of the DOE from 75.9 days to approximately 4 days.

Finally the DOE was successfully executed and 110 training points and 25 test points generated.

5.4.2 Creation of the Support Vector Regression Model

Once the training and test points were created the SVR model could be fitted to the data. As seen in the previous section, two responses are given as outputs, namely the C_p and C_d values. This allowed the calculation of the the power augmentation, with its related cost in terms of added drag to the diffuser-augmented turbine.

For the SVR creation, the Surrogates Toolbox [65] was used and implemented in Matlab. The built-in Matlab optimiser was used to maximise C_p. An important factor and open issue in the implementation of SVR concerns the quality of fitment that can be achieved by varying the regularisation parameter C and the radius parameter σ of the kernel function. The insensitivity parameter ϵ was found to also play a role but to a lesser degree. For the fitment process a value of $\varepsilon = 0.00001$ was found to be adequate.

The values for C and σ were determined by analysing the amount of error for each different configuration. For the first evaluation of the model the 110 training points were used to fit the model. The researcher then progressed to vary the C and σ values; where at each C and σ an error analyses method called "cross-validation" was performed.

Although test points were available to analyse the metamodel to increase the fidelity of the approximation, various other validation techniques were used. The cross-validation method excludes one training point; fits the model to the remaining points, and then

determines the RMS error between the excluded point and the SVR model approximation. Figure 5.6 shows a contour plot of the cross-validation analyses. Note the higher resolution area between $C = 100$ and $\sigma = 0.5$.

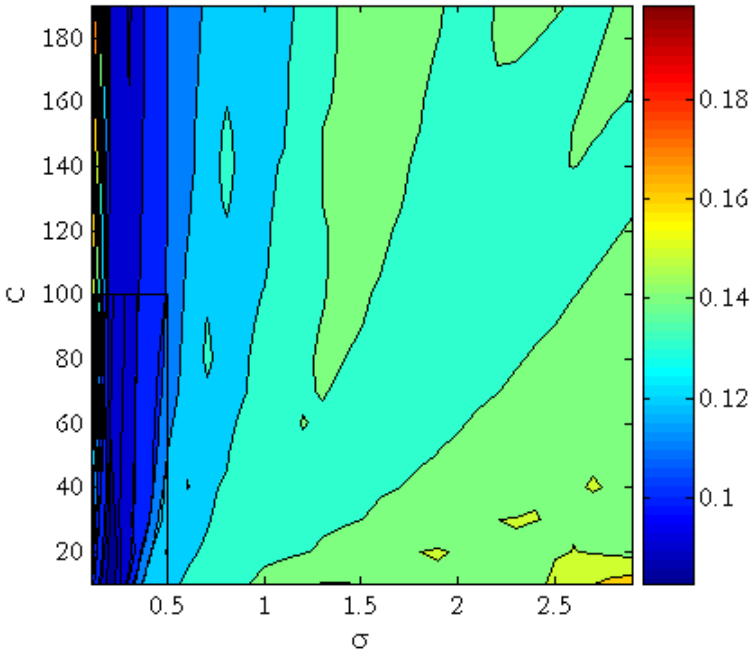

Figure 5.6: Cross-validation RMS error for C and σ values.

From the above figure it can be seen that the error is relatively the same for $C = 0$ - 100 and that the chosen σ will be less than 0.5. In order to also analyse the fitted model further regarding errors, the absolute average error (AAE), standard error (SE) and coefficient of determination (R^2) were also calculated. In addition the fitted model was analysed against the 25 test points generated and the same errors analysed. The result of the SE is shown below.

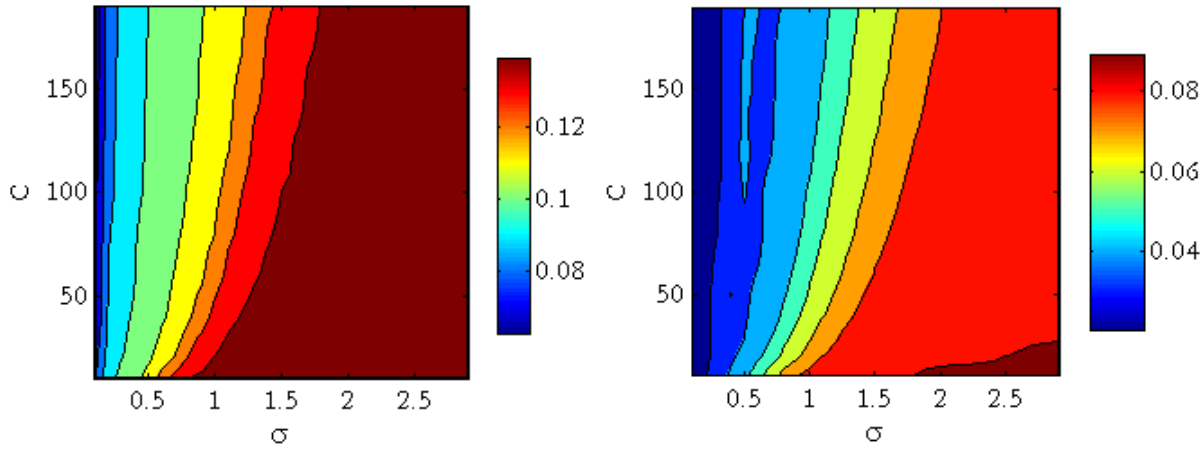

Figure 5.7: Standard error (SE) for 110 point fitment (left) and the fitted model against test points (right).

From these figures it can be seen that the value for C could be chosen between 0 and 100, after 100 the accuracy of the model tended to drop. A value of $C = 40$ was selected. After this the AAE was investigated for the value of C and allowed σ to vary between 0 and 0.5. For this analyses the SVR model was first fitted against the training data with varying σ. At each value for σ, the model was checked to see how accurately it predicted the test points and the AAE was calculated. The results are presented in figure 5.8.

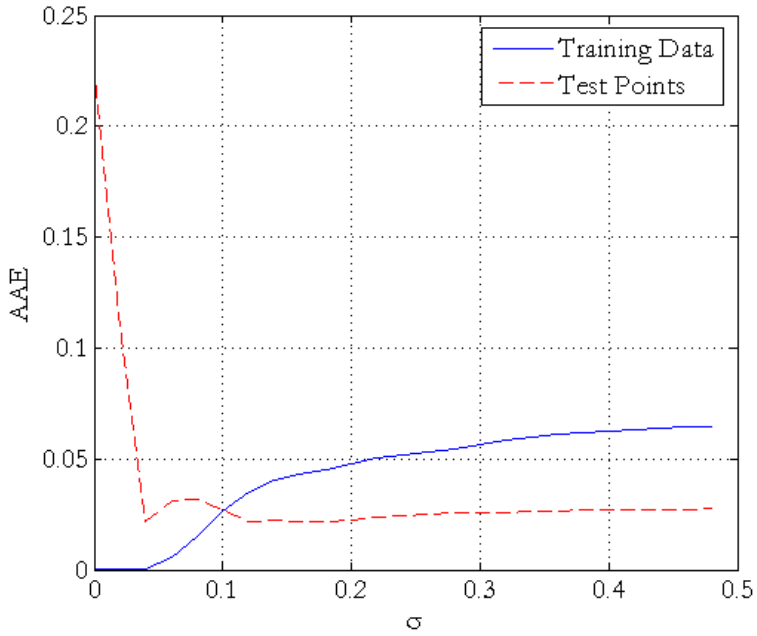

Figure 5.8: Absolute average error for $C = 40$ and $0 < \sigma < 0.5$.

From this figure it is seen that a σ value that allows both trends to have a minimum

AAE is to be selected. Two values are eligible candidates, namely 0.12 and 0.047. When $\sigma = 0.047$ was chosen, it resulted in better metamodel accuracy related to additional cross-validation tests and test points. Hence $\sigma = 0.047$ was selected.

To approximate the C_p responses in the optimisation for the SVR model, $\sigma = 0.047$, $C = 40$ and $\varepsilon = 0.00001$ was used. A similar process was followed to fit the C_d responses and the model parameters were found to be $\sigma = 0.04$, $C = 60$ and $\epsilon = 0.00001$.

In order to insure a global optimum for C_p was reached for the SVR and RS model, the optimisation was carried out by using each training point as a starting point. After the global optimum was reached the associated optimum design variables were used to construct a CFD analyses and the global optimum C_p was compared to the computed CFD C_p value.

If a difference in values existed, the C_p resulting from the CFD analyses was then entered into the training points, and the optimisation procedure repeated and the next global optimum C_p from the SVR model checked against the CFD C_p. This process was repeated until the SVR and CFD C_p values converged to within 0.5% of each other. For this study this occurred after 12 iterations.

It should be noted that during optimisation by starting at the 122 points (110 +12 additional points), the optimiser converged at eight different optimums. This showed the existence of local optimums and confirmed a multi modal design space.

The final results for the optimum diffuser shape with corresponding predicted C_p, C_d and design variables (measured as radius lengths) are presented in Table 5.2.

Table 5.2: Details of optimum diffuser as determined by SVR.

C_p	C_d	x_1 (m)	x_2 (m)	x_3 (m)	x_4 (m)
1.672	1.728	0.426	0.4463	0.4984	0.5480

5.4.3 Optimisation of C_p versus C_d

Once an accurate metamodel for the system existed the problem of how C_d is influenced by a higher C_p could be investigated. In this regard it should be noted that optimising merely for the highest possible C_p might be too straightforward and one would preferably combine the C_p model with the C_d model as a non-linear constraint. Using the two metamodels, some studies were done to gain more knowledge on the behaviour of the diffuser-augmented turbine. Being able to do this is a distinct advantage of metamodelling techniques.

It was firstly decided to optimise the diffuser system for the maximum power coefficient whilst being constrained to a maximum C_d value of 0.7. Repeating the optimisation for a C_d value of 0.8 and so on up to a value of 1.8 and finally an unconstrained C_d Figure 5.9 below shows the results.

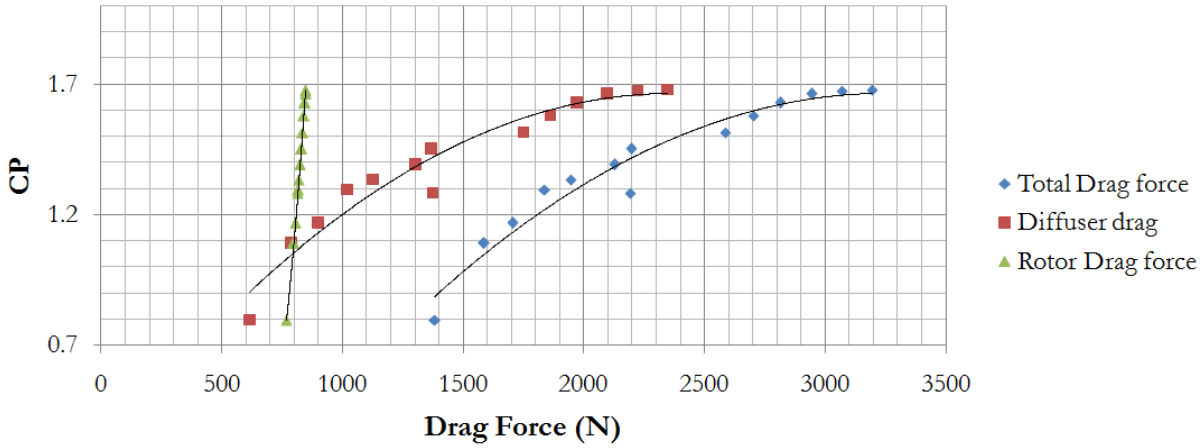

Figure 5.9: Power coefficient versus drag force graph for the total system, diffuser only and rotor only.

It is important to note that C_p refers to the total system power coefficient. For instance, at a total system C_p value of 1.2 the rotor drag force, and diffuser drag force were calculated according to 1D-theory. In figure 5.9 the drag contribution of the rotor is less than the contribution from the diffuser. Over the entire C_p range the rotor drag force contribution only varies between 766 N to 846 N whereas the diffuser drag contribution varies between 615 N and 2347 N.

The pressing question that arises from this stage of the research is whether using multiple rotors to achieve a higher system power output is a better option when considering the increase in drag of a diffuser system to achieve the same level of power output. Figure 5.10 below shows the power versus drag force of a multiple rotor system (MRS) and diffuser-augmented turbine (DAT). Multiple rotor systems refer to using multiple single bare rotors (turbine farm).

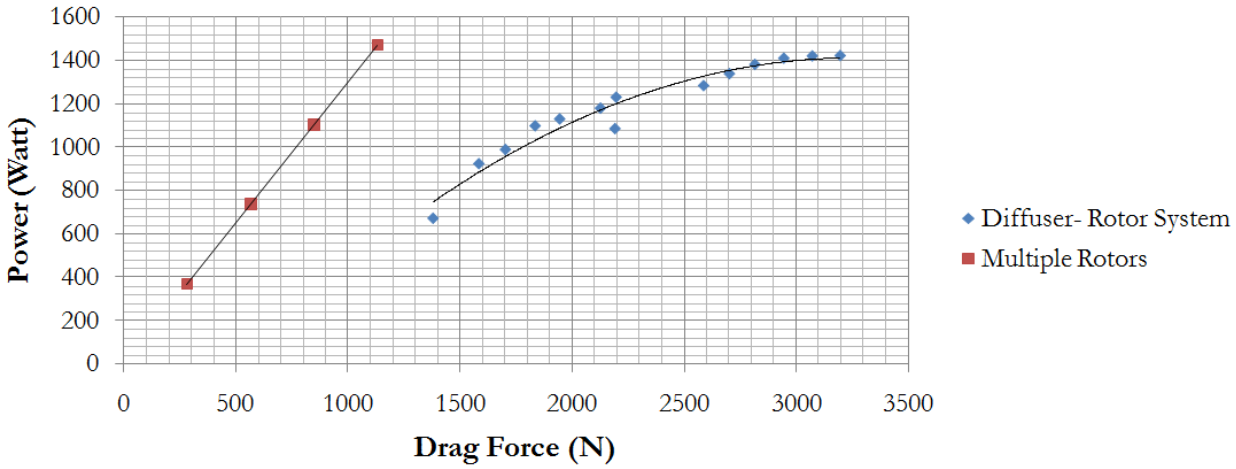

Figure 5.10: Power versus drag force graph for multiple rotor system and diffuser-augmented turbine (diffuser rotor).

From figure 5.10 it is clear that when considering only the drag, the MRS is preferred over DAT. The optimisation problem however now becomes an economic one. The cost of higher drag to structural integrity, increased mooring and materials cost, might for instance be very small over the additional cost of an extra rotor with a generator and gearbox. Attempting to therefore address the question whether MRS is preferred over DAT considering economical profitability and complexity seems difficult to answer and is beyond the scope of this project.

Literature shows that the limit to which C_p can increase seems to still be proved in experimentally [12, 9, 53]. Various experiments, mainly focused on wind turbines, have shown underestimated results on C_p increase for diffuser-augmented turbines. It is thus proposed that the optimisation should aim to increase the C_p as much as possible without being constrained by C_d.

5.4.4 Creation of the Response Surface Model and Comparison to Support Vector Regression Model

For this study it was deemed necessary to show results as compared to the SVR model in terms of optimum achieved, convergence and accuracy. An identical fitting strategy was used to analyse the RS model. Although its implementation is straightforward, the quality of the fit still needed to be established.

After fitment of the 110 training points the RS model was optimised and the same convergence strategy followed as in the SVR model. After eight iterations of the strategy the convergence was achieved. It was found that the RS model fitment quality was poor in

comparison with the SVR model. This is due to the use of training points obtained from using a space-filling LHC and not a D-optimal approach that is better suited to RS techniques. RS being low-order polynomial therefore requires only point density in the centre of the design space and the periphery as it assumes the low-order polynomial between the open spaces. Space-filling designs like LHC then allocates less points in the centre and periphery. The errors investigated with their respective abbreviations are displayed in the table below.

Table 5.3: Errors investigated between the SVR and RS model.

R^2	Coefficient of determination
R^2a	Adjusted R-square
RMSE	Root mean square error
MinE	Minimum error
MaxE	Maximum error
MAE	Maximum absolute error
RYYhat	Correlation coefficient between DOE points and DOE points predicted by the model
SE	Standard error

To illustrate the difference in accuracy, the converged metamodels of RS and SVR were analysed for errors as it pertains to the training data alone. The results follow in the Table 5.4.

Table 5.4: Comparison of errors between RS and SVR models pertaining to the training data.

	R^2	R^2a	**SE**
SVR	0.9982	0.9982	0.0128
RS	0.8945	0.8804	0.104

The metamodels are subsequently given the task to predict the 25 test points. The errors are then calculated between the actual test point data and the model approximation of the point data. The results are as follow:

Table 5.5: Comparison of errors between RS and SVR models as compared to test points.

	R^2	R^2a	**RMSE**	**MinE**	**MaxE**	**MAE**	**RYYhat**
SVR	0.737	0.737	0.0712	-0.26	0.1921	0.2602	0.8750
RS	0.52	0.184	0.093	-0.3603	0.244	0.3603	0.851

Finally, a comparison between the optimums reached by the different models is conducted and is presented below.

Table 5.6: Comparison in optimums reached between the RS and SVR model.

	C_p	x_1 (m)	x_2 (m)	x_3 (m)	x_4 (m)	**Iterations to convergence**
SVR	1.672	0.426	0.4463	0.498	0.548	12
RS	1.616	0.415	0.435	0.455	0.475	8

From the aforementioned discussion it may be deduced that a difference of 3.4 % exists between the optimum C_p values of the RS and SVR model. Also note that the SVR model's optimum is reached inside the design constraints imposed. The RS model's optimum is reached whilst all the constraints are active.

The optimised shape was found to be relatively insensitive to shape changes with respect to C_p values. For changes of between 20 and 28 mm in the vertical location of the design variables ($x_1 ... x_4$) that define the diffuser shape by means of a B-spline, the C_p varied between 1.571 and 1.672. This is illustrated in figure 5.11.

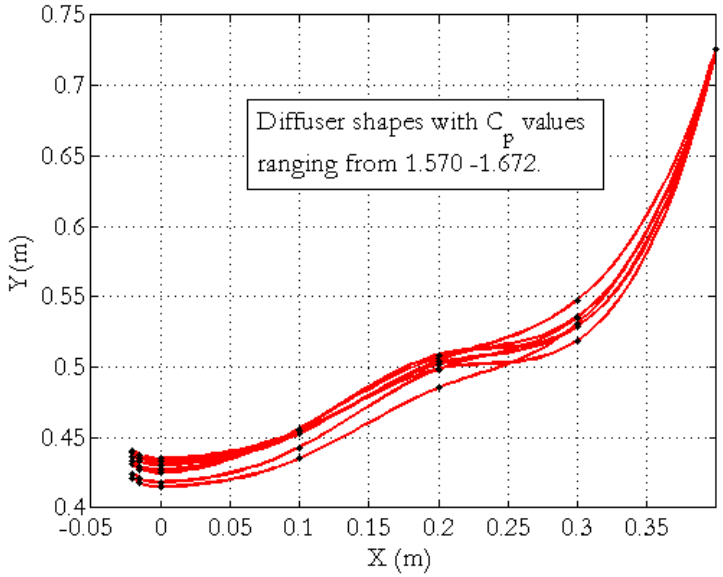

Figure 5.11: Change in diffuser performance with change in diffuser shape.

5.4.5 Optimum Design

The need existed to check the final optimum design as proposed by the SVR model. For this a 2D-axisymmetric CFD solution with a higher mesh resolution was selected in order to obtain a more accurate result. The mesh consisted of 406 604 cells and had a maximum

aspect ratio of 4.83; maximum cell skewness of 0.52, and maximum squish of 0.32. The mesh was thus considered to have acceptable quality as all values were within excellent to good ranges. Convergence was achieved at 18 000 iterations, but to ensure that it was not temporary, the simulation was allowed to run to a iteration count of 30 000.

Pictures showing the diffuser shape and relevant contour plots are presented below. The images are zoomed in for adequate viewing of the area around the diffuser.

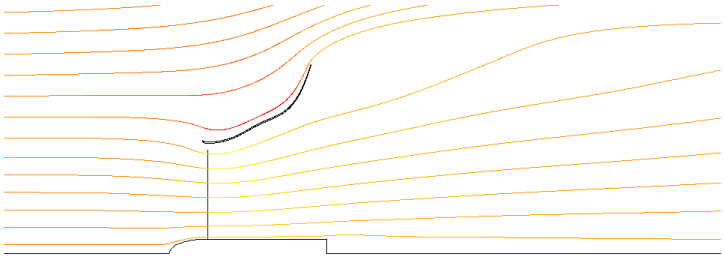

Figure 5.12: Path lines through diffuser.

Figure 5.12 indicates the path lines through the diffuser. It is evident how the lines contract as they approach the rotor plane and then expand again as they leave the plane, exhibiting diffuser behaviour. In figure 5.13 the static pressure can be seen to initially decrease slightly in front of the rotor and is then greatly reduced after the rotor when kinetic energy is extracted and the streamlines expand.

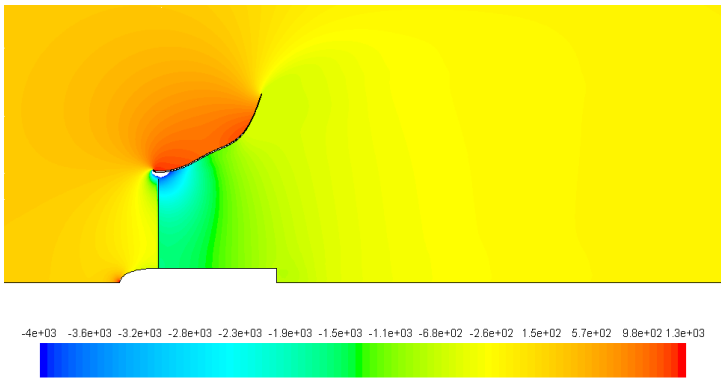

Figure 5.13: Contour plot of static pressure in the diffuser area.

Figure 5.14 shows a contour plot of the axial velocity around the diffuser-augmented turbine.

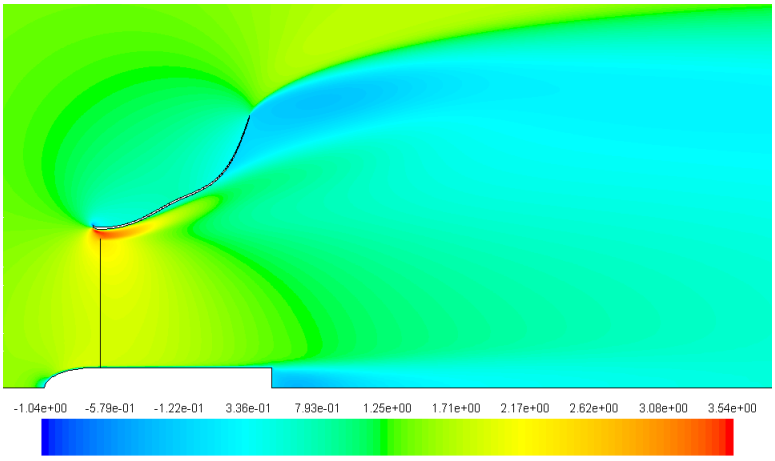

Figure 5.14: Contour plot of axial velocity in the diffuser area.

In figure 5.14 one can note the high velocity water jet passing between the diffuser and the rotor tip. This jet is responsible for retarding the onset of boundary separation in the region and for the re-energisation of the boundary layer [58].

5.5 Conclusion

The various steps undertaken in order to determine the optimum shape of the diffuser have been discussed. First the discontinuous pressure jump rotor model was validated against 1D-theory, this validated the use of the k-ε turbulence model. In addition the details of the 2D-axisymmetric function evaluation was presented. From this section a validated function evaluation existed for use in the optimisation.

In order to understand the optimisation methodology, a short description of related theories was presented. The choice of the SVR metamodelling technique was made based on its comparatively cheap computational cost compared to gradient-based techniques; ability to handle highly non-linear design space approximation, and smoothing of numerical noise.

In addition to the SVR model, a RS model was also constructed and the two models compared to each other using various test points. The results showed that the SVR model outperformed the RS model considerably in terms of error analyses, but showed a gain in optimum C_p value of only 3.4 %. Similar to Madsen [61] it was found that the diffuser performance is relatively insensitive to small shape changes.

The overall results are encouraging as the SVR indicates a theoretical increase in C_p over its bare turbine counterpart by a factor of 3.77 or equal to a $C_p = 1.672$. This relates

to an increase in power from 383 W to 1448 W. However increase in power due to the diffuser, came at a drag cost of a factor 8.30 increase. For this study it was decided to not minimise the amount of drag incurred and a diffuser based on maximising C_{p} was selected.

A previous study performed in Gaden & Bibeau [62] shows that for a given rotor, if the diffuser area ratio is increased over 1.30 the factor increase essentially remained the same. In the same study for a diffuser area ratio of 3.30, an augmentation factor of 2.62 was achieved. In [62] the arrived at the optimum by changing only the diffuser area; however the diffuser half angle and length was dependant variables and changed as the area changed. In this study for a diffuser area ratio of 3.30 a factor increase of 3.77 is predicted, greatly exceeding the previous studies maximum.

The results also compare favourably to the study of Grobbelaar [11], as the diffusers used in both have the same diffuser area ratio and geometric envelope. In the study of Grobbelaar 710 W is the maximum measured power. This relates to a increase in power over the bare turbine by a factor of 1.85. In this research a predicted maximum power output of 1448 W is predicted through optimisation that translates to a factor increase of 3.77. This is a considerable improvement on the straight wall diffuser of Grobbelaar.

For the diffuser-augmented turbine, the rotor axial velocity has increased from 1.289 m/s (bare turbine) to a velocity of 2.014 m/s; that is equal to a mass flow increase of 1.56. Thus if one regards the theory as proposed in equation 2.34, a maximum factor increase in power of 1.56 is possible. If we however consider the ratio in axial velocity cubed, a better estimate is proposed.

$$\frac{C_{p,d}}{C_{p,b}} = \frac{V^3_{rotor,d}}{V^3_{rotor,bare}} \tag{5.10}$$

Applying equation 5.10 a factor increase in power of 3.81 is predicted. When applying equation 4.4 to the CFD data, an increase in power by a factor of 3.78 is predicted; a difference in value of less than 1 %.

The optimum diffuser has a slight bell-shaped middle section as encountered in the design of a diffuser in [61]. In the beginning of the diffuser the rapid expansion in cross-section of the diffuser occurs and then plateaus slightly to give rise to the bell-shape. This happens as the boundary layer is still stable and able to withstand a higher adverse pressure gradient [61]. As the boundary layer grows unstable the curvature is decreased until separation cannot be postponed, and the shape rises to the flanged-type end part. It seems that the positive effect of a flange at the end of the diffuser is also incorporated in a way similar to the straight wall diffuser of Matsushima *et al.* [12].

Now that the diffuser shape has been optimised, it must be manufactured and tested. The following chapter deals with the design of the support structure and the diffuser.

Chapter 6

Design

6.1 Structural and Diffuser Design

One of the considerations that the researcher had to keep in mind was that the rig needed to be as stiff as possible in order to minimise the amount of deflection experienced by the support structure and diffuser.

The reason for the above statement is that the current test rig as used by Grobbelaar [11] consists of two independent parts, namely the turbine rotor assembly (TRA) and the diffuser with support structure (DSS). They are thus able to deflect in the axial direction independent of each other. This can have adverse effects on test results as the rotor location will not correspond to the location used in the optimisation procedure; making the test results questionable.

To ensure minimal deflection, topology optimisation was used in conjunction with various FEM analyses. Details of the application of these techniques can be found in Appendix C. Using topology optimisation, the placement of support struts to minimise structural deflection was obtained. Forces experienced during testing were calculated from CFD and applied to all FEM analyses. After performing a buckling analyses and checking the structural integrity, no material failure was predicted by the model and showed a maximum combined stress experienced by the steel support structure to be 93 MPa. A maximum combined stress of 14.7 MPa was experienced by the diffuser with its wall having a thickness of 10 mm. The maximum deflection experienced by the support structure was predicted to be 8.3 mm in the streamwise direction.

Consequently the rig was adjusted so that when in testing, the rotor plane was located correctly to the diffuser as simulated in the CFD analyses.

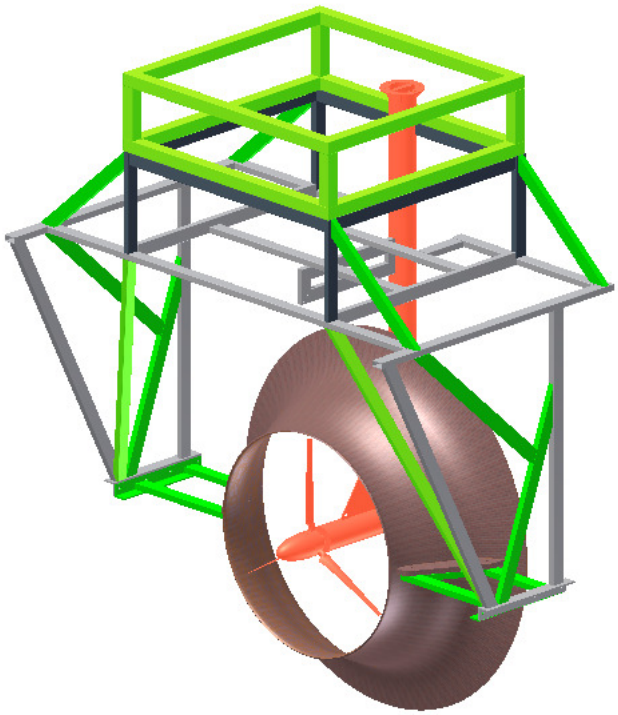

Figure 6.1: New test rig design showing additional strengthening supports (green struts).

Chapter 7

Manufacturing

7.1 Diffuser

For the manufacturing of the diffuser a novel approach was followed. In order to save resources and cost, the diffuser was to be made in two halves that could be joined by means of a flanged interface. A mould therefore needed to be made for the fibreglass hand lay-up, and a material that is stable enough to work on was required. Due to the researchers bursary agreement the material to be used was specified to be fibreglass.

A wood-type material was first investigated to produce the diffuser mould. This was to be done by using CNC machining to have the mould within 1 mm tolerance of the CAD model. The total amount of wood needed to manufacture the diffuser was however estimated to cost R 3 225.00. This estimation was based on the use of Jelutong wood, which is preferred for CNC operators due to its fine fibre structure and minimal chipping quality.

Being too expensive, a high density polyurethane (HDPU) foam (40 kg/m^3) was also investigated as a substitute for using Jelutong. Quotations from various suppliers suggested that it was approximately 50 % cheaper than Jelutong. The material was however more unstable than Jelutong and very brittle, and thus required a low viscosity, deep penetrating polyurethane adhesive coating to be painted on the mould surface to stabilise the material for handling and machining.

After choosing the HDPU material for the mould, the diffuser was manufactured using a CNC machine at CAM Services manufacturing company. A large CNC cutting bed was necessary to produce the mould with as little sub-divisions needed to be made to the mould. The CAD model of the mould can be seen in the figure 7.1.

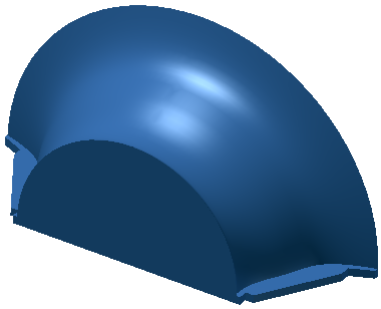

Figure 7.1: CAD model of diffuser mould.

For the CNC machining the mould was made in four layers that were glued together at a later stage. On each layer locating holes were created so that all four layers would line up accurately. The final mould is shown in the figure 7.2 below.

Figure 7.2: Polyurethane foam mould for diffuser.

In figure 7.2, no flanges where present as presented in the CAD model. A backing board with appropriate dimensions was glued to the back of the mould to create the necessary flanges. After the mould was complete, a fibreglass hand lay-up was done to produce two diffuser halves. The diffuser halves were manufactured using CSM 450 g/m^2 fibreglass with a low shrinkage polyester resin (less than 1 % shrinkage).

Four application layers were necessary to ensure a wall thickness of 10 mm. The curing time per diffuser half was approximately 26 hours. The most critical surface with regard to diffuser performance was the inside, and a polished finish was given to it. After the

fibreglass manufacturing was completed, the diffuser dimensions needed to be checked to be within design tolerances.

In order to do this, the two fibreglass halves were joined using bolts and the four locations of the design variables used in the optimisation procedure were marked, out on the inside surface. The distance between locations of the variables were then measured and compared to the computer model. The results are presented in Table 7.1. In the table the direction "x" refers to the distance measured from the rotor plane along the rotor axis towards the diffuser exit (streamwise). The direction "y" refers to the distance measured from the rotor axis towards the diffuser surface (radial).

Table 7.1: Discrepancies between CAD diffuser and the manufactured diffuser.

Direction		x_1(m)	x_2(m)	x_3(m)	x_4(m)	Fixed point (m)
x	Computer model and fibreglass diffuser	0	0.1	0.2	0.3	0.4
y	Computer model	0.426	0.446	0.498	0.540	0.726
	Fibreglass diffuser	0.419	0.434	0.491	0.543	0.724

The manufactured diffuser's profile differed from the CAD model by approximately 2 to 12 mm. This was attributed to the amount of shrinkage incurred in the manufacturing process and the mould quality being not as expected. The variance however still falls well within the sensitivity limits as discussed in Chapter 5.4. Creating a CFD model representative of the manufactured diffuser predicted a value of $C_p = 1.64$. The manufactured diffuser's C_p then differs from the SVR model by 2%. The two diffuser halves fitted well together and the inlet and outlet plane was concentric.

7.2 Support Structure

In conjunction to the manufacturing of the diffuser, the support structure that houses the diffuser was manufactured independently according to the design presented in Appendix C and illustrated in figure C.4. This involved the creation of a drawing pack and sourcing of the required material to build the structure. After the support structure was completed, it was fitted with the diffuser - as can be seen in figure 7.3.

Figure 7.3: Manufactured support structure with diffuser.

7.3 Drive Train

The drive train consists of elements involved with the measurement of the turbine power. Some peripherals needed to be manufactured according to the researcher's measurement requirement. The main elements created was a frame that housed the drive train and also provides a interface with the support structure of the diffuser and the turbine. The main elements housed in the frame are illustrated in the figure 7.4.

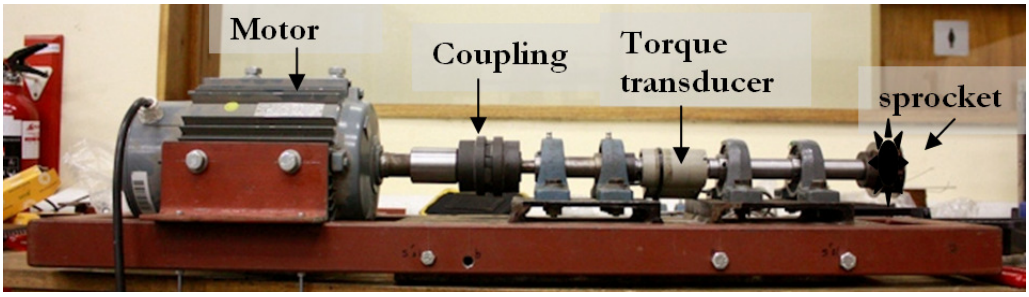

Figure 7.4: Drive train with elements.

7.4 Conclusion

In this section the basic manufacturing of the support structure and diffuser is presented simplistically. The main concerns and discrepancies between the CAD and manufactured diffuser are highlighted and discussed. It was found that although there is a small variance in geometric shape, it is still expected to produce accurate results. Some figures illustrate the assembly of the support rig with the diffuser; and finally a brief description of the top drive train was presented. The assembled support rig with diffuser, test equipment and installed rotor is shown in figure 7.5.

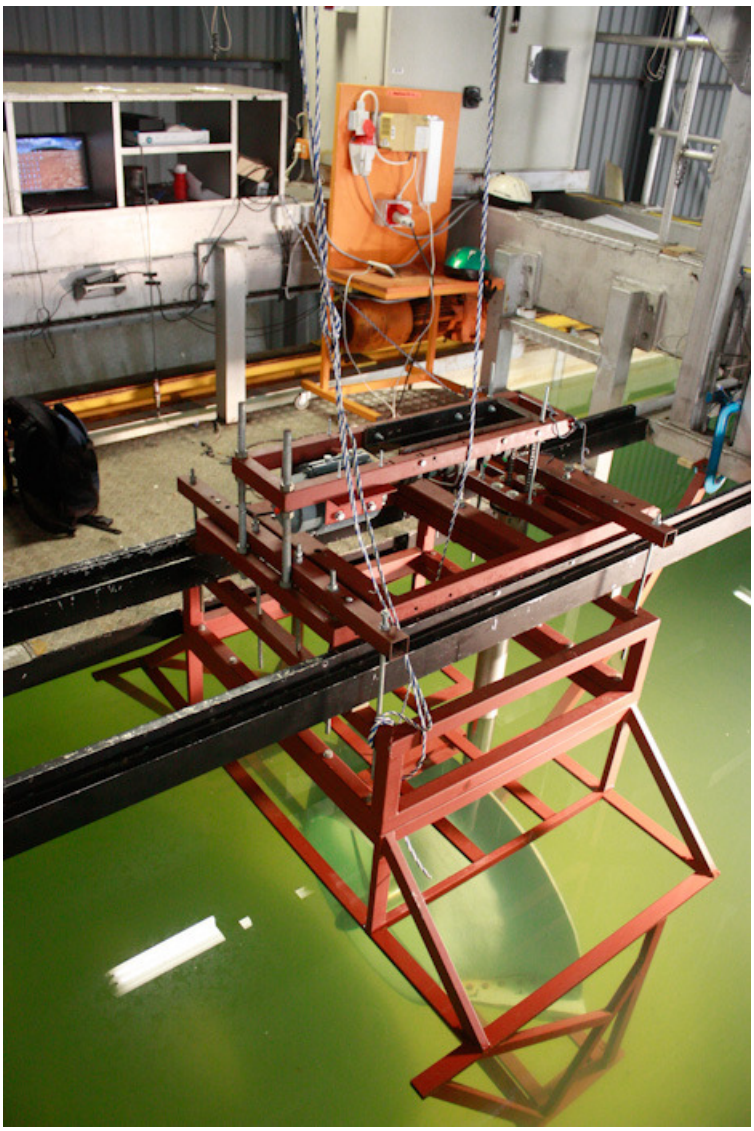

Figure 7.5: Assembled experimental setup.

Chapter 8

Model Ocean Current Turbine Testing

8.1 Experimental Methodology

For the experimental testing of the turbine diffuser system the towing tank facilities at Stellenbosch University was used. The towing tank has a length of 90 m, a depth of 2.4 m and width of 4.6 m. This is also one of the largest towing tank facilities in the Southern Hemisphere and previous model OCT tests have been conducted here successfully [16, 11]. It boasts a trolley where scale model ships or turbines can be attached and is then 'towed' through the tank to simulate flow conditions from 0 m/s to 9 m/s, see Appendix E.2 for photos and specifics.

To determine the power production of the turbine, a test setup similar to Reinecke [16] was used. This involved measuring the torque produced by the turbine by means of a torque transducer. The second variable that needed to be measured in order to determine the power output was the revolutions per minute (RPM) of the turbine shaft. By measuring these two variables the power could be determined as shown in the equation below.

$$P = T\omega \tag{8.1}$$

The shaft power is P (W), T is the torque (N.m) and ω is the RPM (rad/s). The test setup is shown diagrammatically in figure 8.1.

As seen in figure 8.1, speed is controlled by means of a variable speed drive (VSD) that changes the frequency of the feed-in power between 0 and 60 Hz and as a result controls the generator RPMs. By doing this, when the motor is in operation and the turbine produces power the motor will attempt to maintain its steady state RPM as determined by the VSD, although it would not be able to completely follow the unloaded RPM speed

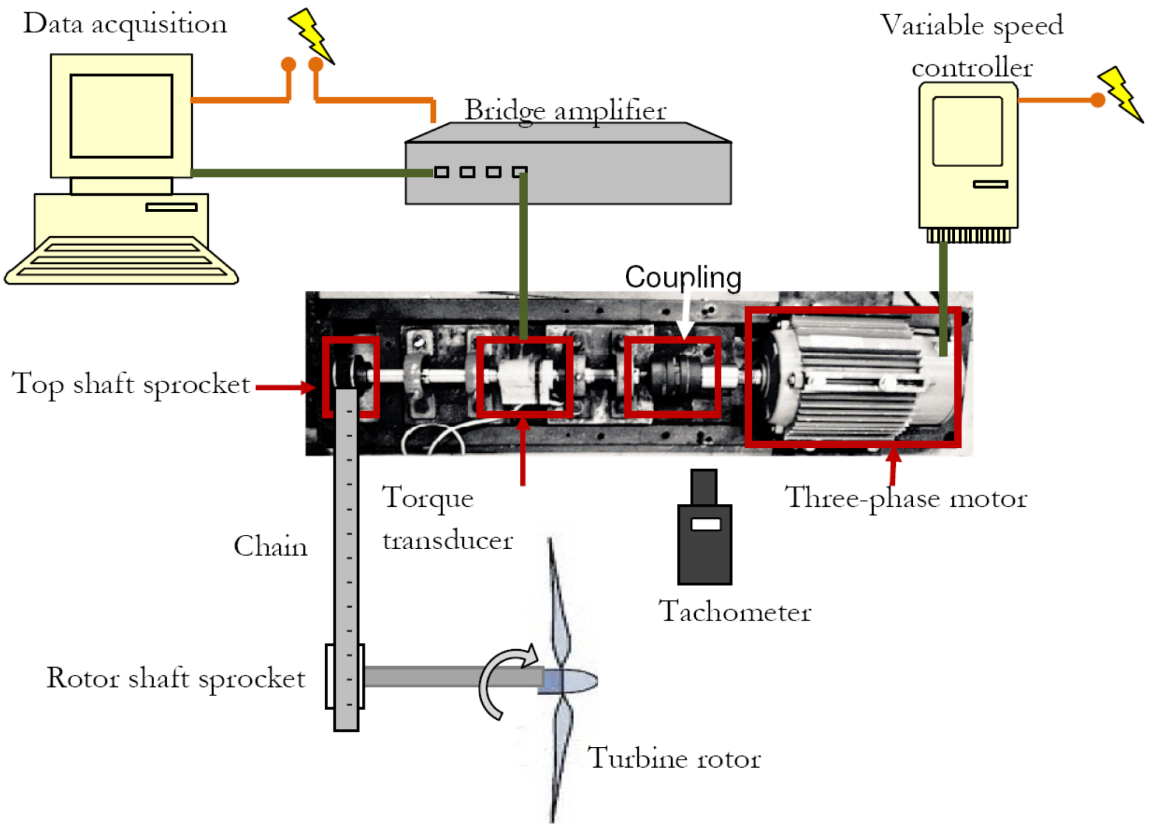

Figure 8.1: Experimental setup.

and will thus start to generate power. This braking effect is equivalent to the torque produced by the motor and hence the power can be determined.

Also important to observe is that a hand-held tachometer is used to measure the shaft RPMs. From figure 8.1 it is evident that the data acquisition is all conducted on the top shaft or top drive train. Additional details of the equipment can be found in Appendix E.

The power produced by the turbine is transmitted through a chain and sprocket system. The top shaft pulley is in turn connected to the torque transducer and to the motor via a coupling. Thus system losses associated with the chain and sprockets needed to be taken into account when calculating the turbine power production. These can be found in Appendix D.

Measurement of the torque was done by using the torque transducer in conjunction with a bridge amplifier and data capture device. The bridge amplifier can handle a sampling rate of up to 300 Hz and provided real time observation of the torque measurement.

The flow speed that needed to be simulated in the towing tank experiment was 1.5 m/s and data needed to be collected for a TSR ranging from two to 12. Figure 8.2 shows the actual experimental setup. For the tests the rotor axis was centred at a depth of 1.2 m below the water surface and 2.3 m from the sides of the tank.

Figure 8.2: Actual test setup.

8.1.1 Test Procedure

The testing procedure first and foremost was dealt with by keeping personnel safety in mind. As shown in figure 8.3 the procedure started by first checking that the operation of the experiment was safe. After this the data capturing was initiated, followed by the initiation of the motor at a specific speed. The test then commenced for about 50 m down the towing tank length after which it was halted and the motor stopped.

The data was then logged and a decision was made regarding whether the data was of a stable nature or whether to repeat the test for the specific performance point. In both cases the trolley proceeded back to its starting position.

Should the recorded data exhibit measurement noise in excess of 15 % of the average torque reading or 10 % of the trolley set velocity was exceeded during the test, the test would be redone.

The experimental tests involved two sets of different rotors to be tested. The specific rotors used are those designed by Bahaj with particulars presented in [71]; and those of Stanford in [72]. These were also used in Grobbelaar [11], allowing accurate comparisons of the diffusers performance.

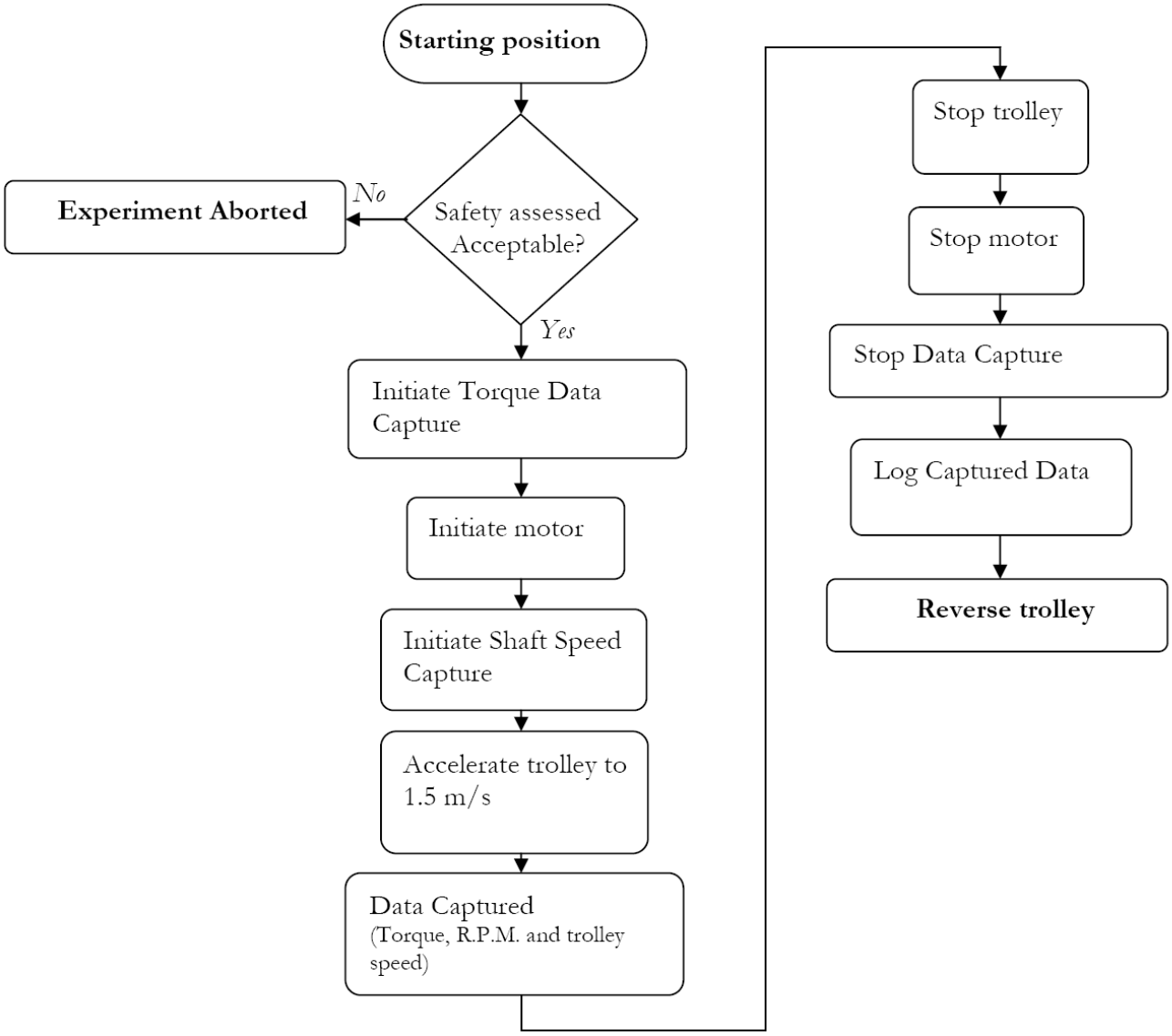

Figure 8.3: Testing procedure.

In order to obtain accurate experimental results, the test equipment needed to be calibrated. Various procedures were used and are discussed in Appendix E.

8.1.2 Discrepancies

Installation of the test rig was tedious owing to the fact that the diffuser support structure and the turbine are two independent structures. During installation, locating the rotor correctly in the diffuser was critical. Underwater inspection needed to be conducted along with some minor adjustments to the positioning of the diffuser structure. This was achieved successfully.

During testing some results showed a non-stable trend for part of the testing length. This is ascribed to the acceleration and deceleration the trolley experienced in each test run. This in turn produced an added mass of the water around the rotor blades and the rotor could not respond immediately to the change in flow conditions. From all the tests conducted, a stable measurement existed for at least 10 m (or seven seconds of data capture) of towing length.

The final problem encountered involved the use of the two kW three-phase motor used to apply braking to the system. Because both the rotor shafts and the top drive train shaft are connected via a chain and sprocket system the researcher was able to scale the rotational speeds of the shafts by using different sprocket ratios.

Ideally running the 2 kW motor with high RPMs increases the effectiveness of the braking effect and allowed the diffuser-augmented turbine to be tested across a wide range of TSR. Some slippage between the motor stator and rotor was encountered between TSRs of 2 to 3.5 (low RPMs) but was corrected by applying the correct gearing ratio.

It should also be mentioned that the data suffered from some scatter in the torque measurement. This scatter is attributed to slight misalignment existing between the torque transducer shaft and the shaft containing the sprocket. By applying an averaging scheme to the data it could be reduced to within 0.6 N.m variance. Detection of outliers in post-processing was conducted using the three-sigma test described in [73].

Additionally, the free surface effects was not accounted for in post-processing of the data as the effect it had on the performance could not be quantified appreciably. The free surface effects can be seen in Appendix E.

8.1.3 Blockage Effects

It was assumed that blockage effects were affecting the test experiments, but the degree of such influences needed to be determined. Considering that the towing tank has a cross-sectional area of 11.5 m^2 and the turbine diffuser system an area of 1.65 m^2, a area ratio of 0.14 existed or blockage of 14 %. Some theories for blockage calculation in bare turbines are presented in [71] and [74]. It was attempted to implement these theories to our study but differing corrections were found; suggesting a blockage correction of between 5 % and 12 % to be made to the data.

To circumvent the lack of theoretical guidelines a CFD investigation was conducted and entailed the simulation of three different fluid space sizes; one resembling the towing tank water depth and diffuser-augmented turbine; one the infinitely high water level height, and one similar to the depth used in the DOE function evaluations. Calculating the power

production from these results yielded essentially the same power production: respectively 1473.2 W, 1448.8 W and 1443.2 W. Thus a variance of less than 2 %. Please refer to Appendix B for simulation details and axial velocity plots.

Due to the difference in predictions from literature and CFD it was decided not to incorporate blockage effects into the data analyses.

8.2 Experimental Results

The results shown here represent the testing of two different rotor blades inside the optimised diffuser. The first set is named the Bahaj rotor [71]. This was also the rotor that was approximated for the diffuser design. The second set of blades were designed by a previous student for his final year project, termed the Stanford rotor [72]. For the Stanford blades a second set of carbon fibre blades were manufactured by Dippenaar [75]. Raw data can be found in Appendix E.

8.2.1 Towing Tank Test Results

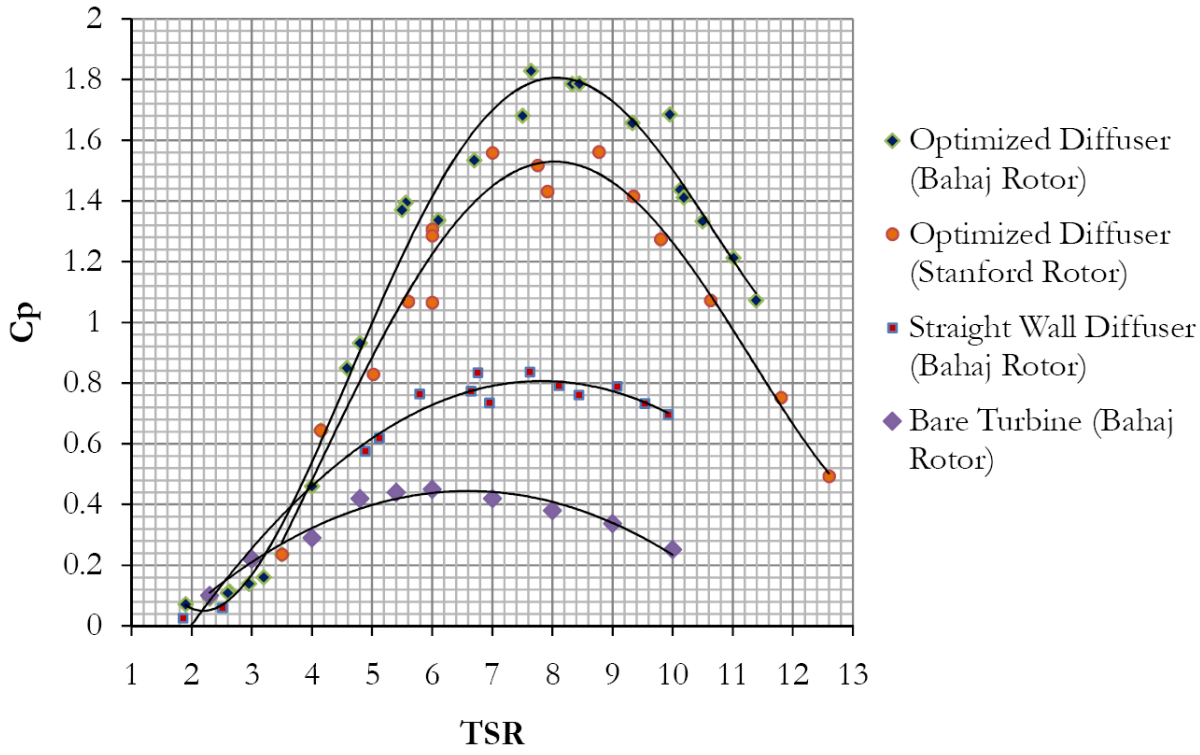

Figure 8.4: Performance curve of tested turbine diffuser systems (Power versus TSR).

Figure 8.4 shows the measured power from the experimental tests for the various diffuser-augmented turbines and including the straight wall diffuser of Grobbelaar [11] and the bare turbine performance for the Bahaj rotor. Between a TSR of two to four it can be seen that the performance with the optimised diffuser is worse than the other data sets.

This initial dipping in performance is attributed to the fact that the diffuser was optimised for a single performance point (TSR of eight) and not over the entire flow range. For this reason the boundary layer is adversely affected in the low TSR range and thus separation occurs and impedes the flow of the wake and leads to a drop in performance.

As the TSR is increased the diffuser effect is invoked; attachment of the boundary layer occurs and a rapid rise in power is experienced between a TSR four and seven. The performance levels out and then reaches a maximum of 1512 W at a TSR of 7.9. After this point, however, the pressure gradient becomes too great behind the rotor and the boundary layer separates causing a fall in performance. The next figure indicates the same graph, now in terms of the C_p versus TSR.

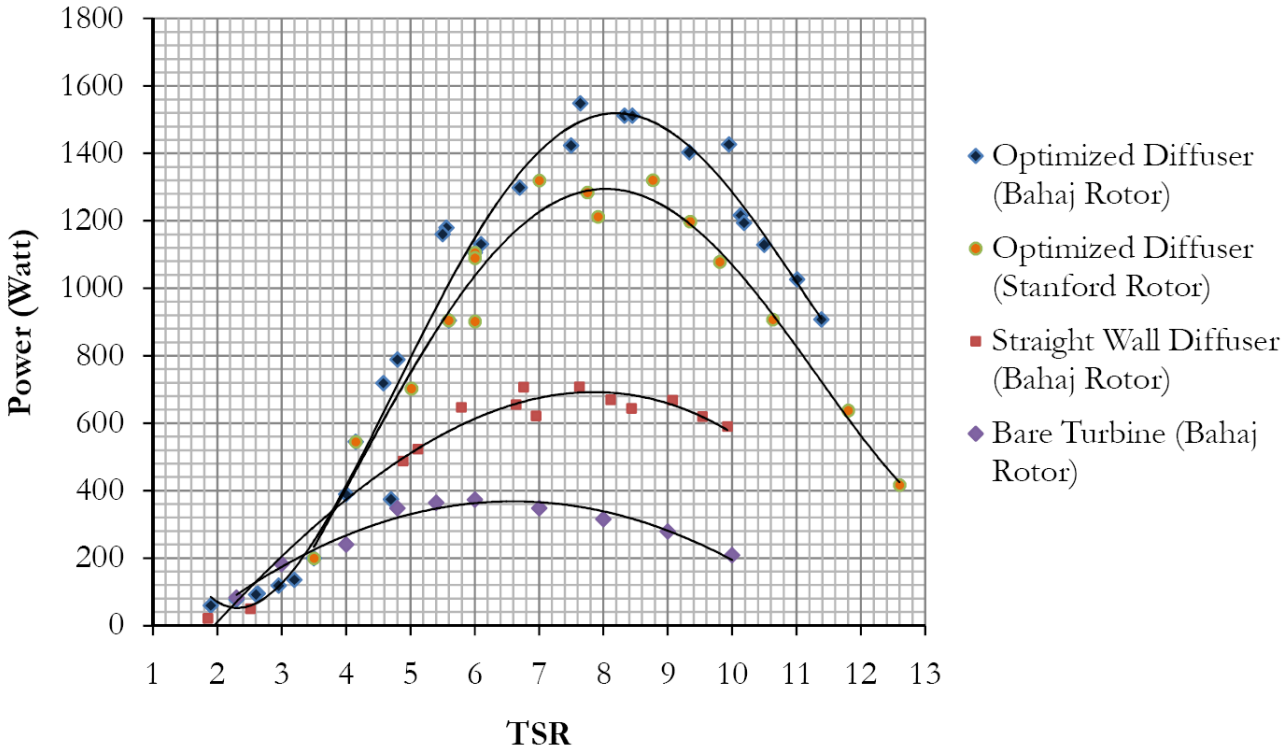

Figure 8.5: Performance curve of tested turbine diffuser systems (Power versus TSR).

From the figures it can be seen that the optimised diffuser out performs the straight wall diffuser and that the Bahaj blades proved to be the rotor-set yielding the highest power rating.

8.2.2 Comparison Between CFD and Model Tests

For the comparison of CFD against the optimised diffuser with the Bahaj rotor set, only the maximum power production was considered as this is also the point that was optimised. For the test results, the maximum measured power that was within statistical confidence levels was used. The findings are shown below.

Table 8.1: CFD versus test results.

	C_p	**Power (Watt)**
CFD	1.672	1448
Test Results	1.745	1512

From Table 8.1 it can be seen that an under-prediction of power generated by the CFD model exists and amounted to 4.2 %. This under prediction, contrary to [58] over prediction, is ascribed to the blockage effects affecting the results. Even with a blockage effect of 10 %, the experimental results compare well with the CFD prediction.

8.2.3 Comparative analyses Between Previous Studies

For the comparative analyses five different data sets were analysed. These sets, with their names as found in the histograms that will follow, are listed below all results are experimentally extracted except the 'scaled' results that are mathematically calculated from the existing results.

- Bare Turbine (Bahaj: This refers to the Bahaj rotor performance without a diffuser added; it has $C_p \approx 0.44$.
- Scaled (Bahaj): Refers to the above "Bare Turbine" with the rotor diameter being increased to match the outside diameter of the optimised diffuser (1.452 m).
- Grobbelaar (Bahaj): Refers to the diffuser-augmented turbine of Grobbelaar [11] with the Bahaj rotor set.
- Optimised Diffuser (Bahaj): Refers to the diffuser-augmented turbine using the optimised diffuser with the Bahaj rotor set.
- Bare Turbine (Gaden): This refers to bare turbine of Gaden [62].
- Optimised (Gaden):This refers to diffuser-augmented turbine of Gaden [62].
- Scaled (Gaden):This refers to bare turbine of Gaden [62] scaled up to the outside diameter of his diffuser (3 m).

Table 8.2: Comparisons in performance of various diffuser-augmented and bare turbine systems.

	Max Power (W)	Max C_p	Scaled C_p	Improvement over bare turbine (%)
Bare Turbine (Bahaj)	372	0.44	0.13	0
Grobbelaar (Bahaj)	691	0.84	0.25	85.24
Optimised (Bahaj)	1512	1.74	0.54	305.9
Scaled (Bahaj)	1227	1.45	0.44	229.4

Table 8.3: Comparisons in performance of the diffuser-augmented turbine of Gaden.

	Max Power (kW)	Max C_p	Scaled C_p	Improvement over bare turbine (%)
Bare Turbine (Gaden)	16.4	0.27	0.13	0
Optimised (Gaden)	34.9	0.85	0.54	212.8
Scaled (Gaden)	25.8	0.43	0.27	57.3

8.2.4 Conclusion: Result Interpretations and Synthesis

In the test results the relative motion between the rotor and diffuser was dealt with fully by designing a low-deflection test rig to minimise shape warp and then also by fixing the diffuser against the rotor upright to allow for minimal, if any, deflection.

From Tables 8.2 and 8.3, various comparisons are made. Most importantly is the increase in power of the optimised diffuser (Bahaj) over the bare turbine (Bahaj) by a factor of four. This comes at a cost of area increase by a factor of 3.29.

Determining the real gain in power performance of the optimised diffuser (Bahaj) needs to be compared to a scaled up bare turbine (Bahaj) of similar size to the apparent area of the diffuser. The result is a factor increase in power of 1.23 (from 1227 W to 1512 W) over the scaled up turbine.

The bare turbine (with Bahaj rotor) produces its maximum power at a much lower TSR than the optimised diffuser turbine (Bahaj) and thus generates a greater torque and hence would require a larger and more expensive drive train. This has large economical effects as the cost of a generator and gearbox forms a considerable part of turbine initial capital expenditure.

Comparing the optimised diffuser (Bahaj) to Grobbelaar (Bahaj), a factor increase in power of 2.19 has been achieved. Thus for a given geometric envelope a more geometric complex shape delivers greater improvements than a simplistically-designed diffuser. The gain in the power increase possible by using a more rigorous optimisation approach is also shown.

This power augmentation achieved by the optimised diffuser together with the comparison between predicted CFD results and experimental testing validates the use of the design methodology. It also highlights the improvements possible when applying SVR optimisation techniques.

Chapter 9

Conclusion

9.1 Summary of Findings

9.1.1 CFD Function Evaluation

The CFD function evaluation used in the optimisation consisted of 2D-axisymmetric mesh and utilised a k-ε turbulence model. The use of which was validated against 1D-turbine theory and found to be within 5 % variance of the design point. In addition the grid was parametrised and the use of journal files for grid creation and simulation used to enable automation of the analyses. This in turn enabled the parallelisation of the function evaluation.

9.1.2 SVR Modelling Technique and Implementation

Firstly, a DOE was created using a space filling Latin Hyper Cube. This consisted of 110 training points and 25 test points; each point representing a specific CFD analyses with a unique diffuser shape. In order to analyse this amount of points, a parallel computing scheme was used.

After the points were generated, accurate fitment of the SVR and RS metamodels to the points were conducted and the models optimised. The SVR model, outperformed the RS model but only by 3.9%.

The SVR optimisation yielded an optimum shape and predicted a theoretical increase in power by a factor 3.77 or a maximum power of 1448 W.

9.1.3 FEM and Topology Optimisation

For the design of the diffuser and the support structure necessary to test the diffuser turbine system, FEM in conjunction with topology optimisation were employed. This method decreased the amount of time spent on the concept design stage considerably. Using this the researcher was able to decrease the amount of maximum deflection on the support structure from 28 mm to 8.3 mm. Failure of the structure due to buckling and stress was not predicted by the FEM model.

9.1.4 Test Equipment

For the testing of the diffuser turbine system all the measurement equipment was calibrated and an efficient testing procedure was designed. This process allowed accurate measurements to be recorded.

9.1.5 Experimental Results

The results were calculated from the data obtained during testing in the towing tank facility. Some discrepancies in data existed due to the dynamic changes experienced by the trolley in terms of velocity. This showed a change in speed over a test run ranging from 1.55 m/s to 1.43 m/s. By data checking and statistical analyses, however, these runs were considered outliers and were not included in the data sets.

The results showed the increase in the performance of the optimised diffuser to be twice that of the straight wall diffuser of Grobbelaar and a factor four greater than the bare turbine. The maximum power measured was 1512 W. The maximum power measured differed by less than 5 % from the predicted CFD results.

9.2 Conclusion

The research aimed to investigate the effect that a diffuser has on a model OCT turbine. For this study the following conclusions are made as it pertains to the research objectives:

- A power increase of a factor four (or in terms of power, 1512 W instead of 378 W) has been achieved by the use of a diffuser over the bare turbine. To explain it simply, it has been found that a single diffuser-augmented turbine is equal in power output to the combined power of four bare turbines. This is of influence on the real world as using a diffuser-augmented turbine reduces system complexity to produce a

certain amount of power. Instead of four separate installations only one installation is necessary. The increase in power of the optimised diffuser over the bare turbine resulted in an increase in torque by a factor of 2.28.

- In addition this increase of kinetic energy density that is exhibited has an effect on source selection for real world applications. It was found from CFD that the flow speed at the rotor was increased by a factor of 1.34. Considering that an ocean or tidal site is selected with a minimum criteria in flow speed of 1.5 m/s to 2 m/s, slower moving flows by a factor of 1.34 (or minimum flow speed of 1.1 m/s) can be utilised for diffuser-augmented systems. Thus increasing the application area of where OCTs can be utilised.

- The amount of augmentation was also found to be better predicted for this specific diffuser turbine system by the ratio of rotor axial velocity cubed, thus challenging the proposition of Hansen [21, 18]. The new proposed equation differed from CFD results by less than 1.2 %. Applying equation 2.34 to the results of [9, 12] we find that the difference between results is 1.1 % and 1.7 % respectively.Equation 2.34 is formulated as:

$$\frac{C_{p,d}}{C_{p,b}} = \frac{V^3_{rotor,d}}{V^3_{rotor,bare}}$$

- In addition, the power predicted by the CFD (actual manufactured dimensions) was 1422 W compared to the test results of 1512 W - a difference of less than 5 %. Thus validating the research design method and applicability for use in other diffuser design studies.

- The optimum SVR-determined diffuser shape indicated a sizable tip clearance as exploited in [58]; a bell-shaped mid section as found in [61] and a highly angled end part similar to the flanged results in [12]. Thus it can be seen that various dynamics influenced the diffuser shape and the SVR theory seems to have incorporated the best effects effectively by defining the diffuser shape by a B-spline.

In conclusion the research objectives have been met and results are of value for the theoretical application of future diffuser design, and holds valuable insights to real world application.

9.3 Suggestions for Future Work

- **Diffuser Design:** The design of the diffuser can be expanded to include annular airfoil shapes and a similar optimisation approach used where the airfoil shape and

placements can be varied. An important study could involve the optimisation of a diffuser in iterations of diffuser area ratio, thus optimising a shape given a diffuser area ratio of 1.2, 1.5, 2, etc. This will provide data in order to perform economic feasibility studies.

- **Economic feasibility:** A study involving the economical comparison between multiple bare turbine systems and a single diffuser-augmented system should be conducted to determine the economical benefits of a full-scale application of diffusers.

- **Test facility:** For future model OCT studies at Stellenbosch University a permanent support structure that can house various types of diffusers and rotor diameters is suggested. In addition measurement equipment should be made available that can all be logged simultaneously to a single data-capturing device, as various dynamic effects were encountered during testing.

Bibliography

[1] EU renewable energy policy [Online]. Available at: http://www.euractiv.com/en/energy/eu-renewable-energy-policy/article-117536, Apr 2010. 1

[2] Executive summary of the draft integrated electricity resource plan for south africa - 2010 to 2030 [Online]. Available at: http://www.doe-irp.co.za/content/Executive_Summary_Draft_IRP2010_8Oct2010.pdf, Oct 2010. 1

[3] Chanel de Bruyn [Online]. DoE recommends 'balanced' scenario in 20-year power plan[Online]. Available at: http://www.engineeringnews.co.za/article/doe-publishes-draft-20-year-electricity-plan-for-south-africa-2010-10-07, Oct 2010. 1

[4] F.O. Rourke, F. Boyle, and A. Reynolds. Marine current energy devices: Current status and possible future applications in Ireland. *Renewable and Sustainable Energy Reviews*, 2009. 1, 15, 16, 17, 25

[5] PL Fraenkel. Power from marine currents. *Proceedings of the Institution of Mechanical Engineers, Part A: Journal of Power and Energy*, 216(1):1–14, 2002. 2

[6] Zolisa Mgwatyu [Online]. Switch on ocean current. Available at: http://www.dispatch.co.za/article.aspx?id=369837, Dec 2009. 2, 17

[7] S. Schwartz, K. Argyriadis, and G.L. WindEnergie. Certification of ocean current turbines. In *6th European Wave and Tidal Energy Conference (EWTECŠ05), Glasgow*, 2005. 2, 3

[8] P.L. Fraenkel. Tidal current energy technologies. *Ibis*, 148(s1):145–151, 2006. 3, 16

[9] D.L.F. Gaden and E.L. Bibeau. A numerical investigation into the effect of diffusers on the performance of hydro kinetic turbines using a validated momentum source turbine model. *Renewable Energy*, 2009. 3, 7, 20, 23, 24, 28, 29, 58, 83

[10] WMJ Batten, AS Bahaj, AF Molland, and JR Chaplin. Hydrodynamics of marine current turbines. *Renewable energy*, 31(2):249–256, 2006. 3

[11] PJ Grobbelaar. CFD simulation, design, manufacture and testing of a diffuser augmented ocean current turbine. Final year project, Mechanical Engineering,University of Stellenbosch, Stellenbosch, South Africa, 2008. 3, 5, 27, 29, 30, 34, 48, 63, 64, 71, 73, 77, 78, C–1

[12] T. Matsushima, S. Takagi, and S. Muroyama. Characteristics of a highly efficient propeller type small wind turbine with a diffuser. *Renewable Energy*, 31(9):1343–1354, 2006. 3, 4, 7, 22, 23, 25, 28, 29, 58, 63, 83

[13] H. Grassmann and ML Ganis. On partially static Kaplan turbines. *Renewable energy*, 30(2):179–186, 2005. 3, 21, 25, 29

[14] P. Jamieson. Generalized limits for energy extraction in a linear constant velocity flow field. *Wind Energy*, 11(5):445–457, 2008. 4, 8, 19, 21, 30

[15] O. Igra. Compact shrouds for wind turbines. *Energy Conversion*, 16(4):149–157, 1977. 4, 19, 20

[16] J Reinecke. The Design Manufactrure and Testing of a Model Ocean Current Turbine. Final year project, Mechanical Engineering,University of Stellenbosch, Stellenbosch, South Africa, 2007. 5, 27, 29, 71

[17] F. Bet and H. Grassmann. Upgrading conventional wind turbines. *Renewable Energy*, 28(1):71–78, 2003. 7, 21

[18] M.O.L. Hansen. *Aerodynamics of wind turbines*. Earthscan/James & James, 2008. 8, 9, 14, 83

[19] A. Betz. Das Maximum der theoretisch möglichen Ausnützung des Windes durch Windmotoren. *Zeitschrift für das gesamte Turbinenwesen*, 26:307–309, 1920. 8

[20] D.G.J.W. Bussel. The science of making more torque from wind: Diffuser experiments and theory revisited. In *Journal of Physics: Conference Series*, volume 75, page 012010. IOP Publishing, 2007. 8

[21] M.O.L. Hansen, N.N. Sørensen, and RGJ Flay. Effect of placing a Diffuser around a Wind Turbine. *Wind Energy*, 3(4):207–213, 2000. 8, 15, 29, 83

[22] G.A.M. van Kuik. The Lanchester-Betz-Joukowsky limit. *Wind Energy*, 10(3):289–291, 2007. 8

[23] F.W. Lanchester. A contribution to the theory of propulsion and screw propeller. *Transactions of the Institution of Naval Architects*, (57):98–116, 1915. 8

[24] KH Bergey. The Lanchester-Betz limit. *Journal of Energy*, 3:382–384, 1979. 8

[25] N.E. Joukowsky. Windmill of the NEJ type. *Transactions of the Central Institute for Aero-Hydrodynamics of Moscow*, 1(57), 1920. 8

[26] R.E. Froude. On the part played in propulsion by diffrences of fluid pressure. *Transactions of the Institution of Naval Architects*, (30):390–405, 1889. 9

[27] B. Kirke. Developments in ducted water current turbines. *School of Engineering, Griffith university, Australia*, 2003. 16

[28] MJ Khan, G. Bhuyan, MT Iqbal, and JE Quaicoe. Hydrokinetic energy conversion systems and assessment of horizontal and vertical axis turbines for river and tidal applications: A technology status review. *Applied Energy*, 86(10):1823–1835, 2009. 16, 17

[29] Adam Westwood. Seagen tidal installation moves forward [Online]. Available at: `http://www.renewableenergyfocus.com/view/3330/seagen-tidal-installation-moves-forward-/`, Feb 2010. 16, 18

[30] JV Norris and E. Droniou. Update on EMEC activities, resource description, and characterisation of wave-induced velocities in a tidal flow. In *Proceedings of the 7th European Wave and Tidal Energy Conference*, pages 11–14, 2007. 16

[31] F.O. Rourke, F. Boyle, and A. Reynolds. Renewable energy resources and technologies applicable to Ireland. *Renewable and Sustainable Energy Reviews*, 13(8):1975–1984, 2009. 16, 17

[32] G. Calcagno, F. Salvatore, L. Greco, A. Moroso, and H. Eriksson. Experimental and numerical investigation of an innovative technology for marine current exploitation: the Kobold turbine. In *Proceedings of the Sixteenth International Offshore and Polar Engineering Conference*, pages 323–330, 2006. 16

[33] A.M. Gorlov. Helical turbines for the Gulf Stream: Conceptual approach to design of a large-scale floating power farm. *Marine technology*, 35(3):175–182, 1998. 16

[34] JA Clarke, G. Connor, AD Grant, CM Johnstone, and D. Mackenzie. Development of a contra-rotating tidal current turbine and analysis of performance. *Gas*, 20:23. 16

[35] F. O'Rourke, F. Boyle, and A. Reynolds. Tidal energy update 2009. *Applied Energy*, 87:398–409, 2010. 16, 17

[36] OpenHydro [Online]. Technology: open-centre turbine. Available at: `http://www.openhydro.com/techOCT.html`, Jun 2010. 16

[37] P. Bresesti, W.L. Kling, R.L. Hendriks, and R. Vailati. HVDC connection of offshore wind farms to the transmission system. *IEEE Transaction on Energy Conversion*, 22(1):37–43, 2007. 16

[38] R.H. Charlier. A" sleeper" awakes: tidal current power. *Renewable and Sustainable Energy Reviews*, 7(6):515–530, 2003. 17

[39] IG Bryden, SJ Couch, A. Owen, and G. Melville. Tidal current resource assessment. *Proceedings of the Institution of Mechanical Engineers, Part A: Journal of Power and Energy*, 221(2):125–135, 2007. 17

[40] Siddiqui O Hagerman G Bedard R, Previsic M and Robinson M. EPRI Tidal In Stream Energy Conversion (TISEC) Project. 2005. 17

[41] G.D. Egbert and R.D. Ray. Estimates of M2 tidal energy dissipation from TOPEX/Poseidon altimeter data. *Journal of Geophysical Research*, 106(C10):22475, 2001. 17

[42] R. Bedard, M. Previsic, G. Hagerman, B. Polagye, W. Musial, J. Klure, A. von Jouanne, U. Mathur, C. Collar, C. Hopper, et al. North American ocean energy status–March 2007. *Electric Power Research Institute (EPRI) Tidal Power (TP)*, 8, 2007. 17

[43] D.J.C. MacKay. Under-estimation of the UK tidal resource. *Cambridge:[2006 Dec 7*, 2007. 17

[44] EIA [Online]. International Energy Statistics - Capacity. Available at: `http://www.eia.doe.gov/cfapps/ipdbproject/IEDIndex3.cfm?tid=2&pid=2&aid=7`, Jun 2010. 17

[45] NEWSNETSCOTLAND [Online]. Boost for Scottish renewables as worlds largest tidal turbine unveiled. Available at: `http://newsnetscotland.com/general/467-boost-for-scottish-renewables-as-worlds-largest-tidal-turbine-unveiled`, Jun 2010. 17, 18

[46] G. Cada, J. Ahlgrimm, M. Bahleda, T. Bigford, S.D. Stavrakas, D. Hall, R. Moursund, and M. Sale. Potential impacts of hydrokinetic and wave energy conversion technologies on aquatic environments. *Fisheries*, 32(4):174–181, 2007. 17

[47] EMEC [Online]. Tidal Developers. Available at: `http://www.emec.org.uk/tidal_developers.asp`, Aug 2010. 17, 25

[48] Honey Garcia [Online]. Scotland supports marine energy projects with USD 20 million. Available at: `http://ecoseed.org/en/water-power/wave-and-tidal-energy/article/64-wave-and-tidal-energy/7553-scotland-supports-marine-energy-projects-with-$-20-million`, Jul 2010. 18

[49] Ham [Online]. HS300. Available at: `http://www.hammerfeststrom.com/content/view/66/101/lang,en/`, Jan 2010. 18

[50] Stuart Nathan [Online]. Turning the tide at the European Marine Energy Centre. Available at: `http://www.theengineer.co.uk/in-depth/turning-the-tide-at-the-european-marine-energy-centre/298750.article`, Sept 2010. 18

[51] Robin Shulman. N.Y. Tests Turbines to Produce Power. Available at: `http://www.washingtonpost.com/wp-dyn/content/article/2008/09/19/AR2008091903729.html`, Sept 2008. 18

[52] Jamais Cascio [Online]. Gorlov's Helical Turbine. Available at: `http://www.worldchanging.com/archives/002383.html`, Jul 2010. 18

[53] O. Igra. Research and development for shrouded wind turbines. *Energy Conversion and Management*, 21(1):13–48, 1981. 19, 20, 21, 25, 28, 58

[54] C.A.J. Fletcher. Computational analysis of diffuser-augmented wind turbines. *Energy Conversion and Management*, 21(3):175–183, 1981. 20

[55] DG Phillips, PJ Richards, and RGJ Flay. Diffuser Development for a Diffuser Augmented Wind Turbine Using Computational Fluid Dynamics. *University of Auckland*. 20

[56] DG Phillips, RGJ Flay, and TA Nash. Aerodynamic Analysis and Monitoring of the Vortec Seven Diffuser Augmented Wind Turbine. In *Proceedings of the Annual Conference of the Institute of Professional Engineers NZ, Auckland*, 1998. 20

[57] A.P. Schaffarczyk, D. Phillips, and N.Z. Auckland. Design principles for a diffusor augmented wind-turbine blade. EWEC, 2001. 20, 21, 28

[58] H. Grassmann, F. Bet, M. Ceschia, and ML Ganis. On the physics of partially static turbines. *Renewable energy*, 29(4):491–499, 2004. 21, 25, 62, 78, 83

[59] H. Grassmann, F. Bet, G. Cabras, M. Ceschia, D. Cobai, and C. DelPapa. A partially static turbine–first experimental results. *Renewable Energy*, 28(11):1779–1785, 2003. 21, 23, 25, 28

[60] S. Benjanirat, L.N. Sankar, and G. Xu. Evaluation of turbulence models for the prediction of wind turbine aerodynamics. *AIAA paper*, 517:2003, 2003. 22

[61] J.I. Madsen, W. Shyy, and R.T. Haftka. Response surface techniques for diffuser shape optimization. *AIAA journal*, 38(9):1512–1518, 2000. 23, 26, 28, 29, 31, 44, 47, 48, 62, 63, 83

[62] D.L.F. Gaden. *An investigation of river kinetic turbines: performance enhancements, turbine modelling techniques, and an assessment of turbulence models*. PhD thesis, University of Manitoba, 2007. 23, 24, 25, 30, 63, 78, A–2, A–4

[63] S.B. Chitralekha and S.L. Shah. Application of support vector regression for developing soft sensors for nonlinear processes. *The Canadian Journal of Chemical Engineering*. 29

[64] S.M. Clarke, J.H. Griebsch, and T.W. Simpson. Analysis of support vector regression for approximation of complex engineering analyses. *Journal of mechanical design*, 127:1077, 2005. 31, 43, 44, 46

[65] F.A.C. Viana. *SURROGATES Toolbox User's Guide*, 2009. 32, 45, 53

[66] *FLUENT 6.3 User's Guide*, September 2006. 35, 37, 49, A–2, A–4, A–5, A–6

[67] H. Glauert. *Aerofoil and airscrew theory*. Cambridge University Press, 1926. 38

[68] M.L. Buhl Jr. A new empirical relationship between thrust coefficient and induction factor for the turbulent windmill state. Technical report, NREL/TP-500-36834. Golden, CO: National Renewable Energy Laboratory, September, 2004. 38, 40

[69] G.N. Vanderplaats. Multidiscipline Design Optimization. *Applied Mechanics Reviews*, 41:257, 1988. 41

[70] J.N. Wise. Optimization of a low speed wind turbine using support vector regression. Masters thesis, Mechanical Engineering,University of Stellenbosch, Stellenbosch, South Africa, 2009. 43, 44, 45, 46

[71] AS Bahaj, AF Molland, JR Chaplin, and WMJ Batten. Power and thrust measurements of marine current turbines under various hydrodynamic flow conditions in a cavitation tunnel and a towing tank. *Renewable Energy*, 32(3):407–426, 2007. 73, 75, 76

[72] R Stanford. Design of an ocean current turbine. Final year project, Mechanical Engineering,University of Stellenbosch, Stellenbosch, South Africa, 2008. 73, 76

[73] R.S. Figliola and D.E. Beasley. *Theory And Design For Mechanical Measurements*. John Wiley and Sons, fourth edition, 2006. 75, D–3

[74] Dr.M.J Werle. Wind Turbine Wall Blockage Corrections. Available at: |urlhttp://www.flodesign.org/pdf/BlockagePaper.pdf, [2010, August 22]. 75

[75] DJ Dippenaar. A technical and economical evaluation of RP technologies for RTM tooling. Masters thesis, Mechanical Engineering,University of Stellenbosch, Stellenbosch, South Africa, 2009. 76

[76] C.E. Carcangiu. *CFD-RANS study of horizontal axis wind turbines*. PhD thesis, Universita degli Studi di Cagliari, 2008. A–2

[77] Roy R Craig, Jr. *Mechanics of Materials*. John Wiley and Sons, second edition, 2000. C–5

Appendix A

Computational Fluid Dynamics: Theory

A.1 Reynolds-Averaged Navier-Stokes Equations

Computational fluid dynamics and the prediction of finite-volume fluid motion and properties is based on the fundamental momentum, mass and energy conservation equations, which is known as the Navier-Stokes equations. For incompressible Newtonian fluid, the continuity equation using Cartesian coordinates and vector notation can be expressed as:

$$\frac{\partial u_i}{\partial x_i} = 0 \tag{A.1}$$

Here x_i is the i^{th} spatial dimension and u_i is the instantaneous velocity in the i^{th} direction. The equation for conservation of momentum can be written as:

$$\rho\left(\frac{\partial u_i}{\partial t} + \frac{\partial}{\partial x_j}(u_i u_j)\right) = -\frac{\partial p}{\partial x_i} + \mu\frac{\partial}{\partial x_j}\left(\frac{\partial u_i}{\partial x_j} + \frac{\partial u_j}{\partial x_i}\right) + S_{M,i} \tag{A.2}$$

$S_{M,i}$ is the momentum source term, ρ is the fluid density, p fluid pressure and μ the dynamic viscosity. Here u can be decomposed to consist of an average velocity component U and a fluctuating component u'. The instantaneous velocity equation can be written as:

$$u(x,t) = U(x,t) + u'(x,t) \tag{A.3}$$

where,

$$U(x,t) = \lim_{N\to\infty} \frac{1}{N} \sum_{n=1}^{N} u^{(n)}(x,t) \tag{A.4}$$

The Reynolds-averaged Navier-Stokes (RANS) equations, for continuity, is defined as follows:

$$\frac{\partial U_i}{\partial x_i} = 0 \tag{A.5}$$

and for the conservation of momentum equation:

$$\rho \left(\frac{\partial U_i}{\partial t} + \frac{\partial}{\partial x_j}(U_i U_j) \right) = -\frac{\partial p}{\partial x_i} + \frac{\partial}{\partial x_j} \left(\mu \frac{\partial U_i}{\partial x_j} \right) + \frac{\partial R_{ij}}{\partial x_j} \tag{A.6}$$

where R_{ij} is termed the Reynolds stress tensor.

R_{ij} is added to the momentum equation due to additional unknowns incurred by the averaging procedure. These Reynolds stresses must be modelled in order to solve the RANS equations. This is termed the closure problem where three unknowns namely, U, p and μ_t exist with only two equations available to solve them [62, 76]. This dilemma can be solved in one of two ways, the first is to use the Boussinesq hypothesis that postulates that the momentum transfer can be described by a molecular viscosity. For this case the Reynolds stresses can be described using an eddy viscosity (turbulent viscosity) μ_t. The second solution to the closure problem is using the Reynolds-stress models that can be implemented to solve the transport equations for the individual Reynolds stresses. For the k - ε and k - ω models that follows the Boussinesq hypothesis, R_{ij} is given by:

$$R_{ij} = -\rho \overline{u_i' u_j'} = \mu_t \left(\frac{\partial U_i}{\partial x_j} + \frac{\partial U_j}{\partial x_i} \right) \tag{A.7}$$

The Boussinesq hypothesis, however , is not without its limitations. The velocity gradients and R_{ij} is calculated using a scalar, u_t, instead of a tensor [62]. This is a reasonable formulation for simple turbulent flows involving boundary layers and mixing layers that allows a robust and computationally inexpensive solution [66, 76]. For highly anisotropic turbulence or complex 3D turbulent flows the Reynolds-stress models are preferred, but at higher computational cost and less stability in convergence.

Based on dimensional analyses, u_t can be calculated from a turbulence velocity scale and/or a length scale. For different turbulence models the calculation of u_t is conducted differently. In this research only two turbulence models were investigated namely the $k-\varepsilon$ and $k-\omega$ models.

Both of these models are two equation models that solve the transport equations for k, ε and ω and are defined in Fluent as:

$$k \equiv \frac{\overline{u_i' u_j'}}{2} \tag{A.8}$$

$$\varepsilon \equiv \upsilon \overline{\frac{\partial u_i'}{\partial x_j}\left(\frac{\partial u_i'}{\partial x_j} + \frac{\partial u_j'}{\partial x_j}\right)} \tag{A.9}$$

$$\omega \approx \frac{\varepsilon}{k} \tag{A.10}$$

where k is the turbulence kinetic energy, ε is the turbulence dissipation rate and ω is the specific dissipation rate.

A.1.1 Wilcox $k-\omega$ model

The Wilcox and standard model is an empirical based model that describes the transport equations of k and ω. In the solver used, Fluent, the $k-\omega$ standard model is based on the Wilcox $k-\omega$ model, that incorporates certain modifications for low-Reynolds-number effects, compressibility and shear flow spreading. In this dissertation the formulation of the Wilcox model only will be presented as it describes the underlying formulation of the standard model. For the Wilcox model u_t is defined as:

$$u_t = \left(\frac{\rho k}{\omega}\right) \tag{A.11}$$

and the transport equations are formulated as:

$$\rho\frac{\partial k}{\partial t} + \rho\frac{\partial}{\partial x_i} = \frac{\partial}{\partial x_j}\left[\left(\mu + \frac{\mu_t}{\sigma_k}\right)\frac{\partial k}{\partial x_j}\right] + G_k - Y_k + S_k \tag{A.12}$$

$$\rho\frac{\partial \omega}{\partial t} + \rho\frac{\partial}{\partial x_i} = \frac{\partial}{\partial x_j}\left[\left(\mu + \frac{\mu_t}{\sigma_\varepsilon}\right)\frac{\partial \omega}{\partial x_j}\right] + G_\omega - Y_\omega + S_\omega \tag{A.13}$$

and,

$$\mu_{eff} = \mu + \mu_t \tag{A.14}$$

where G_k is the generation of turbulence kinetic energy and is formulated as:

$$G_k = -\rho\overline{u_i' u_j'}\frac{\partial u_j}{\partial x_i} \tag{A.15}$$

Evaluating G_k that is consistent with the eddy-viscosity model, it becomes

$$G_k = \mu_t S^2 \tag{A.16}$$

$$S \equiv \sqrt{2S_{ij}S_{ij}} \tag{A.17}$$

where S is the modulus of mean rate of strain tensor defined as

$$S_{ij} = \frac{1}{2}\left(\frac{\partial u_j}{\partial x_i} + \frac{\partial u_i}{\partial x_j}\right) \tag{A.18}$$

The rest of the terms for the Wilcox model are then defined as:

$$G_\omega = \alpha\frac{\omega}{k}G_k \tag{A.19}$$

$$Y_k = \rho\beta' k\omega \tag{A.20}$$

$$Y_\omega = \rho\beta\omega^2 \tag{A.21}$$

and S_ω and S_k are user defined source terms. For the Wilcox model the constants are:

$$\alpha = \tfrac{5}{9},\ \beta = 0.075,\ \beta' = 0.09,\ \sigma_k = 2 \text{ and } \sigma_\omega = 2$$

The various $k{-}\omega$ models has been widely used in engineering analyses particularly turbo machinery, as it can be integrated to a wall without using damping functions and are considered accurate and robust for a wide range of boundary layer flows [66].

A.1.2 The $k-\varepsilon$ model

The $k-\varepsilon$ model is considered the work horse for turbulent flow simulation in engineering applications. Part of the answer as to why it is so popular lies in its robustness, computational economy compared to other turbulence models and its applicability to a wide range of turbulent flow problems [62, 66]. The standard $k-\varepsilon$ model assumes that the flow is fully turbulent and that the effects of molecular viscosity is negligible.

For the this model u_t is defined as:

$$u_t = C_\mu \left(\frac{\rho k^2}{\varepsilon} \right) \tag{A.22}$$

and the transport equations are formulated as:

$$\rho \frac{\partial k}{\partial t} = \frac{\partial}{\partial x_j} \left[\left(\mu + \frac{\mu_t}{\sigma_k} \right) \frac{\partial k}{\partial x_j} \right] + G_k - \rho\varepsilon \tag{A.23}$$

$$\rho \frac{\partial \varepsilon}{\partial t} = \frac{\partial}{\partial x_j} \left[\left(\mu + \frac{\mu_t}{\sigma_\varepsilon} \right) \frac{\partial \varepsilon}{\partial x_j} \right] + C_{\varepsilon 1} G_k - C_{\varepsilon 2} \rho \frac{\varepsilon^2}{k} \tag{A.24}$$

where G_k is formulated as in the Wilcox model. The $k-\varepsilon$ model constant are defined as:

$$C_{\varepsilon 1} = 1.44,\ C_{\varepsilon 2} = 1.9,\ C_\mu = 0.09,\ \sigma_k = 1.0 \text{ and } \sigma_\varepsilon = 1.3$$

A problem with the standard formulation exists as it is possible to obtain a result that produces a negative quantity for the normal stress, $\bar{u}^2$, when the strain becomes too large; rendering the mathematics "non-realizable" [66]. The "realizable" formulation is then conducted to prevent this occurrence of negative normal stress and addresses various shortcomings of the standard model. The transport equation differs slightly from the standard model, but the main difference lies in that C_μ is no longer a constant but computed from:

$$C_\mu = \frac{1}{A_0 + A_s \frac{kU^*}{\varepsilon}} \tag{A.25}$$

where, $A_0 = 4.04$ and $A_s = \sqrt{6}\cos\phi$ and,

$$U^* \equiv \sqrt{S_{ij} S_{ij} + \tilde{\Omega}_{ij} \tilde{\Omega}_{ij}} \tag{A.26}$$

where $\tilde{\Omega}_{ij}$ is composed of mean rates of rotation, and the model constants become:

$$C_{\varepsilon 1} = 1.44,\ C_{\varepsilon 2} = 1.9,\ \sigma_k = 1.0 \text{ and } \sigma_\varepsilon = 1.2$$

The realizable model effectively relates the C_μ term as a function of the mean strain and rotation rates; angular velocity, and the turbulence dissipation and energy rates. Further derivation of ϕ and $\tilde{\Omega}_{ij}$ is ommited in this text but [66] can be consulted for more information.

This section aimed to provide a brief look at the Navier-Stokes equations as well as how turbulence is handled in the solver used, Fluent. For more detailed information regarding formulation and implementation of the governing equations into the finite volume solver and related solution formulation, consult Fluent documentation [66]. In addition simulation details specific to this research is presented in Appendix B.

Appendix B

Simulation Details

Table B.1: Added points for SVR convergence.

x1	x2	x3	x4	cP	CD
0.415	0.435	0.455	0.495	1.4657	1.8323
0.415	0.435	0.475	0.505	1.5354	1.7569
0.415	0.435	0.475	0.505	1.5308	1.7194
0.415	0.435	0.4852	0.5308	1.6115	1.7128
0.4332	0.4532	0.4988	0.5188	1.5837	1.6791
0.5082	0.5356	0.556	0.5756	1.1807	1.4591
0.4348	0.4548	0.5046	0.5477	1.5644	1.6232
0.415	0.435	0.455	0.5588	1.3258	1.4893
0.4349	0.4549	0.5044	0.5475	1.5642	1.622
0.4517	0.4717	0.4917	0.5117	1.3683	1.5833
0.4184	0.4428	0.4984	0.535	1.668	1.734
0.426	0.4463	0.4984	0.548	1.672	1.728

Table B.2: Simulation details for Rotor experiment.

Rotor modelling- 2D-axisymmetric		
	Objective: Evaluate the performance of a rotor modelled as a discontinuous pressure jump	
Experiment	Variable	Trials
	pressure jump	11
	Turbulence models	3
	Total	44
Fluid Space	X (stream wise)	8.8 m
	Z(vertical)	2.8 m
	rotor radius	0.4 m
Materials	Fluid	Fluid (Water): density = 998 kg/m^3; viscosity 0.00155
Inlet	Velocity Inlet	axial velocity = 1.5 m/s; radial velocity = 0 m/s; Turbulence Intensity 5%; Turbulent Length scale 0.08 m
Outlet	Pressure outlet	Specification method: K and epsilon; Backflow turbulent kinetic energy = 1
Hub	wall	Stationary wall; No slip; Roughness height = 2e-05; Roughness constant = 0.5
Solver		Type: Pressure-Based; Velocity Formulation = Absolute; Time Steady; 2D space = axisymmetric
Models		Various:k-epsilon realizable; laminar; k-omega standard;
Solve Methods		Scheme = SimpleC; Gradient = Green-Gauss Node Based; Pressure = PRESTO!; Momentum,Turb Kinetic Energy and Turbulent Dissipation = Second-Order Upwind
Monitors	velocity	axial velocity of rotor
	pressure	just before rotor and just after rotor
	Residuals	1e-6
MESH	Quality (worst element)	Skewness (0.48); Squish (0.28); Aspect Ratio (4.2)
(Unstructured Tri-pave)	Cells	42 464
	Iteration to convergence	3800

Table B.3: Function Evaluation simulation details.

Function Evaluation-Diffuser- 2D-axisymmetric		
	Objective: Generate various model geometry and analyses for DOE	
Experiment	Variable	Trials
	Training points	110
	Test points	25
	Total	135
Fluid Space	X (stream wise)	8.8 m
	Z(vertical)	2.8 m
	rotor radius	0.4 m
	diffuser radius (outer, inner)	0.726 m, 0.415 m
Materials	Fluid	Fluid (Water): density = 998 kg/m^3; viscosity 0.00155
Inlet	Velocity Inlet	axial velocity = 1.5 m/s; radial velocity = 0 m/s; Turbulence Intensity 5%; Turbulent Length scale 0.08 m
Outlet	Pressure outlet	Specification method: K and epsilon; Backflow turbulent kinetic energy = 1
Hub and Diffuser	wall	Stationary wall; No slip; Roughness height = 2e-05; Roughness constant = 0.5
Solver		Type: Pressure-Based; Velocity Formulation = Absolute; Time Steady; 2D space = axisymmetric
Turb Model		k-epsilon realizable
Solve Methods		Scheme = SimpleC; Gradient = Green-Gauss Node Based; Pressure = PRESTO!; Momentum,Turb Kinetic Energy and Turbulent Dissipation = Second-Order Upwind
Monitors	velocity	axial velocity of rotor
	pressure	just before rotor and just after rotor
	Drag	Diffuser
	Residuals	1e-6
MESH	Quality (worst element)	Skewness (0.525); Squish (0.323); Aspect Ratio (4.85)
(Unstructured Tri-pave)	Cells	168 682
	Iteration to convergence	10 000

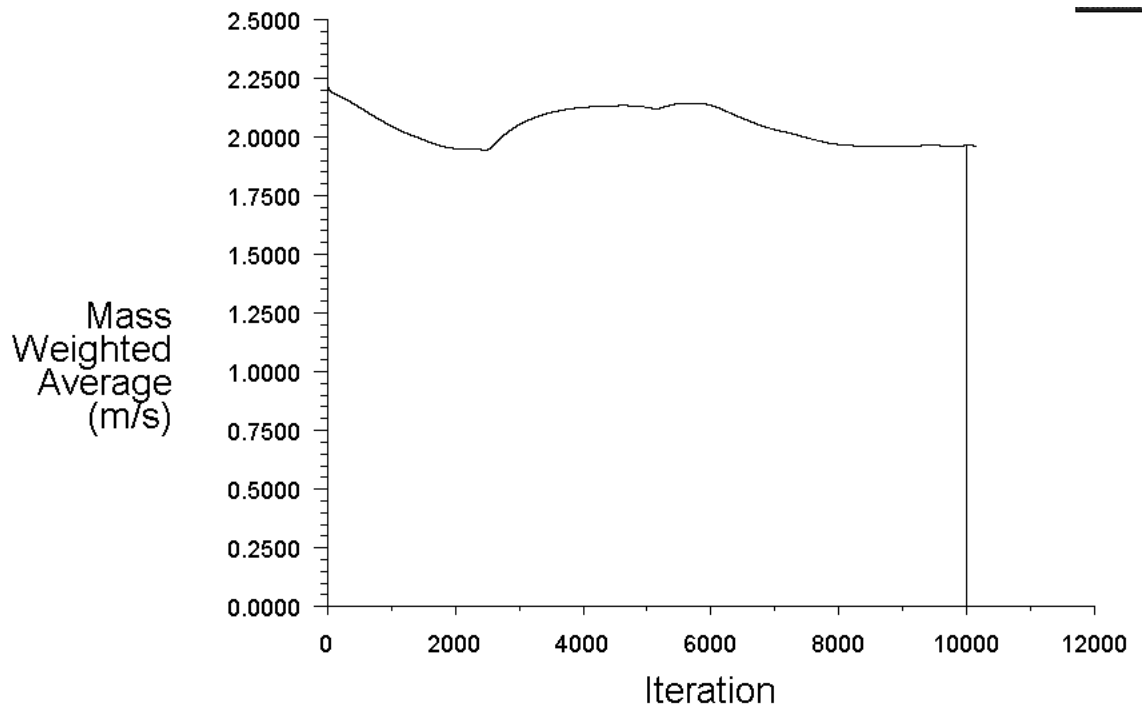

Figure B.1: Convergence of rotor axial velocity

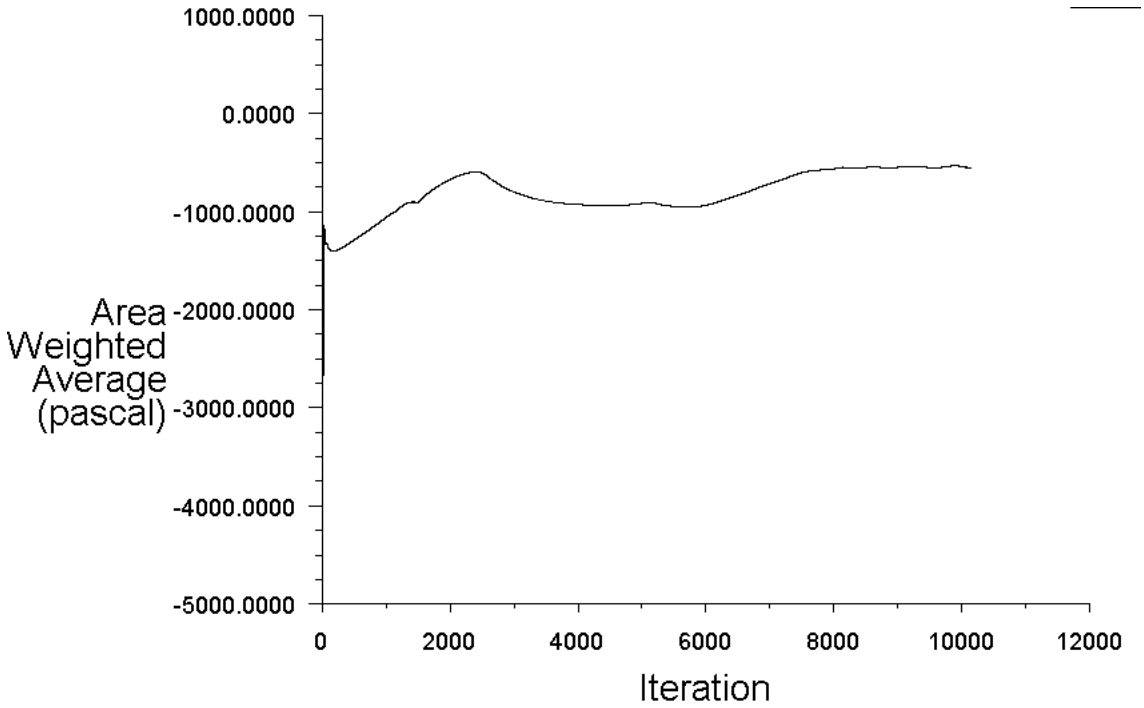

Figure B.2: Convergence of static pressure just in front of rotor

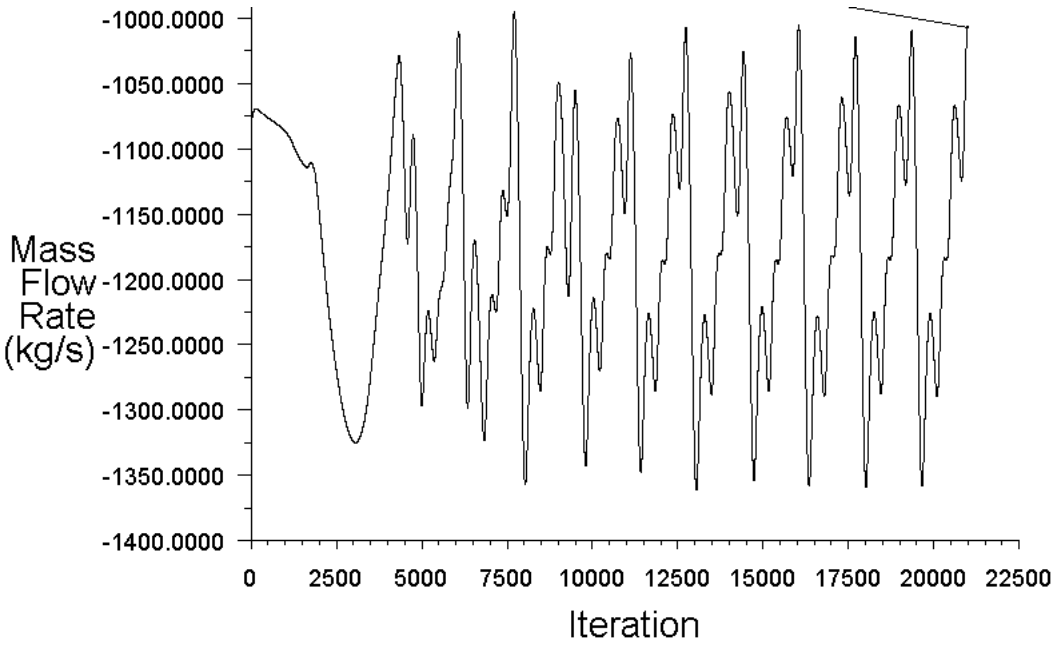

Figure B.3: Convergence of massflow through rotor

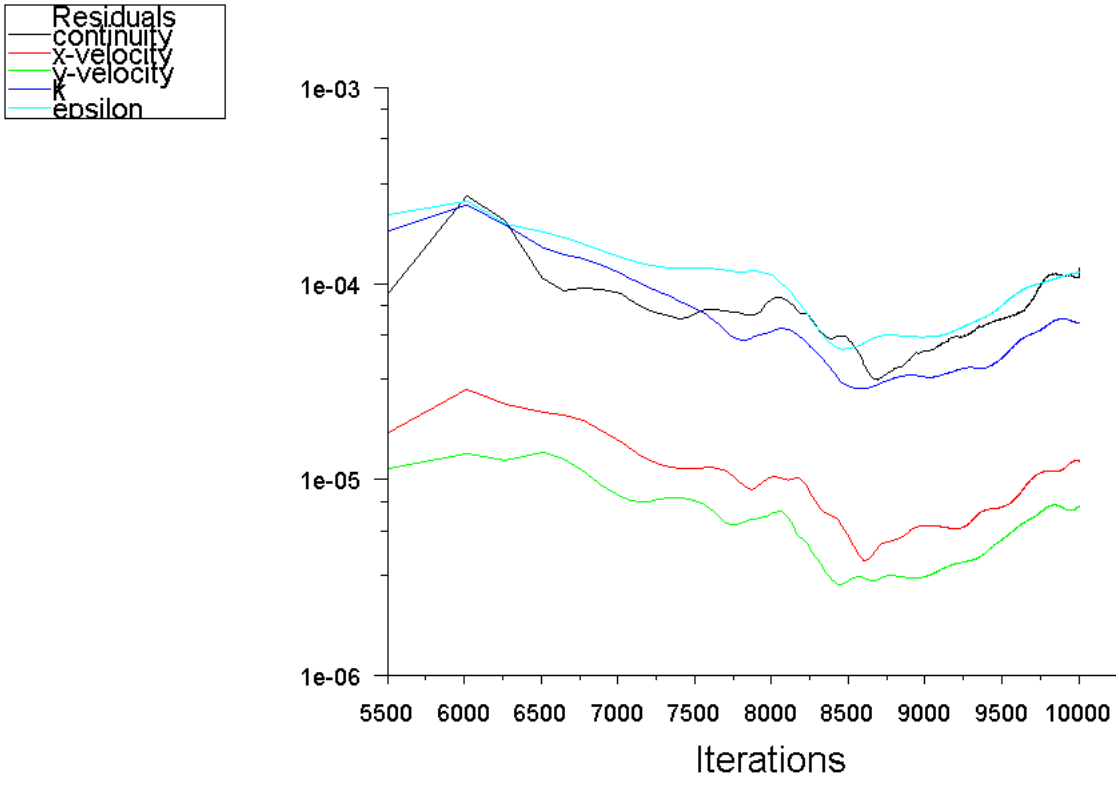

Figure B.4: Residuals of function evaluation

Table B.4: Blockage investigation simulation details.

Blockage Effect		
	Objective: Evaluate the Blockage Effect	
Experiment	Variable	Trials
	Fluid space height	3
	Total	3
Fluid Space Normal then Towing tank dimensions	X (stream wise)	8.8 m
	Z(vertical) from rotor axis to fluid surface	2.8 m and 1.2 m and 4 m
	rotor radius	0.4 m
Materials	Fluid	Fluid (Water): density = 998 kg/m^3; viscosity 0.00155
Inlet	Velocity Inlet	axial velocity = 1.5 m/s; radial velocity = 0 m/s; Turbulence Intensity 5%; Turbulent Length scale 0.08 m
Outlet	Pressure outlet	Specification method: K and epsilon; Backflow turbulent kinetic energy = 1
Hub	wall	Stationary wall; No slip; Roughness height = 2e-05; Roughness constant = 0.5
Solver		Type: Pressure-Based; Velocity Formulation = Absolute; Time Steady; 2D space = axisymmetric
Turb Models		Various:k-epsilon realizable
Solve Methods		Scheme = SimpleC; Gradient = Green-Gauss Node Based; Pressure = PRESTO!; Momentum, Turb Kinetic Energy and Turbulent Dissipation = Second-Order Upwind
Monitors	velocity	axial velocity of rotor
	pressure	just before rotor and just after rotor
	Residuals	1e-6
MESH	Quality (worst element)	Skewness (0.48); Squish (0.28); Aspect Ratio (4.2)
	Cells	406605
	Iteration to convergence	Varied between 10 000, 20 000 and 35 000

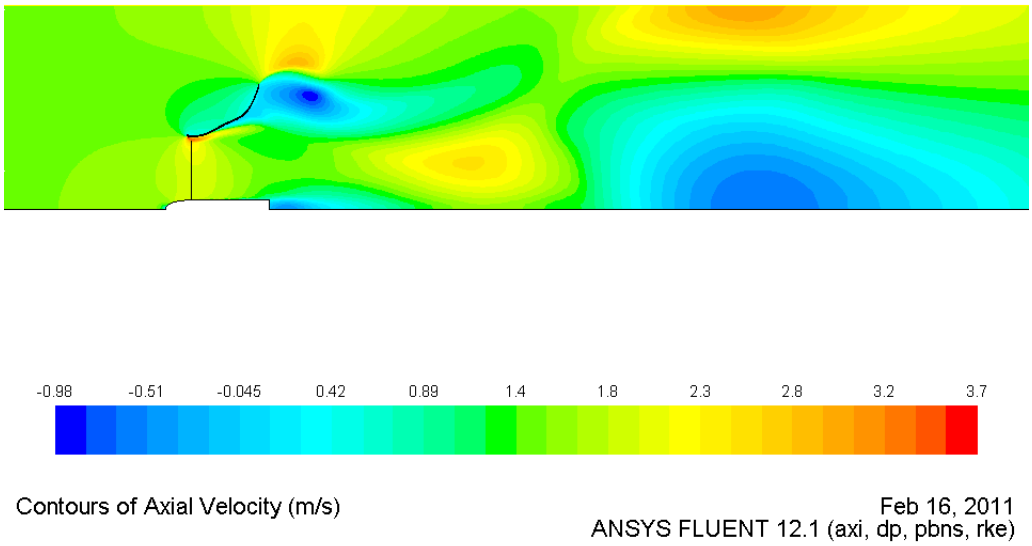

Figure B.5: Blockage investigation, vertical radius of 1.2 m

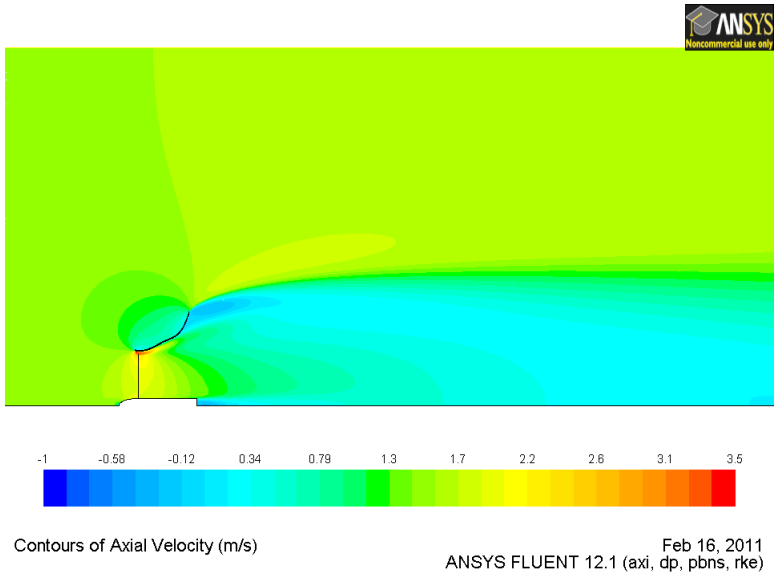

Figure B.6: Blockage investigation, vertical radius of 2.8 m

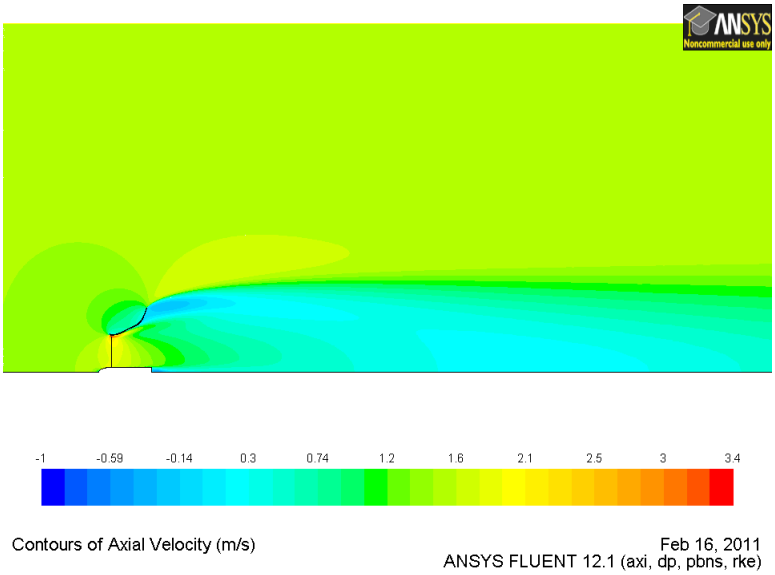

Figure B.7: Blockage investigation, vertical radius of 4 m

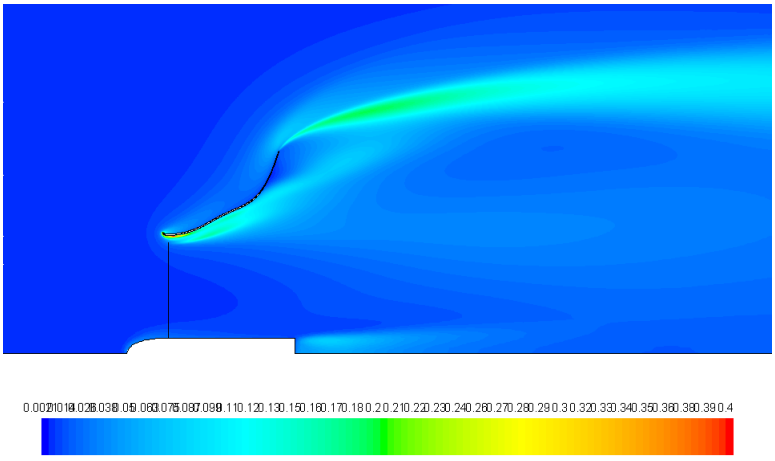

Figure B.8: Contour plot of turbulence kinetic energy in the diffuser area.

Appendix C

Design FEM and Topology Optimisation

C.1 Structural Design Considerations

For the chosen diffuser shape the design of the diffuser and the support structure were performed. Some considerations that we kept in mind are that the rig needed to be as stiff as possible to minimise the amount of deflection experienced by the support structure and diffuser.

The reason being that the current test rig as used by [11] consists of two independent parts, namely the turbine rotor assembly (TRA) and the diffuser with support structure (DSS). Thus they are able to deflect in the axial direction independent of each other. This can have adverse effects, for instance during testing if the amount of deflection experienced by the DSS and TRA differs the rotor will be tested at a different axial location as the one used in the optimisation.

In addition the diffuser alone needed to be made as stiff as possible so that its shape does not change severely during testing so as to assure that the diffuser that is tested experimentally corresponds well with the optimised diffuser shape calculated using SVR. But for this the optimised shape was found to be relatively insensitive to shape changes from numerical studies as shown in figure 5.11.

Seeing that the diffuser shape was complex and to check its influence on the support structure and vice versa it was decided to proceed creating a FEM model of both independently and then integrating them. A figure showing the original DSS and TRA is shown in figure below.

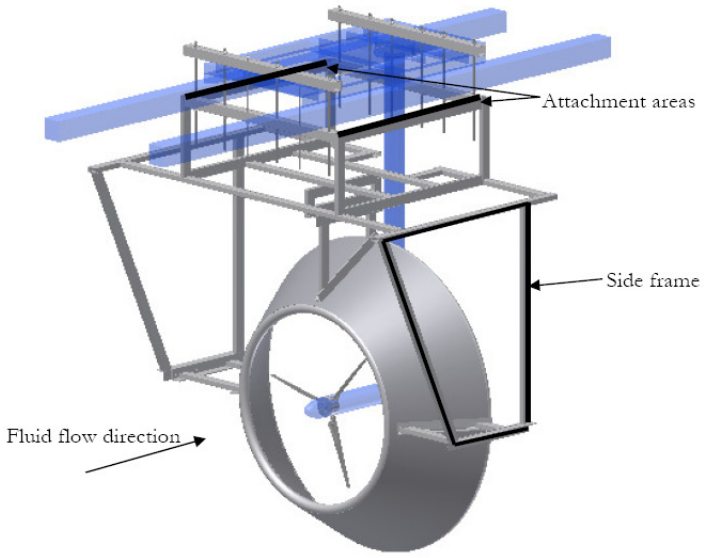

Figure C.1: DSS as used in Grobbelaar.

C.2 FEM Analyses

For the DSS a full FEM model was created initially starting with the support structure as shown in figure C.1. For this the load case was used to include the drag effects of the newly designed optimum diffuser. This total force applied to the diffuser as a total load. The drag force measured from CFD analyses was 3300 N in the axial direction, however for the load case a safety factor of 1.375 was applied and a total drag force of 4400 N applied. The drag force was modelled as a 'total force' discretely applied to each node on the diffuser surface. This safety factor was determined for non-oscillating loads to be 1.3 but to include some model inaccuracies a safety factor of 1.375 was chosen Also the displacement was restricted to the attachment area as showed in figure C.1, allowing no translations in the x,y and z directions, thus considering the areas to be infinitely stiff.

After analysing the model, it was validated against analytical calculations and checked the absence of free body modes. From the results the areas that showed the most deformation in the structure could be identified. With a maximum deflection of 28 mm occurring at the centre of the diffuser in the fluid flow direction.

C.3 Topology Optimisation

In order to determine the best possible placement of some of the struts in the existing diffuser support structure topology optimisation was used to generate the stiffest possible

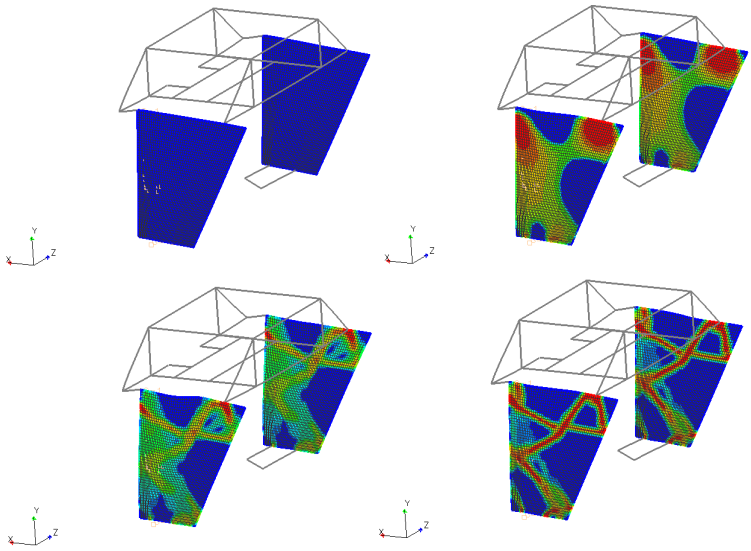

Figure C.2: Topology optimisation results.

configuration. This applied only to the two side frames having a trapezoidal form. The idea was to place struts on the inside of the side frames to increase its stiffness.

The basic formulation for the topology optimisation used modelled the side frame as a solid plate and then placing a constraint on it to reduce the mass or area by 70% and for that case calculate the appropriate configuration of material that will produce the stiffest possible structure. The topology results are shown in figure C.2.

Although topology optimisation is considered to accelerate the concept design stage of a project this was also proved to be the case in the design of the diffuser support structure. Thus from the last graphic in figure C.2 the placements of struts for the support frame was made and also checked to exceed other strut configurations with regard to stiffness added to the total structure.

After adding additional struts a new FEM analyses was created that included the new structure as well as the diffuser. For this analyses the diffuser was modelled using 10576 quad shell elements with isotropic properties. For the support structure a total of 2277 beam elements were used. The load case included the total load as applied in the previous analyses with the same displacement constraint.

C.4 Results & Conclusion

All beam elements were had a rectangular tubing profile similar to the current support structure that is used. Due to the project budget a more complex shaped cross-section beam was not to be used and thus the rectangular tubing selected and hence the use in the FEM model.

Additionally after various investigations into the diffuser thickness a thickness of 10 mm was selected as being the best compromise between cost and minimising the deflection experienced by the diffuser. Arriving at the diffuser thickness was done following a iterative process where the thickness was changed in increments of 1 mm from 1 mm to 14 mm. The optimal wall thickness that met the required strength requirements was then 10 mm. The figure below is a displacement fringe plot of the FEM model.

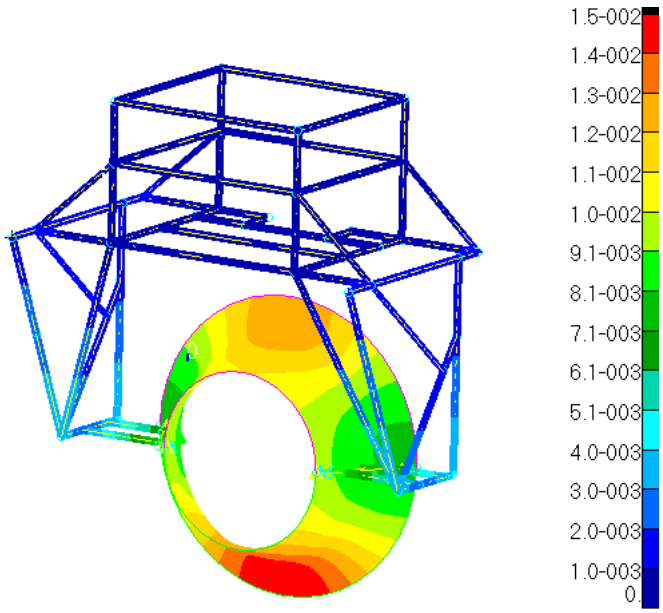

Figure C.3: FEM displacement plot (m).

The maximum deflection is experienced in the top centre part of the diffuser. Some important results for the model is summarised in the table below.

Table C.1: Stress and displacement results from combined FEM model.

	Maximum Combined Stress	**Maximum Displacement**
Support Structure	93 MPa	8.3 mm
Diffuser	14.7 MPa	12.5 mm

Table C.2: Stress and displacement results for diffuser only varying in thickness.

Thickness	**Maximum Combined Stress**	**Maximum Displacement of Diffuser**
2 mm	203 MPa	39 mm
4 mm	55 MPa	7.4 mm
6 mm	25 MPa	3.2 mm
8 mm	18 MPa	2.4 mm
10 mm	14.7 MPa	1.5 mm

Mild steel has a yield strength of approximately 240 MPa Craig [77] thus the support structure is well within failure limits. For the diffuser a composite chop strand matt (CSM) with density of 450 g/$m^2$where used with and a four layer hand lay-up was used with a low shrinkage polyester resin. From the manufacturer a tensile strength for this setup was quoted as being approximately 90 MPa. Thus the material according to the FEM model would not fail.

In addition a buckling analyses was done on the FEM model and no buckling was predicted with the current load case. Thus the design was found to be strong enough and allowed minimum deflection so as to limit the measured discrepancy between the optimisation CFD results and experimental testing. The final design is shown in the figure below. Note that the green struts are the newly added and strategically placed tubing.

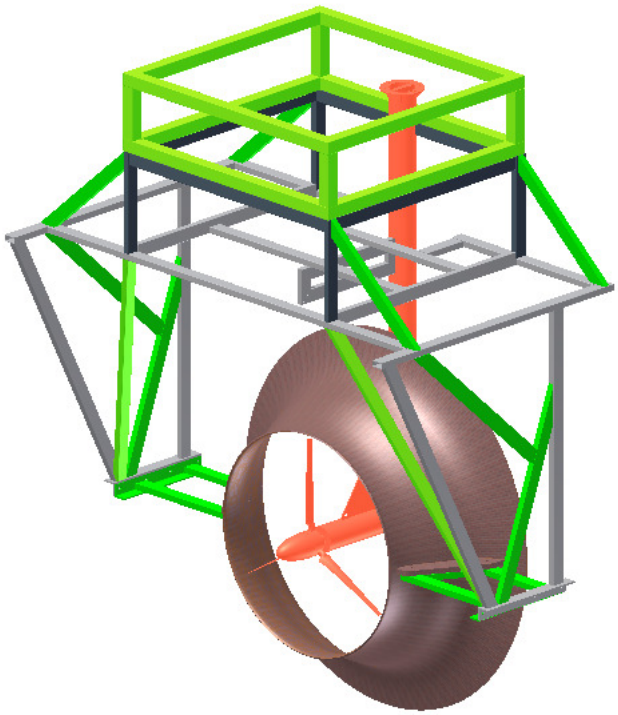

Figure C.4: New test rig design showing additional strengthening supports (green struts).

Note the green frame box at the top of the support structure. This is a spacer that was added so that the turbine axis was exactly in the middle of the towing tank environment. In other words the distance from the centre of the turbine to the water surface is the same as the distance from the turbine centre to the towing tank floor. Also from this figure that the relative deflection in the flow direction has been prohibited by placing the diffuser outlet directly against the turbine upright. Thus if any motion no relative motion will occur between the diffuser and rotor.

From this section a design has emerged that has two major advantages, one will allow minimal structural deflection and secondly will not fail under operation. The FEM approach together with topology optimisation proved to be vital in obtaining the design advantages.

Appendix D

Test Calibrations

D.1 Torque Transducer Calibration

To calibrate the torque transducer an experimental setup was used as shown in the figure below. It involved manufacturing a swing arm with a specific length and various weights.

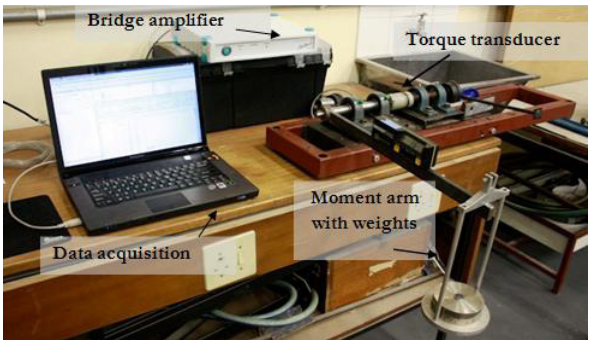

Figure D.1: Torque transducer calibration setup.

The reasoning behind this involved inducing a specific torque on the shaft connected to the transducer. This torque is produced by using a swing arm that at its end is fitted with a carriage that can hold weights. Thus the amount of torque applied can be varied by addition or subtraction of weights. As can be seen an inclination meter was also used to determine the angle that the swing arm produces as accounting for this was necessary to produce accurate calibration data. The data obtained in terms of measured torque against applied torque is show in terms of error percentage in the figure below.

From this it was seen that the torque transducer has been accurately calibrated for our system and reliable torque data can be captured by it.

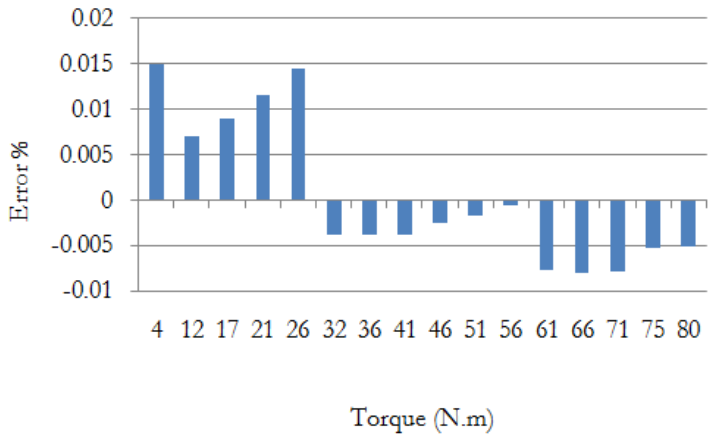

Figure D.2: Error (%) between measured and applied torque.

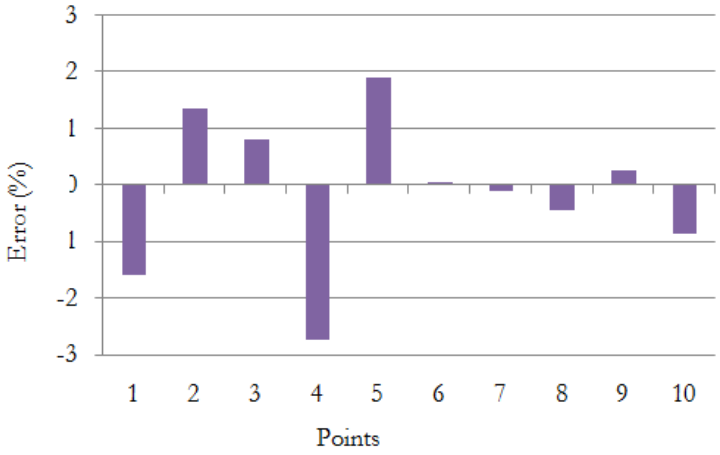

Figure D.3: Trolley speed calibration results.

D.2 Towing Tank Trolley Velocity Calibration

In order to check that the towing tank trolley speed was acceptable the visual output from the trolley indicating velocity in m/s was calibrated against measured distance and time. This entailed marking of 6 m lengths in succession next to the trolley and by means of a stop watch measuring the time the trolley takes to pass each 6 m interval.

Although not the most digitally accurate way of calibration this provided remarkably good results. The results are shown in figure D.3 where the error (%) represents the amount of error between measured velocity (from the trolley control panel) and actual velocity.

In addition the only other measurement component needing calibration was the tachometer. These were however newly acquired instruments and still carried their calibration certificates.

Concluding the calibration, the test setup was installed in the towing tank facility. Some

initial test were done to investigate certain dynamics in data results and establish if the test setup performed adequately.

D.3 System Losses

The system losses needed to be measured as they will need to be included in performance calculations of the turbine. The losses mainly comprised bearing friction losses and the frictional loss associated with the chain and sprocket drive system. For this test, the rotor was removed and the motor allowed to drive the system across various RPM ranges and the corresponding torque measured. The losses are displayed below.

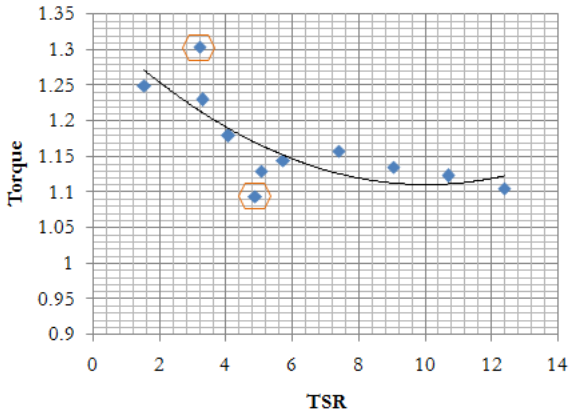

Figure D.4: System losses.

Note the two points encircled by a hexagon where identified as outliers by applying the three-sigma test as described in [73]. A second-order polynomial trend was also calculated for inclusion in performance calculation of the turbine. The torque loss is denoted as T_{loss}.

D.4 Sample Calculations

A sample calculation will now be presented in determining the performance of the turbine. This assumes that the raw data for a specific point has been averaged within a specified time sampling period where the data was stable. In addition, for the performance curve presented in the next chapter, a three-sigma outlier detection scheme was used to refine the data sets.

Because of the conservation of energy from the rotor shaft to the top shaft, where the measurements are taken, applying the relation $P = T\omega$ will yield the power of the turbine.

For a given measurement of torque, say $T_{measured} = 16.8\,N.m$ and measured RPMs of say $RPM_{measured} = 215$ the following calculation is done.

$$\omega = RPM_{measured} \times \left(\frac{2\pi}{60}\right) = 22.5\,rad/s \tag{D.1}$$

$$TSR_{measured} = \frac{\omega R}{V_0} = 6 \tag{D.2}$$

Where R is the rotor radius of 0.4 m, and V_0 the free stream velocity of 1.5 m/s. Now calculating the friction loss from the trend in data.

$$T_{loss} = 0.002(TSR)^2 - 0.045TSR + 1.336 = 1.138\,N \tag{D.3}$$

$$T = T_{measured} + T_{loss} = 16.8 + 1.138 = 17.938\,N \tag{D.4}$$

$$P = T\omega = 17.938 \times 22.5 = 403.6\,W \tag{D.5}$$

However the power has now been calculated the actual turbine shaft TSR still needed to be calculated. For this the ratio in sprocket pitch circle diameter is used:

$$TSR = TSR_{measured} \times \frac{d_{top}}{d_{bottom}} = 6 \times 0.694 = 4.16 \tag{D.6}$$

Thus for the turbine a single performance data point has been calculated. The point shows the turbine produces a power $P = 403.4\,W$ at a $TSR = 4.16$. Additionally $C_p$can be calculated by the definition of $C_p$as described in equation 2.24.

$$C_p = \frac{P}{P_{avail}} = \frac{P}{\frac{1}{2}\rho A V_0^3} = \frac{403.6}{\frac{1}{2} \cdot 998 \cdot \pi \cdot (0.4^2 - 0.055^2) \cdot 1.5^3} = 0.4859 \tag{D.7}$$

Note the density of water is taken a 998 kg/$m^3$and the area corresponds to the rotor tip (0.4 m) to the rotor hub (0.055 m).

Appendix E

Experimental details

E.1 Equipment Details

Table E.1: Experimental equipment details.

Description	Manufacturer	Model	Comment
Variable Speed Drive	Mitsubishi	e500 fr-e540-7.5k-ec	Frequency controller 7.5 kW
Torque Transducer	Hottinger Baldwin Messtechnik (HBM)	T4A 100 Nm	
Data Acquisition Software	Hottinger Baldwin Messtechnik (HBM)	CatmanEasy, version 2	Release 2
Bridge amplifier	Hottinger Baldwin Messtechnik (HBM)	Spider8	8 channels
3 phase motor	S&P		2.2 kW, 220 V, 50 Hz
Optical Tachometer	CT Lutron	DT-2234a dig tacho	Sampling rate: 1 sec, averaging filter

E.2 Towing Facility

Figure E.1: Towing tank facility.

E.3 Free Surface Effects

Figure E.2: Surface effects.

E.4 Raw Data

Table E.2: Raw data of performance curves for the Bahaj rotor.

R.P.M.	Torque	Power	R.P.M.	Torque	Power
362.754	32.0237	1216.5	93.1056	9.4359	92
298.296	48.397	1511.8	196.954	56.2424	1160
302.593	47.716	1512	171.887	43.8333	789
334.213	40.0786	1402.7	148.611	35.0201	545
407.695	21.2677	908	164.009	41.8632	719
394.267	24.8671	1026.7	298.296	51.5982	1611.8
364.688	31.2726	1194.3	404.651	29.3097	1242
356.308	38.2338	1426.6	406.004	968.9	22.7887
376.004	28.6705	1128.9	228.44	1146.2	47.9137
275.736	29.1567	1145	243.295	1548	60.7589
239.926	51.6856	1298.6	76.0387	58.2	7.30903
268.574	50.5956	1423	84.3627	75.3	8.52346
218.44	49.4514	1131.2			
273.695	54.0102	1548			
199.103	56.5947	1180			
68.0387	8.42105	60			
82.3627	8.86029	76.42			
94.1799	9.65982	95.27			
143.239	26.5435	390			
125.335	15.2381	200			
114.592	11.3333	136			
105.818	10.6486	118			

Table E.3: Raw data of performance curves for Stanford rotor set.

R.P.M.	Torque	Power
214.8592	49.13333	1105.5
200.5352	43.04762	904
214.8592	48.4	1089
214.8592	40.04444	901
250.669	50.2819	1319.9
277.6697	44.16817	1284.3
283.6141	40.81145	1212.1
314.0525	40.17028	1321.1
334.8222	34.17897	1198.4
351.1157	29.31294	1077.8
380.6588	22.7783	908
422.5564	14.39503	636.98
451.2043	8.825397	417
179.766	37.29084	702
148.611	35.02008	545
125.3345	15.2381	200